ELECTRIC FIELD-DRIVEN ENGINEERING OF FUNCTIONAL POLYMERIC MICRO/NANO-STRUCTURES

BY

SALMAN MALIK

A THESIS SUBMITTED IN PARTIAL FULFILMENT OF THE REQUIREMENTS FOR THE DEGREE OF

DOCTOR OF PHILOSOPHY

FACULTY OF ENGINEERING
DEPARTMENT OF ELECTRONIC AND ELECTRICAL ENGINEERING

UNIVERSITY COLLEGE LONDON
UNITED KINGDOM

MARCH 2016

‘I, SALMAN AHMED MALIK confirm that the work presented in this thesis is my own. Where information has been derived from other sources, I confirm that this has been indicated in the thesis.'

ABSTRACT

Nanoscopic processing of polymer-nanoparticle composite materials has attracted a great deal of interest due largely to their unique physical and chemical properties. Metal nanoparticles present particularly attractive building blocks as starting materials to fabricate assemblies for future nanodevices with unique electronic properties. However, their fabrication currently remains a great challenge in nanotechnology due to the complexity of organizing metal nanoparticles in low symmetry. Current conventional methods to generate high-aspect ratio linear fibres rely on techniques such as drawing, template synthesis, self-assembly, electron-beam lithography and nanolithography, although these techniques suffer from poor time efficiency, costly starting materials, and all five are difficult to scale up for industrial production, as they rely on batch-type processes.

This work, inspired by frugal engineering, focuses on the controlled manufacture of polymer/nanoparticle assemblies using electrospinning. We show how trade-offs in fibre size, morphology and structure can be controlled by varying nanoparticle loading in the slurry to carefully engineer linear composite nanomaterials. This procedure circumvents the space, regulation, control, standards and maintenance necessary for state-of-the-art cleanroom facilities.

This thesis demonstrates the fabrication of composite nanowires by a single-step electrospun deposition of semi-crystalline Poly(ethylene oxide) (PEO) and zero-valent metallic gold nanoparticle (Au NP) blends. Au NP loading determined the fate of fibre shapes, sizes and electrical performance.

The goal of controlled drug delivery is to administer sustained amounts of a therapeutic agent over a prolonged period of time, improving the drug efficacy as compared to conventional, bolus doses that lead to variable concentrations of antibiotics in the blood. Although there are several systems capable of providing such a continuous-dose-based treatment, the use of biodegradable polymer microparticles offers multiple advantages with respect to other platforms. Microsphere-based controlled release technologies have been utilized for the long-term delivery of proteins, peptides and antibiotics, although their synthesis poses substantial challenges owing to formulation complexities, lack of scalability, and cost. Conventional methods rely predominately on batch, emulsion preparation methods and suffer from several drawbacks: poor control over particle size distribution, broad size distributions at the micro scale, and poor repeatability. To address these shortcomings, the electrospray (ES) process was used as a reproducible, synthesis technique to manufacture highly porous (>94%) microspheres while maintaining control over particle structure and size. This thesis reports a successful formulation recipe used to generate spherical poly(lactic-co-glycolic) acid (PLGA) microspheres using ES coupled with a novel thermally induced phase separation (TIPS) process.

In this work, PLGA microspheres in a range of different sizes, morphologies and compactness are generated using the ES route. The sizes of synthesized particles are primarily controlled by the delicate tuning of the solution physical properties and the ES operational parameters. We show how size, shape and porosity of resulting microspheres can be controlled by judiciously varying ES processing parameters and we demonstrate examples in which the particle sizes affect release kinetics. Importantly, throughout this series of studies, efforts were made to remove the synthesis approach from the all too common empiricism of a large fraction of the literature on materials synthesis, and to establish fundamental criteria that would allow for the generation of particles of prescribed size, morphology and consistency from first principles.

CONTENTS

DEDICATION

TO MY PARENTS; MUSHTAQ AND FOUZIA, MY BROTHERS; JAWWAD AND JAMSHED AND MY BETTER HALF; ANAH,
FOR THEIR SACRIFICES AND ENDLESS SUPPORT.

ACKNOWLEDGMENTS

A thesis requires a significant team effort and mine is no exception. Without the help and support of my family, friends, and colleagues, to whom I wish to extend my gratitude, this work would not have been possible.

Firstly, I would like to thank my supervisor and friend Professor Anthony Kenyon to whom I am greatly indebted for giving me the opportunity and support to embark on my academic journey. His continuous guidance, constructive criticism and support have been invaluable for me as an academic and as an individual. His peaceful nature, patience and endless ability to generate ideas have collectively been inspirational. I cannot have asked for anymore.

I am very grateful to all my collaborators, Dr. Richard Day and Professor Alessandro Gomez for their input and contribution to my research in the form of much advice, knowledge transfer and support. I would like to thank Professor Gomez for the time spent in his lab at Yale University (2014).

A special thanks goes to Dr. Suwan Jayasinghe for his continuous support during my master's degrees and doctoral research. He has been a great friend and our encounters have been filled with humor and countless memories. I am also forever in debt to Dr. Wing Ng for his active involvement in my research and his gifted hands for aid in fabricating devices in my research. I would like to thank all group members, especially Dr. Miraj Shah for being a great friend during the initial stages of my research.

I thank all my friends who have provided me with plenty of entertainment for many years. Their support has ensured I remained sane throughout my Ph.D.

A special thank you goes to my parents for their patience, support, love and understanding. Finally, I want to finish by dedicating a line to my best friend and beautiful better half, Anah. She has been incredibly patient with me during my research and I could not have asked for a better partner to share my life with.

I would like to gratefully acknowledge: (i) the financial support provided by the Engineering and Physical Sciences Research Council (EPSRC) through a Doctoral Training Award (DTA), (ii) the London Centre for Nanotechnology (LCN) for use of the Scanning Electron Microscope and Focused Ion Beam facility, (iii) Dr Michel Bosman at the Institute Of Materials Research and Engineering (IMRE), A*STAR, Singapore for use of the Scanning Transmission Electron Microscope facility, (iv) The UCL Institute of Biomedical Engineering (IBME) Yale-UCL Medical Technologies Collaborative (MTC) and (v) The financial support provided by the Department of Biomedical Engineering at Yale University. This work was also partially undertaken at UCL/UCLH which receives funding from the Department of Health's NIHR as a comprehensive Biomedical Research Centre.

PUBLISHED WORK (LEAD AUTHOR)

FULL PAPERS

Malik, S.A., Ng W.H., Bowen J., Tang J., Gomez A., Kenyon A.J. and Day, R.M. (2016), Electrospray Synthesis and Properties of Hierarchically Structured PLGA TIPS Microspheres for use as Controlled Release Technologies, *Journal of Colloid and Interface Science*, 467, pp. 220-229, 2016.

CONFERENCE PAPERS

Malik, S.A., Ng W.H., Munde M., Jayasinghe S.N., Kitching H., Bosman M., Parkin I.P. and Kenyon A.J. (2015), Electrospun fabrication of one-dimensional composite nanofibres using colloidal gold/polymer aqueous blends, *in* Proc.*15th IEEE International Conference on Nanotechnology (IEEE Nano)*, no. 135.

CONFERENCE PRESENTATIONS

Malik, S.A., Ng W.H., Mehonic A., Kitching H., Parkin I.P. and Kenyon A.J. (2014), Electrospun one-dimensional composite nanostructures as potential electronic materials, *in* Proc. *Materials Research Society (MRS) Fall Meeting and Exhibit*, Cambridge University Press, no. B18.19.

(Boston, MA, USA)

Malik, S.A., Ng W.H., Bowen J., Tang J., Gomez A., Kenyon A.J. and Day, R.M. (2015), Electrospray synthesis of PLGA TIPS microspheres, *in* Proc. *2nd Announcement on Aerosol Technology (AT2015)*, no. 0112.

(Tampere, Finland)

Malik, S.A., Ng W.H., Munde M., Jayasinghe S.N., Kitching H., Bosman M., Parkin I.P. and Kenyon A.J. (2015), Electrospun fabrication of one-dimensional composite nanofibres using colloidal gold/polymer aqueous blends, *in* Proc. *15th IEEE International Conference on Nanotechnology (IEEE Nano)*, no. 135.

(Rome, Italy)

Malik, S.A., Ng W.H., Bowen J., Tang J., Gomez A., Kenyon A.J. and Day, R.M. (2015), Electrospray generated synthesis of highly porous PLGA TIPS microspheres, *in* Proc. *European Aerosol Conference (EAC)*, no. 1ELE_P001.

(Milan, Italy)

Malik, S.A., Ng W.H., Bowen J., Tang J., Gomez A., Kenyon A.J. and Day, R.M. (2015), Electrospray Manufacturing of Highly Porous Snowball-like PLGA TIPS-Microspheres using a novel Cryogenic Liquid-based Collection Scheme, *in* Proc. *Annual Aerosol Science Conference 2015.*

(Birmingham, UK)

Malik, S.A., Ng W.H., Bowen J., Tang J., Gomez A., Kenyon A.J. and Day, R.M. (2015), In vitro performance of dye-loaded microsphere-based controlled release technologies synthesized via electrospray atomization, *in* Proc. *3rd International Conference on Nanotechnology in Medicine (NanoMED),* no. MED-1.

(Manchester, UK)

CONFERENCES ATTENDED (AS DELEGATE)

"Research Commercialisation, From Ideas to IPO" (Elsevier), 2014

"Electrospinning: Principles, and Possibilities 2015" Institute of Physics (IOP) (4th Meeting), 2015

LIST OF FIGURES

CHAPTER 2

CHAPTER 3

CHAPTER 4

CHAPTER 5

CHAPTER 6

CHAPTER 7

LIST OF TABLES

CHAPTER 6

CHAPTER 7

NOMENCLATURE AND ABBREVIATIONS

θ	Contact Angle
ε	Dielectric Constant of the Liquid
ε_0	Permittivity of Free Space
ρ	Resistivity
k	Solution Electrical Conductivity (for Scaling Law)
σ	Solution Electrical Conductivity (from Resistivity measurements)
γ	Surface Tension
0D	Zero-dimensional
1D	One-dimensional
2D	Two-dimensional
3D	Three-dimensional
A	Cross-sectional Area
Ag	Silver
Ag NPs	Silver Nanoparticles
Al	Aluminium
Au	Gold
Au NPs	Gold Nanoparticles
Au NRs	Gold Nanorods
BF-STEM	Bright-Field Scanning Transmission Electron Microscopy
C-AFM	Conductive Atomic Force Microscopy
CED	Circular Equivalent Diameter
CMOS	Complementary Metal Oxide Semiconductor
Co	Cobalt
Cr	Chromium
CRM	Confocal Raman Microscopy

Cu	Copper
d	Droplet Diameter
d_1	Distance between Emitter and Extractor Electrode or Ground
d_2	Distance between Extractor Electrode and LN_2 Free Surface
d_{min}	Minimum Droplet Size
d_p	Diameter of the Particle
DC	Direct Current
DF-STEM	Dark-Field Scanning Transmission Electron Microscopy
DI	Deionized Water
DMC	Dimethyl Carbonate
DNA	Deoxyribonucleic Acid
DRAM	Dynamic Random Access Memory
E	Electric Field
EBL	Electron Beam Lithography
EE	Encapsulation Efficiency
ES	Electrospray
FE-SEM	Field Emission Scanning Electron Microscope
FIB	Focussed Ion Beam
FRAM	Ferroelectric Random Access Memory
FT82	Poly (9,9-dioctyl-fluorene-co-bithiophene)
Ga^+	Gallium ion
Hg	Mercury
HRS	High-Resistance State
HR-SEM	High-Resolution Scanning Electron Microscopy
HSC	High Sensitivity Circularity
HVPSU	High Voltage Power Supply Unit
I_{CC}	Collected Current
I_{EC}	Emitted Current
I_{FB}	Flyback Current

ID	Inner Diameter of ES Emitter
I-V	Current-Voltage
IVIVC	*in-vitro in-vivo* Correlation
LMIS	Liquid Metal Ion Source
LN_2	Liquid Nitrogen
LRS	Low-Resistance State
Ni	Nickel
NTA	Nanoparticle Tracking Analysis
OD	Outer Diameter of ES Emitter
O/W	Oil in Water
MiM	Metal-Insulator-Metal
MIP	Mercury Intrusion Porosimetry
MRAM	Magnetic Random Access Memory
NPs	Nanoparticles
P	Applied Pressure
P3HT	Poly (3-hexthiophene)
PBS	Phosphate Buffered Saline
PDLA	Poly (DL-lactic acid)
PEO	Poly (ethylene oxide)
PGA	Poly (glycolic acid)
PLA	Poly (lactic acid)
PLGA	Poly (lactic-co-glycolic acid)
PMMA	Poly (methyl methacrylate)
PRAM	Phase-Change Random Access Memory
PS	Polystyrene
Pt	Platinum
PTT	Poly (trimethylene terephthalate)
PVA	Poly (vinyl alcohol)
Q	Solution Flow Rate

Q_{min}	Minimum Solution Flow Rate
R6G	Rhodamine 6G
R	Resistance
RAM	Random Access Memory
ReRAM	Resistive Random Access Memory
RSD	Relative Standard Deviation
SBF	Simulated Body Fluid
SCS	Semiconductor Characterization System
SDU	Sample Dispersion Unit
SEM	Scanning Electron Microscopy
SERS	Surface-Enhanced Raman Scattering
SES	Sample Entrainment Spool
Si	Silicon
SiO_2	Silicon Oxide
SOP	Standard Operating Procedure
SPR	Surface Plasmon Resonance
SRAM	Static Random Access Memory
STEM	Scanning Transmission Electron Microscopy
STM	Scanning Tunneling Microscope
TEM	Transmission Electron Microscopy
TG	Thermogravimetry
TGA	Thermogravimetric Analysis
TIPS	Thermally Induced Phase Separation
TIV	Total Intrusion Volume
UV-Vis	Ultraviolet–Visible Spectroscopy
V	Applied Voltage
V_{onset}	Onset Voltage
W/O	Water-in-Oil
W/O/W	Water in Oil in Water

1. INTRODUCTION

Micro/nano-structures have received steadily growing interest as a result of their peculiar and fascinating properties and applications superior to their bulk counterparts. The ability to generate such miniscule structures is essential to much of modern science and technology. There are a large number of opportunities that might be realized by making new types of nanostructures, or simply by downsizing existing microstructures into the 1-1000nm regime. The most successful example is provided by microelectronics, where “smaller” has meant greater performance ever since the invention of integrated circuits. Miniaturization may also represent the trend in a range of other technologies, such as healthcare and pharmaceutical delivery technologies.

Polymeric microstructured or nanostructured systems show great potential in both the physical and life science industries although their synthesis poses substantial challenges owing to their formulation complexity, lack of scalability and cost. Attempts to engineer polymeric micro/nano-materials using cost-effective techniques has seen a rapid rise in recent years due to their use in several major industries including nanotechnology, biopharmaceuticals and medical devices [1].

1.1 ONE-DIMENSIONAL NANOSTRUCTURES

One-dimensional (1D) micro/nano-structures such as fibres, wires, rods, belts, and tubes have become the focus of intensive research owing to their unique applications in mesoscopic physics and fabrication of nanoscale devices [2]. It is generally accepted that 1D nanostructures provide a good system to investigate the dependence of electrical and thermal transport on dimensionality and size reduction. They are also expected to play an important role as both interconnects and functional units in fabricating electronic, optoelectronic, electrochemical and electromechanical devices with nanoscale dimensions. The advancement of 1D nanostructures has been slow until very recently, as hindered by the difficulties associated with the synthesis and fabrication of these nanostructures with well-controlled dimensions, morphology, phase purity and material composition. Although 1D nanostructures can now be fabricated (in the setting of a research laboratory) using a number of advanced nanolithographic techniques [3], such as Electron Beam Lithography (EBL) or focused-ion-beam (FIB) writing [4], proximal probe patterning [5], and X-ray or extreme-UV lithography [6], further development of these techniques into practical routes to large quantities of 1D nanostructures from a diversified range of materials, rapidly, and at reasonably low costs, still requires great ingenuity.

Currently, there are many well-established and successful methods of generating 2D and 3D nanoparticle assemblies with excellent uniformity and regularity compared with 1D systems. Principally, this is due to the relative ease of fabricating 2D/3D nanoparticle assemblies using chemical and physical methods. The construction of 1D nanoparticle assemblies on the other hand is considerably more challenging [7]. However, 1D nanoparticle assemblies are considered to be an important nanostructure for future novel

devices, which has incentivised researchers to find an ideal fabrication technique with rapid throughput capabilities. A plethora of synthesis methods for producing 1D nanoparticle assemblies now exist, from bottom-up to top-down approaches and hybrid techniques that exploit elements of self-assembly in conjunction with a top-down approach. Fabricating 1D nanoparticle arrays using top-down procedures, particularly EBL, has been extremely successful in engineering uniform, periodic and well-defined 1D nanostructures of feature sizes above tens of nanometers. However, EBL suffers from low-throughput and high cost. Bottom-up techniques are promising because very small particle sizes and separations, beyond the capabilities of EBL, can be fabricated in high-yield with relative ease and at low cost. However, chemical methods rarely match EBL for array uniformity and regularity. For chemical methods, the difficulty is associated with the dependence of interparticle molecular interactions. These must be manipulated in such a way that they create the necessary anisotropic interactions to drive the formation of 1D nanoparticle assemblies. Alternatively, templates, interfaces or field-assisted methods must be employed to direct the assembly of particles into 1D structures.

Colloid-electrospinning is a new field that offers the possibility to fabricate 1D nanocomposites containing blends of polymer with metallic nanoparticles. Metal nanoparticles present particularly attractive building blocks as starting materials to fabricate assemblies for future nanodevices with unique electronic and plasmonic properties [8-10]. Formations of these nanoassemblies are structures of closely separated nanoparticles that can exhibit emergent collective properties, which can be exploited in nanotechnology. Control over geometrical assemblies currently remains a great challenge in nanotechnology due to the complexity of organizing metal nanoparticles in low symmetry however colloid-electrospinning provides a cost-effective alternative [11].

1.2 POLYMERIC MICROSPHERES

Zero-dimensional (0D) micro/nano-structures for controlled release applications have received significant interest over the past couple of decades. Controlled drug delivery systems often consist of macromolecular carriers that transport therapeutic agents through the body to the desired site of action. Among the many forms that these carriers may take, solid, biodegradable polymer micro and nanoparticles are attractive systems that have been extensively investigated over the past few decades. Given the variety of fields of application of such colloidal objects – from nanomedicine, drug delivery and cosmetics, to printing ink and petroleum sciences, a thorough knowledge of the formulation processes is essential in order to achieve the given purposes and needs. The acceleration in the discovery of new therapeutic moieties (chemical, biological, genetic) has led to an increasing demand for delivery systems capable of loading, protecting, transporting and selectively targeting those agents to desired sites.

The predictions by Park et al. for the 3rd generation of controlled drug delivery technologies has provided evolutionary direction to the development of engineering a novel class of release systems [12]. One of the key challenges associated with (but not fully addressed by) the previous (2nd) generation is progression towards 'modulated delivery systems'. Delivering active molecules with the desired release kinetics requires an understanding of the physicochemical properties of the delivery vehicle and its release mechanism. Establishing performance metrics using *in vitro* models is considered the 'gold standard' approach preceding clinical investigation. It is vital to recognize the complexity associated with developing new release technologies and the simultaneous influence of multiple factors. Factors such as optimized formulation, manufacturability, materials, a suitable delivery route and the *in-*

vitro in-vivo correlation (IVIVC) to assist quality control can be considered as the benchmark prior to *in vivo* investigation.

The global market for microspheres has seen a steady growth rate in double digits in the last decade due to their use in healthcare, personal care, and in many speciality research and development applications [13]. They have been recognized as novel technologies for modulated release devices and have received significant interest from clinical communities. Polymeric microspheres are small spherical microparticles of a size ranging from 1μm to 1000μm that offer functionality for application-specific industries. They have a number of interesting attributes that make them particularly suitable for microencapsulation: (i) controlled release of encapsulated materials, (ii) protection of the encapsulated materials against degradative reactions which can also result in an improved shelf life and (iii) high surface-to-volume ratios [14,15].

Maintaining control of their homogeneous size, shape, skeletal porosity and reproducibility can dictate their performance in biological microenvironments. Encapsulation, biocompatibility and active agent release from microspheres are closely related to their structural properties. For example, the release rates of active molecules depend on the degradation of the polymer and/or diffusion of active molecules. This can be controlled by the molecular mass of the polymer, the microsphere size and also its porosity. The shape of a particle also influences its biocompatibility, for example, its interactions with macrophages [16-18].

Current methods for generating spherical, porous microstructures rely on techniques such as emulsion polymerization, thermal phase separation and spray drying. These techniques suffer from poor monodispersity, harsh solvent

toxicities, additives and costly starting materials not scalable for pharmaceutical industries [19-22]. Realizing a high degree of control over particle structure with a scalable, continuous spray process poses a challenge and provides the primary motivation for developing and demonstrating an electrospray synthesis method for continuous particle manufacture.

Both 1D and 0D structures mentioned above utilize electric field-assisted approaches to fabricate micro/nano-structures. Briefly, a high-voltage electric field can be imposed on a polymer liquid to form microspheres through electrospray or electrostatic assembly to fabricate nanofibres through electrospinning. The addition of an electric field results in charging the components of the system. The resulting electrostatic interactions either induce elongation of the charged polymer droplet or encourage droplet fission. Because electrostatic forces become meaningful at the micro/nano-scale, electrostatic generating technologies attract much attention in microfabrication or nanofabrication.

1.3 THESIS AIMS

The first half of this thesis will aim to manufacture composite 1D nanofibres using electrospinning techniques that demonstrate their potential application in nanoelectronics. Furthermore, electrospinning process parameters and solution properties (i.e. nanoparticle loading) will be varied to examine their influence on fibre morphology and electrical performance, respectively. Dark-field scanning transmission electron microscopy techniques will be used to reveal for the first time, the enhanced contrast of nanoparticles within polymer nanofibre matrices and expose the dispersion of nanoparticles within the polymer matrices.

So far several studies have successfully reported on the fabrication and characterization of polymer/ gold nanoparticle nanofibres although have failed to report the electrical performance of electrospun single nanowires [23-29]. Here we aim to address this and expose the potential of these electrospun composites in electronic nanodevices.

The second half of this thesis focuses on the controlled manufacturing of polymeric microspheres using ES atomization coupled with a novel thermally induced phase separation process (TIPS) and lyophilisation to enable their long-term storage. The physical properties of the microspheres have been investigated to examine whether the synthesis step has any physicochemical effects on the manufactured material and their potential as controlled release systems. Finally, an investigation into the performance of these microspheres as potential controlled release delivery vehicles will be examined using a dye as the encapsulated active agent.

1.4 THESIS STRUCTURE & OBJECTIVES

Chapter 1 has given an overview of the research project, the novelty and the aims. The scope of the research project are outlined and briefly the principle of operation of both electrospinning and electrospraying are discussed which are used for the generation of 1D and 0D micro/nano-structures.

Chapter 2 reviews the literature in detail, discusses the fabrication techniques used in this research and the key parameters, which govern their operation. Furthermore, the literature is surveyed to understand the techniques currently adopted for manufacturing polymer/nanoparticle composites for applications in nanoelectronics and the preparation of polymeric microspheres as vehicles for controlled release systems. It gives an account of past research, observations of the present state-of-the-art research in this field and situates the work done in this thesis within the research efforts in the field. Chapters 1 and 2 are intended for review, whereas the remaining chapters are original to this thesis.

Chapter 3 describes the experimental section covering: the materials, apparatus, synthesis and fabrication techniques used to manufacture the micro/nano-structures. Furthermore the chapter discusses the characterization techniques employed throughout the study along with the practices used for sample preparation.

Chapter 4 discusses fabrication of the polymer/nanoparticle composites and the approaches used to optimize the electrospinning process for manufacturing nanofibres. It briefly covers nanoparticle synthesis along with microscopic and optical characterization of the nanoparticles. Finally, a detailed characterization study is provided covering the microscopic techniques used to image the composite morphologies.

Chapter 5 investigates the electrical performance of the fabricated polymer/nanoparticle composite fibres prepared in Chapter 4. Measurements of resistive switching are presented and the results are discussed, varying both the nanoparticle loading concentration and electrode materials.

Chapter 6 describes the scaling law and recipe used to estimate and manufacture PLGA microspheres of specific size. The characterization techniques used for analytical purpose are discussed and the influence of key process parameters on the size and morphology of the novel particles.

Chapter 7 describes the methods used for particle functionality tests, i.e. *in vitro* release studies. Primarily the influence of microsphere size on the release of an active agent is investigated and the results are correlated with the cumulative release profile of each particle size (and its porosity). Furthermore, image analysis pre- and post-dissolution test examine whether active ingredient loading has influenced particle morphology.

Chapter 8 concludes this thesis and suggests recommendations for future work.

2. LITERATURE REVIEW

PART A

2.1 NANOFIBRE FABRICATION TECHNIQUES

2.1.1 NANOFIBRE DEFINITION

It is essential to define what a *nanofibre* is prior to discussing the ways in which they can be fabricated. To do so, we split the term into two parts, namely “nano” and “fibre”. Nano is derived from the Greek word, “nanos”, translating to “dwarf, simply meaning something very small. When quantified, it translates to one-billionth of one [30]. Historically, the term “fibre” comes from Latin “fibra” [30]. In this thesis, a “fibre” is defined from a geometrical standpoint - a slender, elongated, thread-like object or structure. Anatomists tend to understand fibres as any of the filaments constituting the extracellular matrix of connective tissue, the textile industry views fibres as a natural or synthetic filament, such as cotton or nylon, capable of being spun into yarn, or simply a material made of such filaments. In this thesis, a fibre will be recognized as a polymer-based 1D structure with high aspect ratio.

2.1.2 DRAWING

Drawing has previously offered a method of fabricating suspended micro/nano-fibres continuously, in which polymeric micro/nano-fibres are formed by drawing and solidification of a viscous liquid polymer solution, which is pumped through a glass micropipette. By controlling the drawing parameters, this method is demonstrated to form networks of suspended fibres having amorphous internal structure and uniform diameters from micrometers down to sub-50-nm [31]. Generally a micropipette with a diameter of a few micrometers is dipped into a droplet near the contact line using a micromanipulator. The micropipette is then withdrawn from the liquid and moved at a constant speed of approximately $1x10^{-4}$ m/s, resulting in a nanofibre being pulled. The pulled fibre is deposited on the surface by touching it with the end of the micropipette, as seen in Figure 2.01. Drawing a fibre requires a viscoelastic material that can undergo strong deformations while being cohesive enough to support the stresses developed during pulling [32, 33]. Although the process is convenient due to its simplicity and also repeatability, it is difficult to control fibre dimensions and the process is discontinuous therefore cannot be scaled, as it relies on batch-type processes.

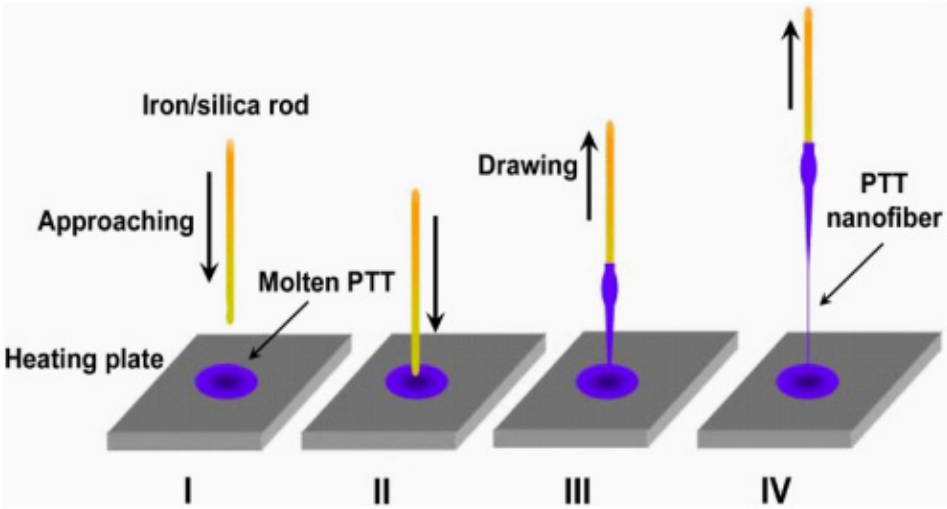

FIGURE 2.01. Schematic illustration of nanofibres fabrication by direct drawing process from molten poly(trimethylene terephthalate) (PTT). (I) An iron or silica rod is approaching the molten PTT. (II) The rod end is immersed into the molten PTT. (III) The rod conglutinated PTT is being drawn out. (IV) A PTT nanofibre is formed. [Taken from 32]

2.1.3 TEMPLATE SYNTHESIS

Template synthesis is a technique used to make a variety of templates for the alignment and production of nanofibre assemblies. This bottom-up approach can make use of universally available materials and nearly all-solid matter can in principle be synthesised within nanoporous templates, as long as a suitable chemical pathway can be developed. However, a major consideration with the template mechanism is whether the template remains stable with respect to the reaction conditions. One representative strategy of template synthesis of nanostructures is using electrochemical deposition [34]. Electrodeposition of a material is preceded by coating one face of the template with a metal film and

using this metal film as a cathode for electroplating, as shown in Figure 2.02. The volume of the pore is continuously filled up beginning from the pore bottom. Thus, the length of a nanostructure can be controlled by varying the amount of material deposited. Nanorods have also previously been synthesized using this method [35].

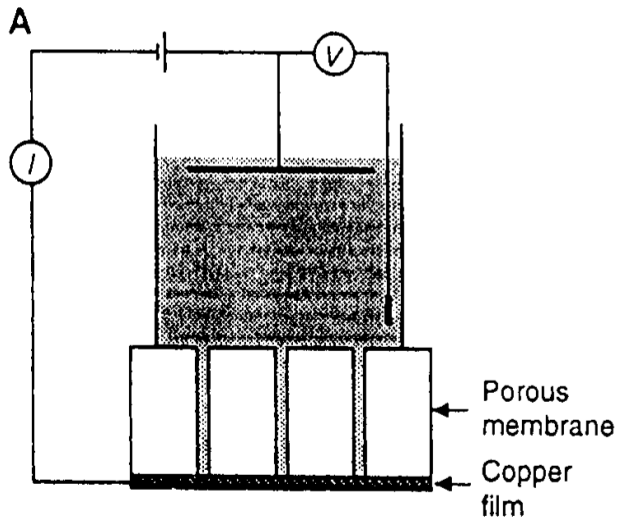

FIGURE 2.02. Illustration of the electrode arrangement for electrodeposition of Ni and Co nanowire assemblies. [Taken from 34]

Template-based synthesis, in general, is a straightforward way of producing nanostructures, which requires a suitable deposition method and a sacrificial substrate having the desired geometry. However, the most obvious constraint of template synthesis is the limited control over the properties of resulting structure (e.g. crystal structure, dimensions, etc.) [36-40]. Another key limitation of this method is the selected template material should not only be resistant to the growth ambient (i.e. temperature, pressure and gases), but should disappear with a simple post-deposition treatment as well, unless it has

a function in the final structure [36]. Although studies have proven the flexibility of the technique to manufacture nanofibres from a range of materials [36-40], the technique is confined to the laboratory and cannot be scaled for industrial processing.

2.1.4 ELECTRON BEAM LITHOGRAPHY (EBL)

Electron Beam Lithography (EBL) is an ideal top-down approach that can precisely fabricate nanostructures with dimensions down to tens of nanometers and enable direct control over the nanostructure geometry. It is versatile and provides high resolution and precise control over the geometry for manufacturing well-defined arbitrary element shapes and array configurations, including nanofibre-like filaments. It is a direct pattern transfer technique that enables control over the separation of nanostructures, guaranteeing a fabrication reproducibility and precision down to the nanometer scale [41, 42].

The technique scans a focused beam of electrons to produce shapes, specific in size and morphology. It is considered a powerful tool for the fabrication of linear metallic nanostructures for applications in nanoelectronics and plasmonics and is an ideal candidate for demonstrating control over particle separation [43]. The ultimate resolution is better than 10 nm [43], and the technique is highly flexible. The flexibility originates from the fact that the electron-beam is scanned over the surface by a programmable pattern generator, so that the method does not rely on pre-fabricated masks.

The technique has been explored particularly for fabricating structures for micro/nano-electronics and additionally it remains the tool of choice for fundamental studies of plasmonic nanostructures. Many plasmonic nanostructures actually require relatively large nanostructures that are above

the resolution limits of EBL. For example, plasmonic waveguides consisting of gold (Au) nanoparticle chains with well-defined gaps and homogeneous nanoparticle sizes and shapes can be routinely fabricated using EBL, as shown in Figure 2.03 [44].

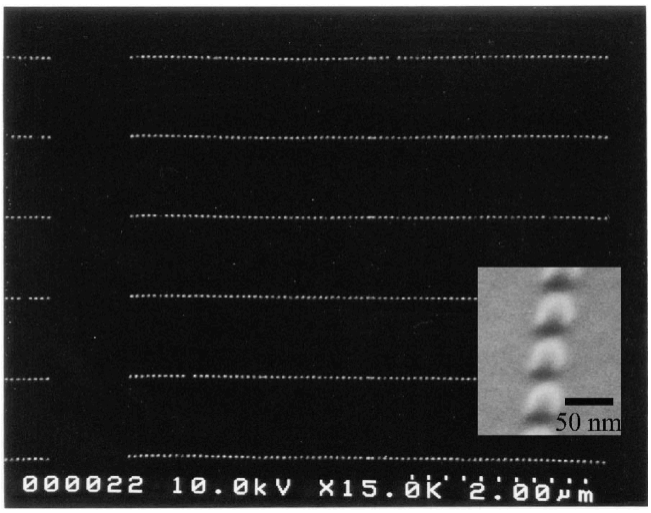

FIGURE 2.03. Scanning electron micrograph (SEM) of plasmonic waveguides consisting of Au nanoparticles taken at a normal incidence of the electron beam. The inset shows a micrograph where the sample stage was tilted by 70° to visualize the almost spherical shape of the nanoparticles. The nanostructure is 80 Au particles long with diameters of 50 nm and interparticle separations of 75 nm. [Taken from 44]

Previously, linear arrays of silver (Ag) nanoparticles have been fabricated by EBL to construct multiple samples on a substrate offering precise control over particle size and spacing (as seen in Figure 2.04) [45, 46], although a major problem of the direct-write method in this study revealed the serial nature of the process and the higher costs associated with production of such linear

arrays. Despite the success of the technique, the process is very slow in producing linear arrays of nanoparticles.

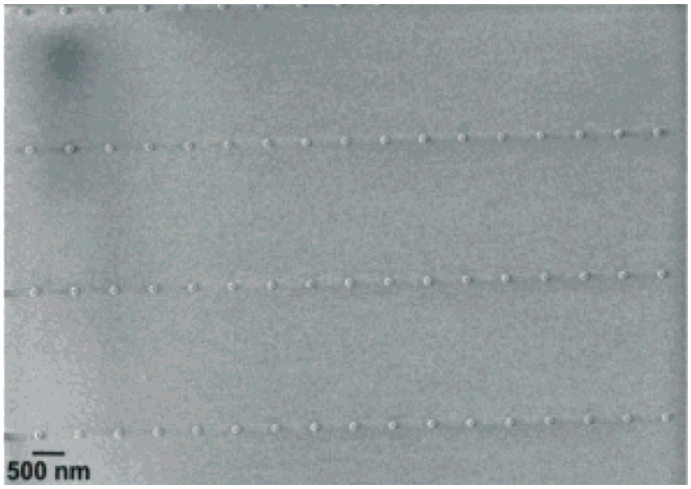

FIGURE 2.04. SEM image of linear arrays of Ag nanoparticles on glass with an interparticle spacing of 632 nm, diameter = 130 nm, height = 30 nm. [Taken from 45]

Inherently the EBL method of fabrication suffers from several apparent drawbacks, which make it a difficult long-term solution for manufacturing particle arrays for nanotechnology applications. Firstly, the electron beam must be scanned across patterned areas pixel-by-pixel and therefore single or multiple exposures can take many hours to complete. Secondly, conventional fabrication techniques such as metal lift-off and etching can become difficult at sub-micron length scales. Finally, EBL systems are generally expensive and highly complex machines requiring substantial maintenance over a long period of time.

There is a clear need for a technique that offers a rapid throughput eliminating

the need for the direct deposition of particles and alternatively encapsulates the nanoparticles within a sacrificial polymer template that either enhances the processing capability of the technique or the end-functionality. The solution must combine the merits of increased throughput, scalability, control over structure and morphology of nanostructured arrays and simplicity with the low-cost element and user-friendly needs of the technique.

2.1.5 SELF-ASSEMBLY

Nanomaterials such as nanofibres can in principle, be made using both top-down and bottom-up techniques. Self-assembly bridges these two techniques and allows materials to be designed with hierarchical order and complexity that mimics those seen in biological systems. Self-assembly of nanostructured materials has demonstrated promise as a low-cost, high-yield technique with a wide range of scientific and technological applications. In general terms, self-assembly refers to the construction of structures using smaller molecules as the basic building blocks, in this case, the structures being nanofibres. It enables structures (of any size, especially nanostructures) synthesized bottom-up to organize themselves into regular patterns or arrangements by using local forces to find the lowest-energy configuration, and to guide this self assembly using templates fabricated top-down [47].

Manufacturing nanofibres using self-assembly has been demonstrated using polymers and also now DNA chains in a one-step synthesis protocol [48, 49]. Here, nanofibres were synthesized when a small molecule is arranged in a concentric manner such that the bonds can form among the concentrically arranged molecules, which, upon extension in the plane's normal gives the longitudinal axis of a nanofibre, as seen in Figure 2.05.

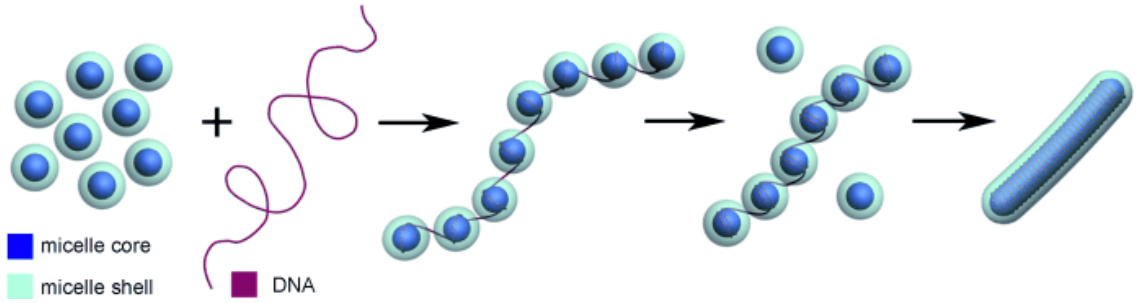

FIGURE 2.05. A schematic representation of the self-assembly process of linear DNA and the core-shell micelles. [Taken from 49]

The self-assembly process can also be adapted to nanoparticles [50, 51], although their synthesis poses a challenge owing to their size, shape and interaction with molecules. The complexity associated with repeating such structures consistently requires 'matched' conditions that enables their repeatability and supports the need for an effective technique that enables their directed assembly in ambient conditions. Fabricating one-dimensional nanostructures using self-assembly not only requires an understanding of the complexity of the process itself, but more attention to the fundamental thermodynamics, kinetics, and mechanisms involved in the process.

2.2 HISTORY – ELECTROSTATIC SPINNING

In 1600, William Gilbert made the first official report of electrostatic attraction of a liquid solution [52]. After Gilbert had observed that rubbed amber exerts an attractive force on a liquid that is not transmitted by movements in the air, he wrote: "indeed it plainly does draw the body itself in the case of a spherical drop of water standing on a dry surface; for a piece of amber is applied to it at a suitable distance pulls the nearest parts out of their position and draws it up into a cone; otherwise, if it were drawn by means of the air rushing along, the

whole drop would have moved" [52]. It is this first recording of the deformation of a drop of liquid (that would eventually be referred to as the Taylor cone), becoming the defining observation of the electrospinning process.

In was during the late 1800s that electrodynamics was used to explain the excitation of a dielectric liquid under the influence of an electric charge, which eventually led to the invention of electrospinning in the 1900s. John Francis Cooley, a professional inventor and electrician, filed for the first electrospinning patent in which he patented a set-up that used auxiliary electrodes to direct and guide the jet onto a rotating collector [53]. Despite the efforts of Cooley, it was not until 1934 that electrospinning appeared as a newly developed fabrication technique for spinning ultra-fine fibres [54].

Anton Formhals patented his first invention in 1934 (Figure 2.06) relating to the process and the apparatus for producing artificial filaments using electric charges [54, 55]. Although the methodology of producing artificial threads using an electric field had been experimented and tested for a long period of time, it had not gained importance until Formhal's invention due to some technical difficulties in the earlier spinning methods, such as fibre drying and collection onto substrates. Regardless of the drawbacks during this period, Formhals came up with several innovative set-ups to produce yarns made out of electrospun fibres without the use of a spinneret [53]. Formhal's process was capable of producing threads aligned parallel on to the receiving device in a manner that allowed it to be unwound continuously.

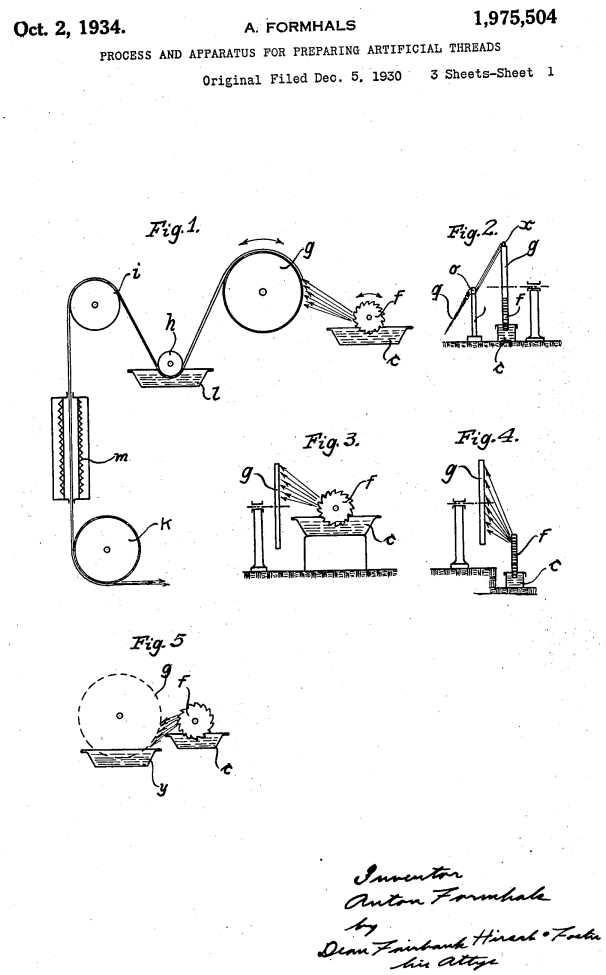
Oct. 2, 1934. A. FORMHALS 1,975,504

PROCESS AND APPARATUS FOR PREPARING ARTIFICIAL THREADS

Original Filed Dec. 5, 1930 3 Sheets-Sheet 1

Fig. 1.

Fig. 2.

Fig. 3.

Fig. 4.

Fig. 5

Inventor
Anton Formhals
by
Dean Fairbank Hirsch & Fosdick
his Attys

FIGURE 2.06. Formhals patent registered on October 2nd 1934 illustrating the process and apparatus for preparing artificial threads.
(US PATENT 1,975,504) [Taken from 54]

It was not until the 1960s that Sir Geoffrey Ingram Taylor initiated further theoretical studies of the fundamental processes of jet formation [56]. In his later years, between 1964 and 1969, he made significant progress in the

theoretical underpinnings behind the electrospinning process. The studies carried out by Taylor during this period contributed to mathematical models of the shape of the cone formed by the fluid droplet under the influence of an electric field; the term coined by Taylor himself for the characteristic droplet shape was the 'Taylor cone' [56]. Up until the early 1990s, very little work had been undertaken on the technique, although since then the increase in the number of publications using a variety of polymers is evidence of a dramatic increase in the popularity of electrospinning globally [57, 58].

2.3 ELECTROSPINNING OPERATION

Electrospinning is a simple and effective technique that enables the production of tiny nanofibres with complex shapes, functions, topologies and nonwoven systems. The process involves the drawing of fluid, either in the form of molten polymer or polymer solution. The drawing of nanofibres occurs when sufficiently high electric fields are applied to a polymer droplet at the exit of an orifice (typically a blunted stainless steel hypodermic needle) inducing the build up of charge (on the droplet surface) to encourage uniaxial stretching of the solution. Typically, when charges in the fluid reach a critical amount, a fluid jet will erupt from the droplet at the tip of the needle resulting in the formation of a Taylor cone. The electrospinning jet will travel towards the region of lower potential, usually an electrically grounded collector substrate [59-61].

The electrospinning process is driven by the electrical forces of free charges on the surface or inside a polymeric liquid [57]. In conventional spinning, the fibre is subject to tensile, rheological, gravitational, inertial, and aerodynamic forces. In electrospinning the tensile force is generated by the interaction of an applied electric field with the electrical charge carried by the jet rather than by the spindles and reels used in conventional spinning [57].

A stable electrospinning jet has four distinct regions, a typical set up can be seen in Figure 2.07. The jet emerges from the charged surface at the emitter region, travels through the jet region, divides into many fibres in the splaying region, and is deposited in the collection region [57].

1. The *emitter* is the region where the jet emerges from the liquid polymer. The geometry of the jet, near the emitter, is a tapered cone in which the axial velocity of the liquid increases as the polymer is accelerated along the axis of the jet. An electric field at the surface of a liquid produces a force that, if the electric field is strong enough, a jet of liquid can be ejected from a surface that was essentially curved before the field was applied. The electrical charging of the jet occurs in the vicinity of the emitter. The electrical conductivity of typical polymers is large enough to supply the small currents that are required for electrospinning [57, 62].

Taylor showed that a conical shaped surface referred to as the Taylor cone with an angle of 49.3° is formed when a critical potential is reached to disturb the equilibrium of the droplet at the tip of the capillary, that is, the initiating surface [56]. When a high potential is applied to the solution, electrical forces and the surface tension help in creating a protrusion wherein the charges accumulate. The high charge per unit area at the protrusion pulls the solution further to form a conical shape, which on further increase in the potential initiates the electrospinning process by jetting [56, 57].

2. The *jetting* region beyond the base where the electrical forces continue to accelerate the polymer liquid and to stretch the jet. In this region, the diameter of the jet decreases and the length increases in a way that keeps constant the amount of mass per unit time passing any point on the axis [59]. A stable electrospinning jet travels from a polymer solution or melt to a collector, e.g. a

metal substrate. The jet is driven by a high electrical potential applied between the solution or melt and the collector. Electrical charges, usually in the form of ions, tend to move in response to the electrical field that is associated with the potential. The charges, which have drift velocities through the liquid polymer that are smaller than the velocity of the jet along its axis, transfer the forces from the electric field to the polymer mass [61]. The Coulombic forces which stretch the fibre are resisted by the viscoelastic forces of the solution [57, 61].

The acceleration of the polymer in the jet is mediated by the transfer of the forces throughout the viscoelastic solution [61]. The charges in the jet carry the liquid polymer in which the charge is embedded in the direction of the electric field. This is the mechanism which moves charge from the reservoir of liquid polymer to the collector, and thereby completes an electrical circuit which provides the energy needed to accelerate the polymer, to increase its surface area, and to drive the flow and deformation processes which change the shape of the liquid into a jet [57, 61].

3. *Splaying* occurs in a region in which the radial forces from the electrical charges carried by the jet become larger than the cohesive forces within the jet, and the single jet divides into many charged jets with approximately equal diameters and charge per unit length. As the jet progresses from the base toward the collector, the forces from the external electric field accelerate and stretch the jet. Stretching and evaporation of the solvent molecules cause the jet diameter to become smaller [55, 57]. The charge on the fibre tends to expand the jet in the radial directions and to stretch it in the axial direction. As the radius of the jet becomes smaller, the radial forces from the charge can become large enough to overcome the cohesive forces of the fibre and cause it to split into two or more fibres, that is to splay. This jet division process occurs several more times in rapid succession and produces a large number

of small electrically charged fibres moving toward the collector [55, 57, 61]. Splaying converts a single jet into many much thinner jets. Thin fibres are also created by elongating a single jet if splaying does not occur, although splaying and elongation occur simultaneously in many cases [57].

4. The *collection* region is where the jet is stopped and the fibres are subsequently deposited. The polymer fibre that remains after the solvent evaporates may be collected on a metal screen. For polymers dissolved in non-volatile solvents, water or other appropriate liquids can be used to collect the jet, remove the solvent, and coagulate the polymer fibre [57, 63].

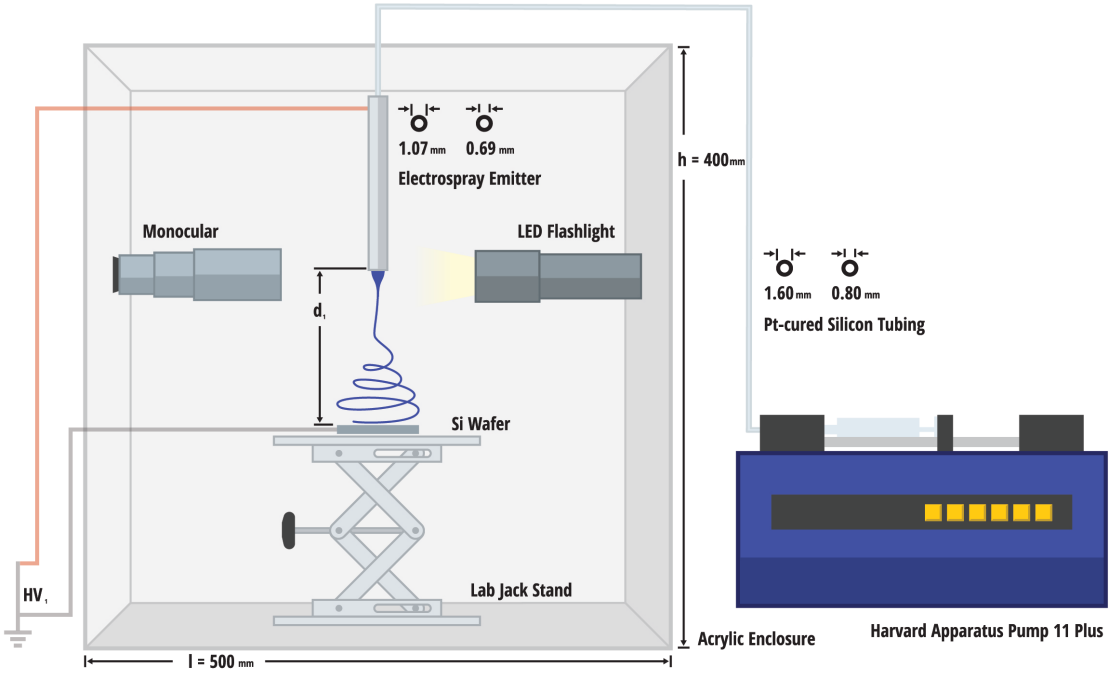

FIGURE 2.07. Schematic of a typical electrospinning configuration used for the generation of ultra-thin fibres.

2.3.1 SOLUTION PROPERTIES

The properties of the polymer solution have the most influential effect on the electrospinning jet, process and the overall fibre morphology and structure. The concentration, viscosity, surface tension and electrical conductivity will determine the extent of elongation of the jet and the viscoelastic solution. These properties of the solution collectively determine the diameter of the electrospun fibres.

2.3.1.1 CONCENTRATION, VISCOSITY AND MOLECULAR WEIGHT

The viscosity of a solution is directly related to the concentration of polymer and is well known to have a direct effect on the fibre diameter and its morphology [64]. Solution viscosity, as controlled by varying the polymer concentration has been studied on a number of different polymer systems, including poly(DL-lactic acid) (PDLA) [65], poly(lactic-co-glycolic acid) (PLGA) [66], poly(ethylene oxide) (PEO) [67, 68, 69], and poly(vinyl alcohol) (PVA) [70]. A study by He *et al.* [71], concluded that the diameters of electrospun nanofibres are greatly affected by solution viscosity, and conclusively the solution viscosity has a proportional relationship with its concentration [71]. At lower polymer concentrations, defects present in the form of beading and droplets have been observed [65, 67, 69]. In contrast, increasing the concentration (i.e. the viscosity) of the solution yields uniform fibres with few beads and junctions [67].

In a study by Jacobs *et al.* [72], in which the concentration of PEO was varied, notable changes were observed in the morphology and diameter of electrospun fibres. Increases in fibre diameter were noted as the

concentrations of the solutions were increased [72]. Their results of mean fibre diameter showed a similar trend; the mean values increased with increasing PEO concentration. This is attributed to the higher viscosity of the solution, which was strong enough to prevent the bending instability from setting in for a longer distance as it was emerging from the spinneret. As the viscosity increases, the electrospun fibres have larger diameters due to the higher entanglement of the polymer chain in the solution and also the greater physical resistance of the polymer when it is stretched by the electrical charges [72].

The molecular weight of the polymer represents the length of the polymer chain, which in turn has an effect on the viscosity of the solution as it is the polymer length that determines the amount of entanglement of the polymer chains in the solvent. Another way to increase the viscosity of the solution is to increase the polymer concentration. Similar to increasing the molecular weight, an increase in the concentration will result in greater polymer chain entanglements within the solution, which is necessary to maintain the continuity of the jet during electrospinning [30, 70].

2.3.1.2 SURFACE TENSION

Surface tension is the resistance of a liquid to external forces. It can be understood simply by taking the case of a droplet of water. In the case of a liquid molecule in solution, there will be uniform attractive forces exerted on it due to the other liquid molecules surrounding it [30]. For liquid molecules at the surface of the solution, there will be a net downward force as the liquid molecules below exert a greater attractive force above. This leaves the surface in tension causing a contraction at the surface of the solution, which is balanced by the repulsive forces that arise from the collisions of molecules from the interior of the solution. The overall effect of pulling of all the surface

liquid molecules causes the liquid surface to contract, thereby reducing the surface area. Therefore, for the case of a droplet of water, a spherical shape is the lowest surface area to volume ratio [30]. The initiation of electrospinning requires the charged solution to overcome its surface tension. However, as the jet travels towards the collection plate, the surface tension may cause the formation of beads along the jet.

The choice of solvent contributes to different surface tensions and tends to play a key role in the electrospinning process. A high surface tension of a solution can inhibit the electrospinning process due to jet instability and production of droplets (i.e. electrospraying) [59]. Solvents such as ethanol have a low surface tension thus it can be used in polymer solutions to encourage the formation of smooth fibres [68].

2.3.1.3 SOLUTION CONDUCTIVITY

Electrospinning is caused by surface charges on the spinning solution and it is clear that, if the conductivity of the solution is increased, more charges can be carried by the electrospinning jet. The type of polymer, solvent and the availability of ionisable salts determine the solution conductivity and by the addition of ions (i.e. salts) to the solution, the conductivity increases. It has been found that with the increase of electrical conductivity of the solution, a significant decrease in the diameter of electrospun fibres has been observed whereas at lower conductivities, elongation of the jet by the electrostatic forces fails to produce uniform fibres and results in bead production. However, there is a limit to the reduction in fibre diameter. As the solution is stretched, there is a greater viscoelastic force acting against the Coulombic forces produced by the charges. Another crucial effect of increased charge is the greater instability of the jetting process, which results in fibres being deposited over a larger

area, giving less control over the process [73].

Another method to increase solution conductivity is the addition of alcohol to the solvent. This has produced fibres with fewer beads [68, 73]. The addition of cationic surfactants however, such as dodecyltrimethylammonium has also been shown to reduce beading on fibres. This reduction in beading was attributed to the ability of charged surfactants to increase solution conductivity and reduce the whipping instabilities of the jet [74].

2.3.2 PROCESS PARAMETERS

From the prior descriptions of electrospinning theory and operation, it is evident that numerous variables can affect the electrospinning process and the final fibre morphologies, dimensions and properties. These parameters will directly influence the morphology of the resultant electrospun fibres, from beaded fibres to fibres that have pores integrated onto their surface [75].

The process parameters, which are also known as the operational conditions, are the variables that the operator has greater control over, as opposed to the ambient environmental conditions and the solution properties. The operational conditions such as the applied voltage (i.e. electric field strength between tip and collector), the flow rate and the distance (between the needle and collector) are the three primary parameters that govern the process, although additional variables such as the shape and size of the collector screen and needle gauge are often also considered but rarely reported [75].

2.3.2.1 APPLIED VOLTAGE – ELECTRIC FIELD STRENGTH

One of the most studied parameters in electrospinning is the applied voltage

(i.e. the electric field). It is responsible for the induced charges on the solution. This variable is principally responsible for the initiation of electrospinning and the process occurs at a critical voltage whereby the electrostatic forces in the solution overcome its surface tension. Generally higher field strengths (either positive or negative) are able to influence the solution droplet at the tip of the needle to distort into a Taylor cone [56]. The Coulombic repulsive forces in the jet are responsible for stretching the viscoelastic solution into ultra-thin fibres. At greater applied voltages, these forces will increase the strength of the electric field; a subsequent increase in charge will cause the jet to accelerate faster, and a greater volume of solution can then be drawn from the needle orifice. At higher applied voltages, the Taylor cone is less stable and smaller in size, which causes greater jet instability. There must be a balance between the flow rate and the voltage as the Taylor cone can recede into the needle if the extraction of the solution towards the collector plate is quicker than the supply from the polymer source [67].

The field-induced stretching of the solution, has the effect of reducing the diameter of the fibres, and also favors faster solvent evaporation, which produces dried fibres upon deposition [76]. At lower voltages, there will be a weaker electric field between the electrodes, and hence the drawing rate will be reduced, leading to a greater flight time to the collector screen. This allows more time for the fibres to stretch, meaning thinner fibres will be produced [77]. More importantly, it must be noted that there is a greater tendency at higher voltages to the formation of beads on the fibres, and that the shape of the beads change from spindle-like to spherical-like with stronger electric fields [67]. This increased bead formation may be down to an increased instability of the jet as the Taylor cone recedes into the needle and hence a lack of ‘stretching’ produces spontaneous beads on the fibres. High voltages not only affect physical appearances of the fibres but also crystallinity [77]. The

field can cause polymer molecules to form order, thus increasing crystallinity.

2.3.2.2 FLOW RATE

The flow rate, also known as the feed rate, from the syringe is an important process parameter that influences the jet velocity and the transfer rate of the material through the needle to the collector and can be expressed in mL/hr, mL/min, mL/sec etc. In order to maintain a stable Taylor cone, there will be a critical flow rate and applied voltage. Lower feed rates are more desirable as the fibre has a greater flight time and, as a result, the solvent will have a longer time to evaporate [78].

It has been observed that the fibre diameter and the pore size increases with an increase in the polymer flow rate in the case of polystyrene (PS) fibres and by changing the flow rate, morphology can be controlled. Megelski *et al.* noted, as flow rates increased, fibres had pronounced beaded morphologies and the mean pore size increased from 90 to 150nm [79].

2.3.2.3 SPINNING DISTANCE

For the controlled fabrication of fibres, the polymer jet should be given a sufficient distance and time (i.e. flight time) for the solvents to evaporate. As the distance between the tip and collector is decreased, the jet covers a shorter distance and will therefore contain traces of solvent upon deposition. Consequently, the electric field strength increases with shorter distances, resulting in greater acceleration of the jet to the collector. Excess solvent can cause fibres to merge together to form junctions that can result in inter- and intra- layer bonding, noted in a study by Buchko *et al.* [80].

2.4 ELECTROSPUN NANOPARTICLE/POLYMER COMPOSITES

In the following section, a brief background of the current progress on electrospun nanoparticle/polymer composites will be discussed including their synthesis, properties and applications. An emphasis on polymer/metallic nanoparticle systems, particularly Au nanoparticles, will be taken as these are most appropriate to the research in this thesis and in many cases a similar protocol can be used for other noble metals as the technique is adaptable for processing a host of nanomaterials.

Nanoscopic processing of polymer-nanoparticle composite materials has attracted a great deal of interest due largely to their unique physical and chemical properties. Metal nanoparticles present particularly attractive building blocks as starting materials to fabricate assemblies for future nanodevices with unique electronic, optoelectronic, and plasmonic properties [8-10]. The physical properties of these nanodevices are regulated by the formation of size-controlled nanoparticles, inter-particle separation and control over geometrical assemblies although their fabrication currently remains a great challenge in nanotechnology due to the complexity of organizing metal nanoparticles in low symmetry [7, 11, 81-89]. Their synthesis poses substantial challenges owing to their formulation complexities, scalability and associated costs.

A number of reviews have been published demonstrating the success of electrospinning colloidal suspensions in polymer nanofibres [90-93]. The dispersion of the inorganic nanocomponent in polymer solution has yielded a straightforward process of manufacturing linear composites (via electrospinning) with multifunctional properties. Previously other nanomaterials,

such as gold nanorods (AuNRs), have been electrospun in poly(vinyl alcohol) (PVA) nanofibres to form free-standing, flexible mats with tunable optical properties, as seen in Figure 2.08. The mats served as a surface-enhanced Raman scattering (SERS) substrate with high sensitivity and large-area uniformity [94]. Additionally, PVA nanofibres have been electrospun into free-standing SERS substrates containing silver nanoparticles (AgNPs) [95].

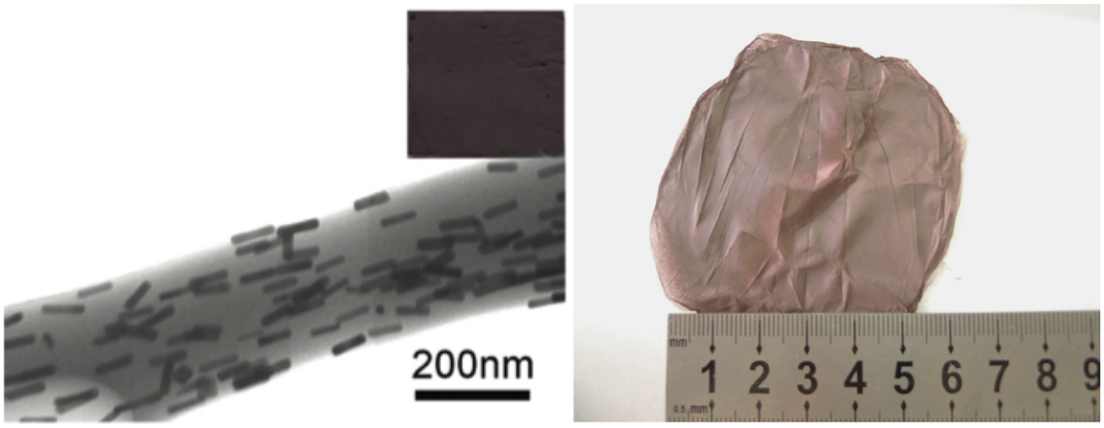

FIGURE 2.08. TEM image (left) of AuNRs assembled within the PVA nanofibres. (Inset is the corresponding photograph of the nanofibre mat). (Right) Photograph of Au/PVA nanofibre mat (with AuNR concentration of 200 nM) produced by electrospinning for 1 h. [Taken from 94]

Lim and co-workers revealed how fibre thinning (during electrospinning) could be used to manufacture 1D colloidal assemblies of monodisperse silica particles at a range of different sizes (including 100 nm, 300 nm, 450 nm, 700 nm and 1 μm). As the composite fibre becomes thinner during electrospinning, the particles are arranged into 1D colloidal assemblies and are confined within the nanofibre geometry. Particle assemblies are obtained after removing the polymer matrix by thermal decomposition [96]. Additionally, Saquing *et al*.

used PEO as the sacrificial template to manufacture 1D assemblies of AgNPs via a one-step synthesis process and investigated the effect of molecular weight (at 600, 1000 and 2000 kDa) to enhance fibre quality (i.e. reduce beading). The polymer was used as the reducing agent for the metal salt precursor to manufacture linear arrays of AgNPs [97]. This procedure circumvents the necessity of separately synthesizing and isolating uniform and stabilized colloids in solution to combine with the polymer and potentially overcomes nanoparticle-aggregation effects. Moreover, it eliminates the need of using conventional chemical, thermal, or radiolytic reduction treatments and the addition of protecting agents.

The incorporation of AgNPs in the solution tremendously improves the fibre quality through reduction in fibre diameter and in bead formation. This fibre quality improvement is attributable to the increased electrical conductivity in the electrospinning solution upon the incorporation of nanoparticles. Several studies have investigated the effect of loading solutions with metallic AuNPs for fabricating linear arrays of nanoparticles (as seen in Figure 2.09) [23-29], although have failed to report the electrical performance of the electrospun fibres and their applications in nanoelectronic devices. Here we aim to address this and expose the potential of these electrospun composites in electronic nanodevices.

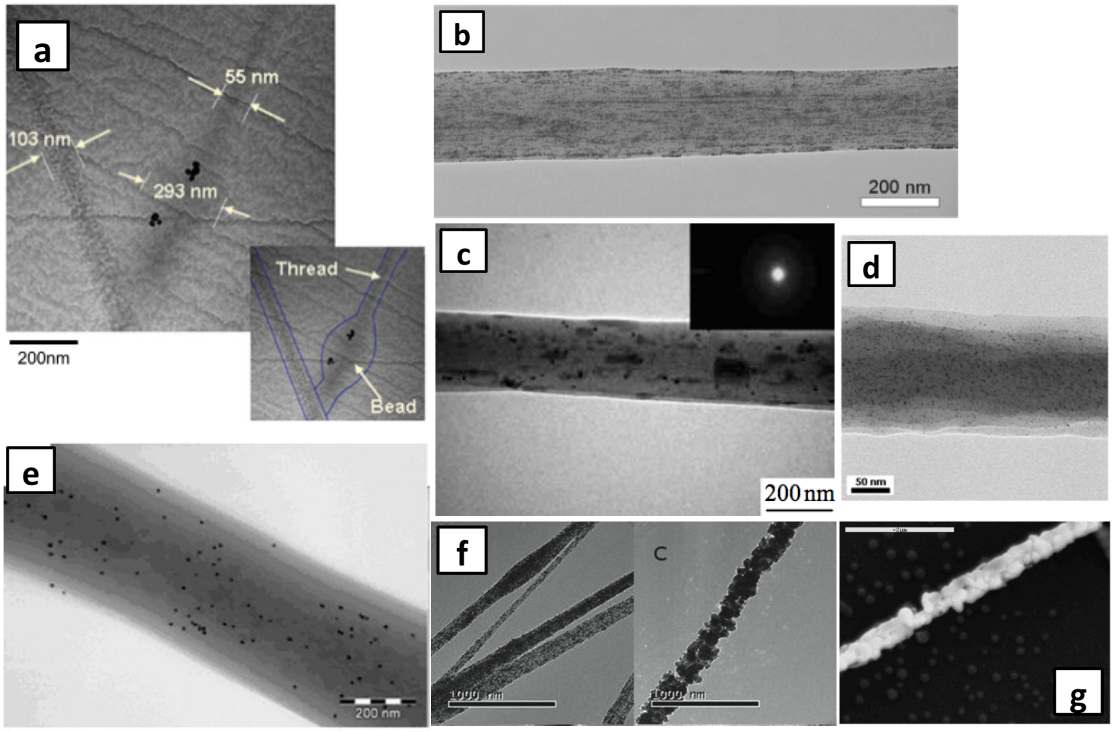

FIGURE 2.09. TEM images showing (a) the presence of Au nanoparticles in PEO 'beads' [Taken from 23], (b) 1D chainlike arrays of AuNPs in PEO fibres [Taken from 24], (c) AuNP/ Polyacrylamide (PAM) nanofibres [Taken from 26], (d) AuNP/Polystyrene (PS) composite nanofibres [Taken from 28], (e) AuNP/PVA composite nanofibers [Taken from 25], (f) electrospun AuNP/PVA composite fibers after annealing in air [Taken from 27], and (g) HR-SEM image of the Au nanowire. [Taken from 29]

Previously, Kim *et al*. and Hamlett *et al*. electrospun passivated colloidal gold nanosuspensions in PEO and found that the incorporation of nanoparticles suppresses the fibre diameter (i.e. 290 mm down to 55 nm) as well as increases the degree of crystallinity. TEM analysis of the smallest fibres reveal that the AuNP distribution within the fibres is more concentrated in the 'beaded'

regions of the composite fibres [23, 24]. Additionally, the preparation of polymer/nanoparticle solutions involved stirring the inorganic nanosuspension with the polymer although this can induce aggregation of nanoparticles. Aggregation will negate the effects that individual nanoparticles have on the electrical and optical properties of the composites. Control over inter-particle distance should be consistent and therefore homogenization is encouraged to influence particle break up and avoid particles aggregating into bulk materials. More importantly, the solvents used to prepare the polymer solution and nanoparticle suspension should be the same or miscible to ensure the colloidal suspension is microscopically dispersed in the polymer and is mixed in all proportions. Immiscible solutions are difficult to electrospin and have uncontrollable surface tension effects with non-linear behaviours.

Finally the post-processing of polymer/AuNP blends has a crucial effect on the linear array and its properties. Gries and co-workers and Pol Kim *et al*. previously used sintering on the electrospun fibres to sinter away the polymer template and leave gold nanowires [27, 29]. Here, highly concentrated aqueous dispersions of AuNPs were obtained in the presence of PVA. PVA/AuNP composite fibres were prepared by electrospinning, followed by pyrolysis of PVA and simultaneous formation of the gold wires by sintering of the AuNPs [27]. The PVA stabilized highly concentrated dispersions of AuNPs against aggregation. These dispersions were used for the preparation of PVA nanofibres with a high content of non-aggregated AuNPs [27].

2.4.1 ELECTRICAL APPLICATIONS

Nanoelectronics based on 1D nanomaterials (such as nanotubes, nanowires or nanofibres) are considered promising candidates for the scaling-limiting problem in semiconducting manufacturing technology. Electrically functional electrospun materials have attracted significant interest in recent years because of their potential applications in electronic devices [98-101]. Electrospun composite nanofibres/nanowires potentially represent important building blocks for nanoscale electronics, optoelectronics, and photoluminescence since they can potentially function as miniaturized devices as well as electronic interconnects. The large surface-to-volume ratio and high electron–hole conductivity along the quasi-1D structure and high aspect ratio of nanowires makes them ideal candidates for use as printing nanoelectronic tracks with cost-effective fabrication/printing technology. Performance improvement of electrospun components results from the unique properties associated with nanometer-scaled features, high specific surface areas, and lightweight designs.

Recently, 1D electrospun nanofibres of poly (3-hexthiophene) (P3HT) have been electrospun with AuNPs and demonstrated potential as non-volatile flash transistor memory devices [102]. The device exhibited excellent mechanical stability and had low operational voltages. Additionally, another very recent study electrospun aligned 1D nanofibre channels using semiconducting polymers and reported on the use of the device as a potential nonvolatile organic field effect transistor memory device [103]. In this study, a two-fluid coaxial electrospinning system was adopted using poly (9,9-dioctyl-fluorene-*co*-bithiophene) (FT82) as the core solution and poly (methyl methacrylate) (PMMA) as the shell solution demonstrating the use of polymers only to create multifunctional electronic materials [103].

In 2005, Tseng *et al.* [104, 105], reported on an electrically bistable device that could be switched electrically between two states with a conductivity difference of about 3 orders of magnitude (i.e. the switches are nonvolatile). The devices are promising candidates for digital nonvolatile memory. Their simple device came about through synthesizing polyaniline into controllable nanofibres containing AuNPs, as seen in Figure 2.10. The nanofibres have an average diameter of 30 nm, and the embedded gold particles are less than a few nanometers in diameter. Charge is stored in the metal particles provided by donor molecules within the polymer that enables the memory effect. Simple fabrication techniques such as spin on and electrode patterning make this device extremely simple and potentially low cost.

In this system, the memory effect is a result of the electric-field-induced charge transfer between polyaniline nanofibres and AuNPs such that electrons are transported from the imine nitrogen of the polyaniline to the polyaniline/gold interface. The mechanism does not require a continuous current, which makes this a stable, nonvolatile memory device with retention times demonstrated beyond several days with an on/off ratio >1,000. The retention time of the memory is determined by the charged AuNPs slowly discharging (relaxing) back into the polyaniline nanowire. The authors acknowledge that more research is required to understand this mechanism to enable optimization of the nanomaterial to minimize nanoparticle charge decay. Although advantages such as non-volatility and low cost are evident, further investigation is required into the materials' stability and temperature influence, which often plague polymer/organic-based devices [104]. Additionally the use of a conductive polymer does not propose the same economical benefits as PEO offers.

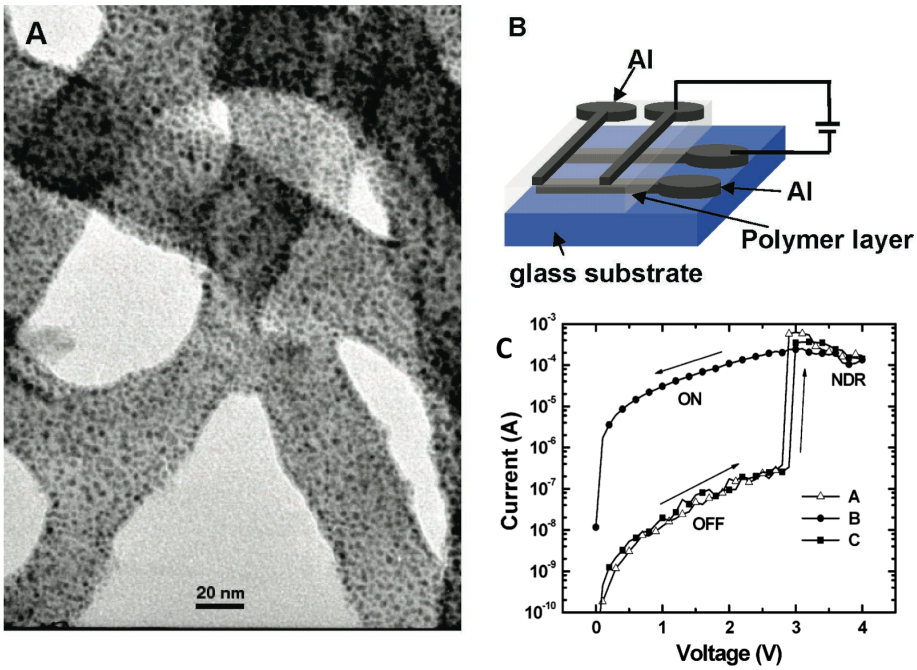

FIGURE 2.10. (A) Transmission electron microscopy image of the polyaniline nanofibre/AuNP composite. The black dots are ~1 nm gold nanoparticles contained within ~30 nm diameter polyaniline nanofibres. (B) The structure of the polyaniline nanofibre/Au NP bistable memory device. (C) Current-Voltage (I-V) characteristics of the device. The potential is scanned from (A) 0 to +4 V, (B) +4 to 0 V, and (C) 0 to +4 V. [Taken from 104]

2.4.1.1 RESISTIVE SWITCHING in MIM DEVICES – PRINCIPLE

Resistive switching is a rapidly developing field. A device that exhibits resistive switching behaviour is a device that can electrically switch between one or more resistances under the application of appropriate voltages. Devices can have two or more discrete resistance states, or may have a continuously variable resistance. Whatever the case, it is important that the change in resistance is governed by the past history of the device, i.e. by the previous voltage applied, or the previous current that has flowed through the device.

Two-terminal resistive switching devices have generated broad interest among industry and academic researchers for potential, industry-disruptive memory and logic applications. Resistive switching devices are generally composed of an insulating or resistive material (I) sandwiched between two electron conductive electrodes (M) to form a metal-insulator-metal (MIM) structure, as shown in Figure 2.11 [106, 107]. By applying an appropriate voltage, the MIM cell can be switched between a high-resistance state (HRS) and a low-resistance state (LRS). These two states can represent the logic values 1 and 0, respectively. Depending on voltage polarity, the resistive switching behavior is classified as unipolar or bipolar.

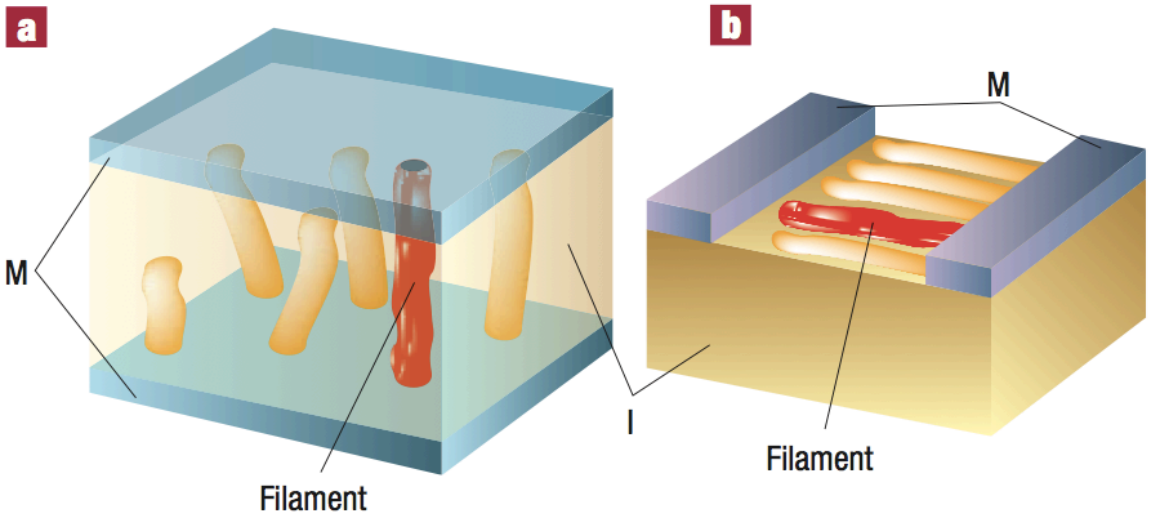

FIGURE 2.11. Sketch of filamentary conduction in MIM structures. (a) Vertical stack configuration, (b) lateral, planar configuration. The red tube indicates the filament responsible for the ON state. [Taken from 107]

2.4.1.2 TYPES OF RESISTIVE SWITCHING

During the past few years of intense research a consensus has emerged on the notion that the phenomenology of resistive switching phenomena can be roughly classified in two types, unipolar or bipolar switching. In the unipolar case, the resistive state of the system can be switched by successive application of electric stress of either the same or opposite polarities [106]. In contrast, the bipolar switching can be toggled between the resistive states by application of successive electric stress of alternate polarity. Moreover, the switching protocols used in unipolar and bipolar systems are also different, with the need of a compliance current in the former case [106].

Unipolar systems are good insulators with a large resistivity. They would normally not show any resistive switching effect. To get the systems into the switching regime it is usually required to perform an initial 'electroforming' step. In this process, a strong electric field is applied, which brings the system close to the dielectric break down. A full break down is prevented by a current limitation or compliance. After this 'SET' procedure, the resistance of the device shows a significant decrease, reaching a 'low resistance' state, R_{LO}, which is stable, i.e., non-volatile [106]. This state has an ohmic I-V characteristic at low bias. To switch the system to the 'high resistance' state, R_{HI}, a voltage has to be applied to the device, with either the same or opposite polarity than the previously applied 'forming' voltage. In this 'RESET' step, the resistance of the system suddenly increases, back to a 'high resistance' value close to the original one (as seen in Figure 2.12). No current compliance should be used in the RESET step. In fact, the resistance change occurs when the current through the device becomes larger than the value of the compliance [106]. To SET the system again in the low resistance state, a voltage with current compliance has to be once again applied, similarly to the

forming step. The system's resistance suddenly decreases down to a value close to R_{LO} at a threshold voltage V_{th}, which is smaller than the forming one. The SET and RESET switching process can be repeated many times. Regardless of the type of switching, the setting current is usually limited to avoid a hard break down of the device [106].

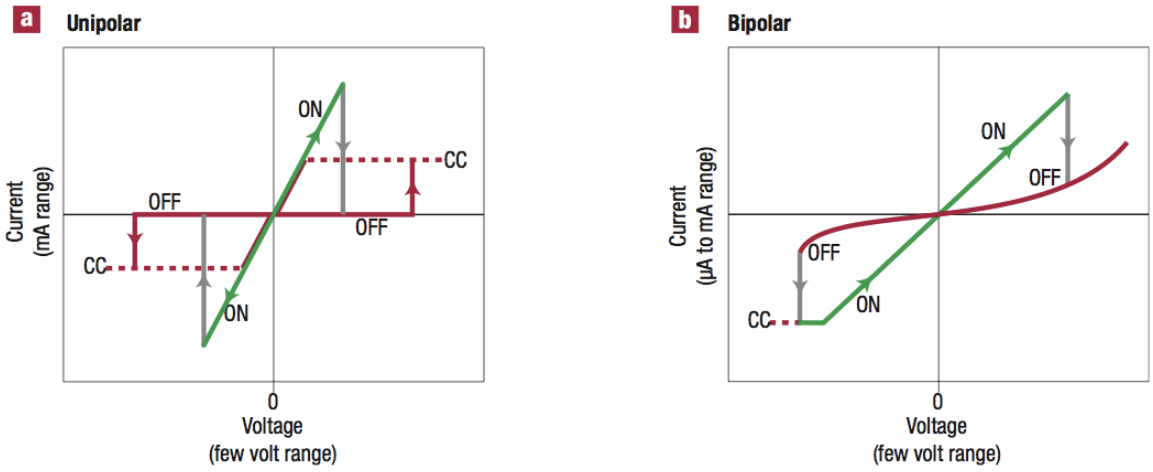

FIGURE 2.12. Typical I-V curves of ReRAM. (a) Unipolar switching whose SET and RESET voltage have the same polarity. (b) Bipolar switching whose SET and RESET voltage have opposite polarity. Compliance Current has been labeled as 'CC'. [Taken from 107]

Resistive switching phenomena and its application is a rapidly developing field. Some obstacles remain to be overcome for technological applications, such as to gain control on the reproducibility of the switching effect, and the related issues of endurance and retention time. Yet, and despite a still incomplete physical understanding of the mechanism responsible for the switching effect, the research in this field is quickly moving to the stage of applied device implementation [106].

PART B

2.5 POLYMER MICROSPHERE SYNTHESIS TECHNIQUES

Microspheres are characteristically free-flowing powders consisting of proteins or synthetic polymers which are biodegradable in nature and are generally less than 1000 μm in size. A number of different methods are available for fabrications of micro- and nano-spheres and also encapsulation of therapeutic agents in the polymeric carriers including: solvent evaporation techniques (i.e. single and double emulsion), thermal phase separation, spray drying, and more recently electrospraying. Each of the named techniques has its own unique advantages and disadvantages, depending on the polymer and the solvent used, the drug and the site of its action and also the duration of therapy [108, 109].

Although a number of different techniques in the manufacturing of polymer nanoparticles have been reported to date, the choice of the optimal fabrication method must be made according to the specific nature of the polymer, the drug and the intended therapy [109]. There exist a vast array of methods for fabricating polymer microparticles but, unfortunately, most of them are specifically designed for the assembly of a particular polymer-embedded agent pair. As a result, they lack generality. Furthermore, with the development of more sophisticated micro/nano-particles and their use in the delivery of a wider selection of drugs, the necessity of finding flexible generation techniques arises. In the search for synthesis methods that can easily adapt to changes in the embedded agents and/or polymer being used, the main features that need to be satisfied are the following:

1. The method for generating the polymer particles must allow some flexibility with respect to the properties (i.e., size, morphology, compactness of the polymer network, surface characteristics, etc.).

2. Particles must be produced as a free flowing powder and should not exhibit aggregation.

3. The generation method must be a flow process with the potential for scale up for industrial fabrication purposes.

4. The synthesis system must be easy to operate, highly repeatable, and flexible with respect to the particle formulation.

5. The embedded agent encapsulation efficiency must be high.

6. The embedded agent should be homogeneously distributed within the polymer matrix, with no preferential encapsulation sites, such as the particle core or its surface.

2.5.1 SOLVENT EVAPORATION – SINGLE AND DOUBLE EMULSION TECHNIQUES

Solvent evaporation methods are classified into single or double emulsion techniques depending on whether the drug to be encapsulated is soluble in the organic phase or not, and are also referred to as oil in water (O/W) or water in oil in water (W/O/W) emulsion methods, respectively. The single emulsion technique is adopted for loading hydrophobic drugs in carriers via oil-in-water (O/W) emulsification methods. In the first step for the preparation of the drug-loaded spheres, the polymer is dissolved in a water-immiscible solvent and

then the drug is dissolved into the polymer solution. The resulting solution is emulsified in water using an emulsifier [109]. In this technique, the amount of solvent in the emulsion is usually reduced by increasing the temperature for evaporation of the residual solvent [110, 111]. Although with this technique, the drug loaded spheres can be simply fabricated, it is only suitable for hydrophobic drugs. The encapsulation efficiencies for hydrophilic drug are very low since drug may diffuse out from the dispersed oil phase into the aqueous phase [110, 111].

Most water-soluble drugs are encapsulated by the W/O/W mechanism (i.e. double emulsion) [112]. In this technique, first, the polymer is dissolved in an organic solvent and then the aqueous solution of the drug is emulsified to form a water-in-oil (W/O) emulsion. Subsequently a W/O/W emulsion is formed by enhancing the W/O emulsion into an excess amount of water containing an emulsifier under strong stirring (Figure 2.13). Finally, the residual solvent from the solution is removed by evaporation or another extraction method. The primary advantage of this method compared to the single emulsion technique is the high encapsulation efficiency for hydrophilic drugs [112].

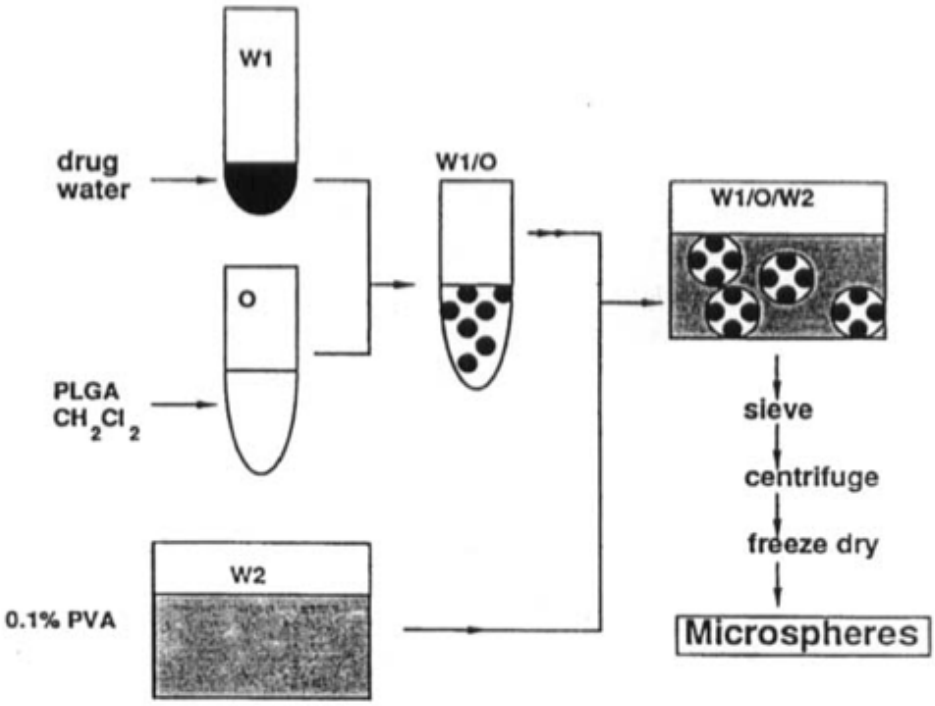

FIGURE 2.13. Schematic representation of the double emulsion solvent evaporation method. [Taken from 112]

Although emulsion methods are very popular thanks to their simplicity, their capability of covering particle sizes in the 100nm-10μm range, and their suitability for large scale production, they present numerous and important shortcomings, including: modest encapsulation efficiency, slow and batch nature of the process, difficulty to scale-up, poor control over the particle size distribution, poor repeatability and limitations with respect to encapsulation of hydrophilic agents. Particle fabrication involves the use of organic solvents to dissolve the polymer and drug, and the use of surfactants to stabilize the particles in solution. The potential toxicity of these solvents (usually alcohols, chlorocarbons or, in general, polar solvents) makes it extremely important to

effectively clean the particles after their formation, and to remove off any excess of reagents from their surface and interior.

2.5.2 THERMALLY INDUCED PHASE SEPARATION

Thermally induced phase separation (TIPS) is a supplementary fabrication method which has been used lately in polymer particle formation to produce porous microspheres for applications in wound therapy, drug delivery and also tissue engineering [113-118]. This technique requires the use of solvents such as dimethyl carbonate (DMC) with a low melting point that can be sublimed from the polymer matrix. During TIPS, the solution is separated into a polymer-rich phase and a polymer-lean phase due to crystallization of the solvent when the temperature of the polymer solution is lower than the freezing point of the solvent, shown below in Figure 2.14. The polymer is expelled from the crystallization front to form a continuous polymer-rich phase. The solvent sublimes to leave pores. This is characteristic of a TIPS particle [113, 114]. Particles are lyophilized in a freeze-dryer to leave porous structures.

TIPS is a simple, cost-effective and scalable process for the controlled manufacturing of porous microspheres although the technique must be combined with a scalable pre-processing step that enables the controlled synthesis of particles, providing consistency in size and structure. So far several studies have investigated a suitable process to manufacture these particles [113-116, 118], although they rely on batch-type processes and lack the convenience of a continuous flow process, which would enable a greater throughput for industrial processing.

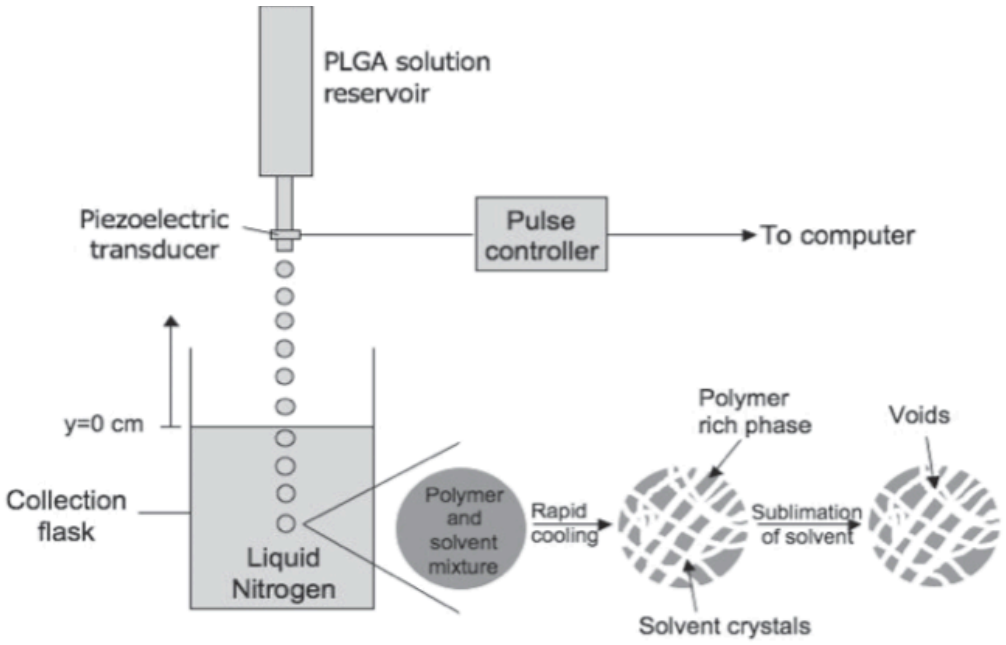

FIGURE 2.14. A schematic illustrating the principle of the TIPS process. [Taken from 118]

2.5.3 SPRAY DRYING

In this technique, dried spherical particles are produced from liquid polymer solution by rapidly drying the processing solution with a hot gas [119-121]. This method offers a number of advantages. It has improved the reproducibility of microspheres (relative to previous techniques described), and the processing conditions are relatively easy which facilitates controlling the sphere size [122]. Apart from key benefits, it also suffers from several drawbacks, firstly there is a loss of a large number of product due to adhesion to the wall of the spray drier and secondly there is a large production of aggregates as a result of the process, prior to removal of the solvent. A typical

spray drying configuration and the process can be seen in Figure 2.15.

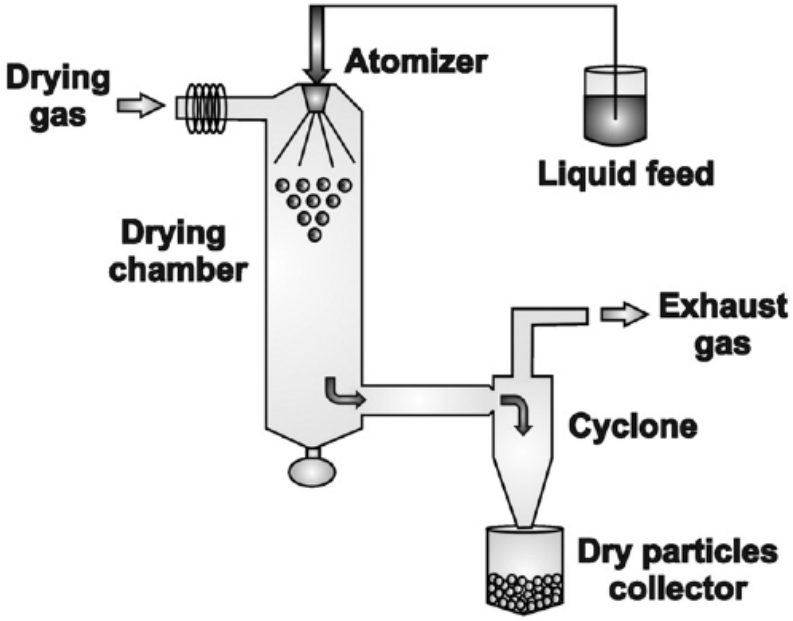

FIGURE 2.15. Schematic of a typical spray drying set up and process. [Taken from 122]

2.5.4 ELECTROSPRAYING

In the past couple of decades, electrospraying has been briefly demonstrated as a technique for manufacturing polymeric micro/nanoparticles as vehicles for drug delivery [123-130]. Efforts have been made for fabricating particles using this simple electric field driven technology and electrohydrodynamic atomization methods are gaining interest to explore ways in which the spray can be combined with a complementary step to fabricate micro/nano-particulate materials.

In brief, the electrostatic spray or electrospray is an electrohydrodynamic process in which a liquid with sufficient electrical conductivity and moderate surface tension is atomized into tiny droplets. Particles of different sizes are controlled through a combination of solution conductivity, flow rates, electric field strength, surface tension and volatility (of the solvent in the solution), which effectively has a large influence on the evaporation of the droplet to form particles. A diagram depicting this process can be seen in Figure 2.16.

The following chapters will explain in greater detail the history and operation of the technique. Additionally, the influence and control of droplet sizes is discussed and the key parameters that affect the process are examined.

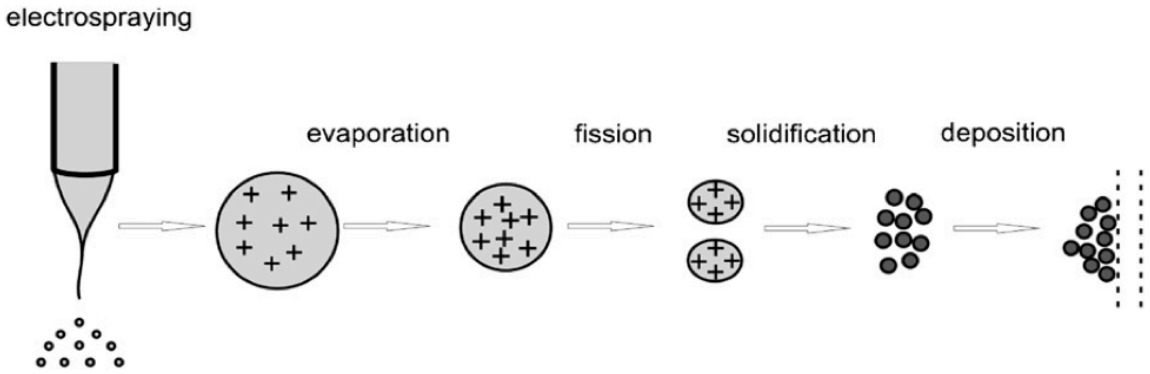

FIGURE 2.16. The steps of particle formation via electrospray atomization. [Taken from 129]

2.6 HISTORY – ELECTROSTATIC SPRAYING

The physical effects of an electrostatic field upon a liquid surface were reported many years ago. When thunderclouds develop, the electrostatic field at the Earth's surface rises by several orders of magnitude. There have been reports that waterspouts have arisen from lakes when overhead thunderclouds were present. On a more modest scale, Abbé Nollet [37], experimented with electrified liquids in the 18th century, as depicted in Figure 2.17.

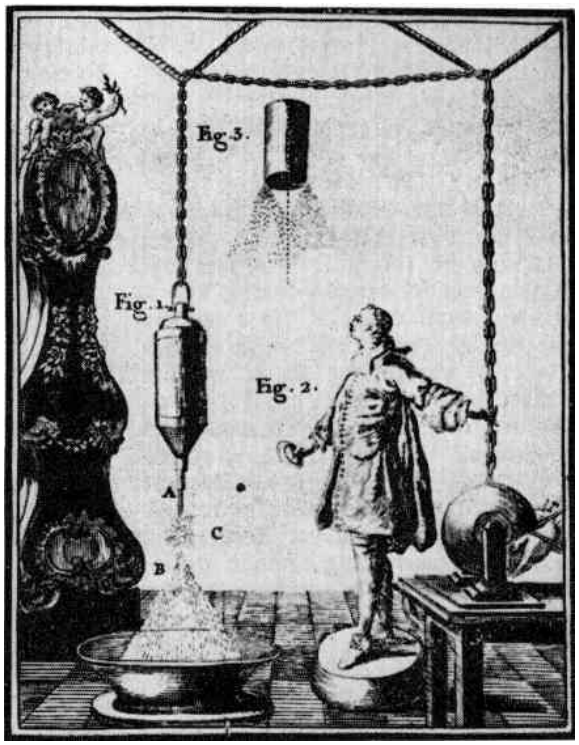

FIGURE 2.17. Experiment - Electrostatic spraying of water in the 18th century. High voltage DC is generated by the rotating glass ball and distributed to the various spraying devices by the insulated chain. [Taken from 131]

In 1750, Nollet made some advances on electrostatic sprays. He noted water flowing from a vessel would aerosolize if the vessel was electrified and placed near electrical ground. He also observed that similarly “when a person was highly electrified by connection to a high-voltage generator, would not bleed normally if he were to cut himself; blood would spray from the wound.”

The electrification of liquid droplets has matured from being an electrostatic curiosity into a highly sophisticated and useful science in its own right. Naturally occurring electrification of liquids can lead to industrial hazards, the scale of which could never have been predicted, such as the sinking of supertankers following tank-washing operations. Controlled charging of liquids, on the other hand, has led to impressive improvements in applications such as high-speed printing, crop spraying and electrified aerosols for manufacturing particles and also fibres.

2.7 ELECTROSPRAYING OPERATION

The electrostatic spray or electrospray (ES) is an electrohydrodynamic process in which a liquid with sufficient electrical conductivity and moderate surface tension is atomized into small droplets, with the dispersion of the liquid relying solely on electrostatic forces. Even though the electrosprays of conductive liquids have been extensively studied over the past few decades, not so much is known about the atomization of polymer solutions. In this section, we briefly review the basic concepts and phenomena involved in the ES process, and highlight the specifics of this technique when applied to polymer solutions.

ES has proven to be a versatile method to manufacture particles, giving tight control over size with quasi-monodisperse size distributions. It is a liquid atomization technique that relies on electrical forces induced via electric

charging of conductive media to aerosolize a liquid and generate a uniform population of highly charged, fine liquid droplets over a broad size range [132-134]. The droplets obtained by this method are charged, up to a fraction of the Rayleigh limit, which enables electrostatic forces to overcome the surface tension of the liquid surface causing the formation of a jet and its subsequent disintegration into droplets. The charge and size of the droplets can be controlled to some extent by adjusting the liquid flow rate and voltage applied to the emitter for the in-flight synthesis of particles, and control over the trajectory of these particles can be precisely manipulated by the use of electric fields to drive them to/into a grounded substrate.

By careful selection of a suitable solvent, operational parameters such as electric field strength can be optimized to overcome the surface tension of the liquid meniscus at the capillary tip elongating the droplet deformation into a conical shape, which snaps into a cone-like protrusion (also known as the Taylor Cone), from the apex of which emission begins generating a fine jet [135]. When operated in the cone-jet mode [136, 137], ES offers exquisite control of droplet size and dispersion, up to monodispersity [138]. Importantly, it does so over a phenomenal size range, from micrometer droplets to nanometer sizes, the latter being virtually impossible to generate from any other spray technique. To ensure a stable cone-jet mode, the rate of mass transfer to the emitter should be coupled with the strength of the electric field to avoid reversal and retraction of the droplet motion at the emitter tip. Furthermore, the highly unipolar-charged droplets are self-dispersing in space, as a result of their mutual Coulombic repulsion, resulting in the absence of droplet coagulation [139]. By altering the solution conductivity or liquid flow rate, it is possible to control the size of the ES-particles as the diameter monotonically increases with both variables [140].

During the droplet formation, a thin thread connects the detaching droplet with the meniscus. When the droplet moves away from the meniscus, the thread becomes thinner, eventually breaks at both ends, and disperses into few small droplets due to electric charge accumulated on it. At higher electric fields, a similar thread can be expelled from the front side of the droplet, producing an additional plume of fine droplets. In many cases, these processes are difficult to avoid, and the main droplet of required size is accompanied with a fine mist of smaller droplets. As a result, the size distribution of droplets is polydisperse; bi-modal or multi-modal. These unwanted phenomena are rarely observed in the cone-jet mode with varicose instabilities, which is of prime practical importance [139].

A conventional electrospray system (electroatomizer) is constructed from a metal-capillary nozzle (typically stainless steel), for example, a chamfered hypodermic needle, and a metal-plate counter electrode, which is a substrate holder. The nozzle is electrically connected to a high-voltage supply, while the substrate is grounded (Figure 2.18). By this means, a strong electric field is generated at the capillary outlet (between the emitter tip and collector). Liquid or polymer-based solutions are fed into the nozzle emitter at programmed constant flow rates connected via silicone or generally chemically resistant tubing. The setup is commonly confined within a Perspex enclosure to ensure the safety for the operator from electrical and chemical inhalation hazards.

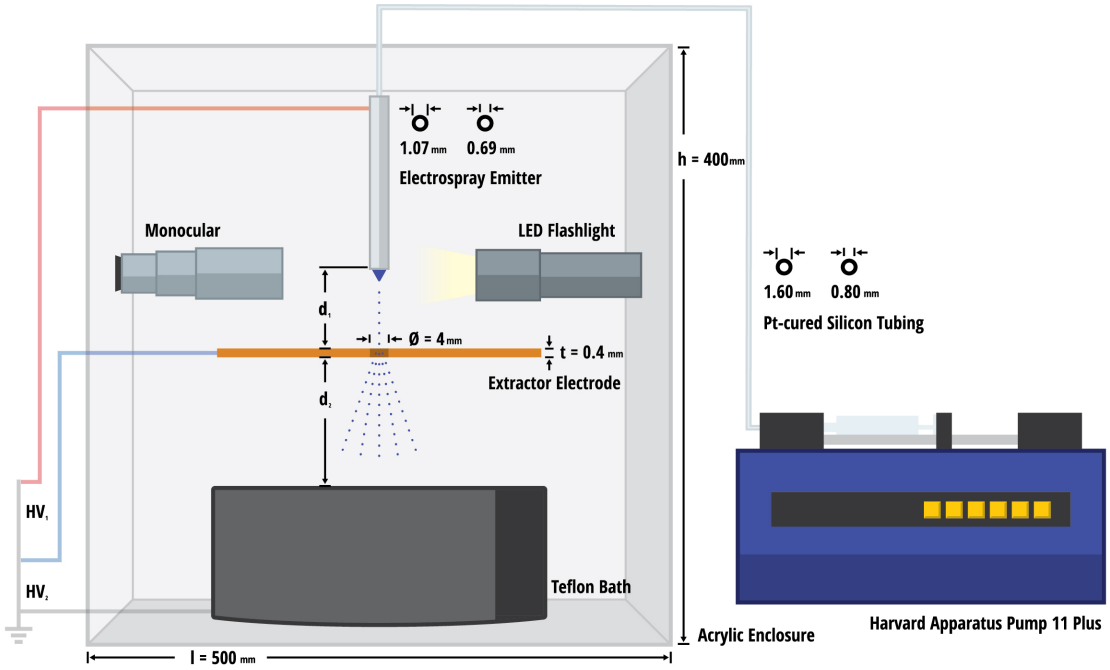

FIGURE 2.18. Schematic of a typical electrospray configuration used for the generation of tiny droplets.

2.7.1 SOLUTION PROPERTIES-DROPLET SIZE SCALING LAW

The physical properties of the liquid to be electrosprayed have a fundamental effect on the stability domain of the electrospray, as well as on its two key outcomes: the emitted current and the droplet size. Among these properties, the electrical conductivity, surface tension, viscosity and dielectric constant of the solution are the most important, and their effect over the emitted current and the droplet size are described here.

The complexity of the electrospray, with the coupling of both hydrodynamic and electrostatic phenomena and a large disparity of scales between the jet

width and the meniscus size makes it really challenging to find analytical solutions for the problem. A theoretical calculation of the electric field in the spray is complicated by the space charge field resulting from the charged droplets in the spray. As a result, there is no complete theory for the electrospray. Instead, many authors resort to valuable, semi-empirical scaling laws that relate the parameters of the problem to a selected object of study, such as the droplet and jet size, or the emitted current.

One of the most important research areas in the field of the electrospray focuses on the study of the droplet size, and how the different electrospray parameters may affect it. The scaling laws for the droplet size are inferred from those derived for the jet diameter, and are based on dimensional analysis and experimental observation. Here we focus on a scaling law that derives the droplet diameter from parameters that influence the solution properties.

There is no good agreement between different authors regarding the scaling laws for the droplet size. The most commonly used of them all (used to estimate droplet diameter in this thesis) is attributed to de la Mora and Loscertales (1994) [141], for highly conductive liquids. The authors proposed an expression that correlates the droplet diameter with the cubic root of the flow rate and the inverse of the cubic root of the electrical conductivity:

$$d \approx G(\varepsilon)\left(\frac{Q\varepsilon\varepsilon_0}{K}\right)^{\frac{1}{3}}, \qquad (1)$$

where, d is the droplet diameter, G (ε) is an empirical function of the order unity, Q is the solution flow rate, ε is the dielectric constant of the liquid, K is the electrical conductivity of the solution, and ε_0 is the permittivity of free space

[142].

As shown by Equation 1, the size of the droplets can be controlled by changing the liquid physical properties or the liquid flow rate. However, if stable operation in the cone-jet mode has to be maintained, the latter can be varied only within a certain range determined by the stability domain if droplet monodispersity has to be preserved. The key criterion for producing small droplets is therefore the use of highly conductive liquids at very small flow rates. Indeed, the smallest possible droplet diameter for a certain liquid will be obtained with the minimum flow rate at which that liquid can be electrosprayed. This minimum flow rate, Q_{min}, determines the diameter of the thinnest jet (and thus the smallest droplets) that can be achieved for a given solution. Because of this, a lot of effort has been directed to the study of this minimum flow rate regime, though the complexity of the phenomenon makes it difficult to be fully understood.

2.7.2 PROCESS PARAMETERS AND SPRAYING MODES

From the prior descriptions of electrospraying theory and operation, it is clear that the key variables that govern the technique are similar to the parameters that control the electrospinning technique although their influence is not as great as the influence of the solution properties. The processing parameters, i.e. the applied voltage, flow rate and distance effectively determines droplet diameter in the spray and influence the particle size and structure. The process parameters, which are also known as the operational conditions, are the variables that the operator has greater control over in addition to the solution properties. As the process parameters that influence the electrospray jet are the same as the parameters that influence the electrospinning jet, a restricted explanation will be given examining their influence on the technique.

The electrospray is a very complex process in which many parameters play a key role, such as the electrostatic configuration (i.e. the number of electrodes driving the trajectory of the droplets and the distance between the electrodes), the applied electric field, the feeding flow rate and more importantly the relevant solution properties. Among the latter, experiments have shown that the most important properties involved in the process are: surface tension (γ) and electrical conductivity (k). In general, for a given electrode configuration and a given liquid, there are only two operating variables that affect the ES output, e.g. the emitted current (I) and droplet size distribution (d): the liquid flow rate (Q) and the voltage applied between the electrodes (V). These two parameters have limited ranges that define a stability domain within which a stable electrospray can be stabilized [136, 143].

As Cloupeau and Prunet-Foch (1989) described in great detail, the onset of a stable electrospray takes place under the so-called cone-jet regime, in which electrostatic stresses balance surface tension forces in the liquid meniscus. The different cone-jet modes of operation (as shown in Figure 2.19) can be observed experimentally by gradually varying the voltage applied to the device capillary for a fixed solution flow rate [136, 144, 145]. The evolution of the liquid meniscus when increasing the voltage in the needle shows a sequence consisting of dripping, pulsation and cone-jet morphology. As the voltage is raised, the dripping mode is first encountered, a regime in which the hemispherical liquid meniscus drips out of the capillary at a rate that increases monotonically with the applied voltage. At a critical voltage at which the electrostatic forces start overcoming the surface tension of the liquid, instabilities appear in the meniscus, right before it drips out of the capillary. A thin jet is ejected from the tip of the meniscus when the latter reaches its maximum diameter, after which the meniscus relaxes back to its hemispherical shape. The shape of the liquid meniscus is therefore unstable, with alternation

between the spherical shape and the conical one. The process repeats itself until, upon increasing the voltage even further, a steady state is reached in which a jet is continuously emitted from the apex of the meniscus, which has now the permanent shape of a cone. This is the so-called *cone-jet mode*. The minimum voltage at which the cone jet appears is called the onset voltage. The cone-jet can be preserved over a reasonably broad voltage interval before other instabilities appear, such as lateral whipping of the jet or the appearance of the multi cone-jet mode in which several cone-jets are anchored on the nozzle in a daisy pattern. After the cone-jet is established, the regime may be preserved as the voltage is lowered a few hundred volts below the onset value before the pulsating mode sets back in [136]. The cone-jet mode is considered the most stable regime of the electrospray and is the best condition for generating the smallest and most monodisperse droplet size distributions [136, 137]. It is also the most widely studied regime of the electrospray and it will be exclusively referred to throughout the rest of the thesis.

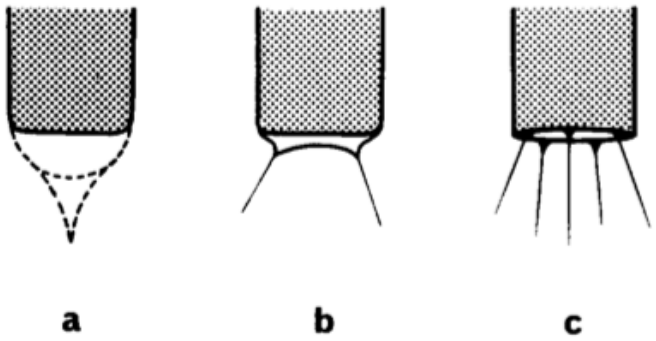

FIGURE 2.19. Variants of the electrospray cone-jet mode: (a) pulsed cone-jet, (b) and (c) variants of the multi-jet. [Taken from 145]

2.7.3 STABILITY DOMAIN

Experimental results over the years indicate that once the electrode configuration and the solution are fixed, there are two voltage bounds at each liquid flow rate between which a stable electrospray can be established [136, 143]. On the other hand, a stable electrospray can also only be attained for a finite range of liquid flow rates. These ranges of liquid flow rate and applied voltage define a stability domain in which a stable and monodisperse electrospray can be obtained. Different instabilities prevent the formation of a proper cone-jet outside these ranges.

Depending on the liquid properties, the stability domain can vary greatly. For example, Cloupeau and Prunet-Foch (1989) and Tang and Gomez (1996) found that the electrical conductivity of the liquid is the major parameter determining the boundaries of the stability domain. With the possibility of varying the electrical conductivity over seven orders of magnitude (from 10^{-7} to 1 S/m in electrosprayable liquids), a higher value of this property will shift the stability domain of the electrospray towards smaller flow rates enabling the manufacture of smaller particles [136, 143].

2.8 POROUS PLGA MICROSPHERES

Polymers, as the most versatile class of materials, have been widely adopted for application in drug delivery systems [12, 16]. They can be either degradable or non-degradable and be either natural or synthetic. Over the past two decades, the use of biodegradable and biocompatible polymers for the administration of therapeutic agents has rapidly gained attention and therefore innovative solutions for delivery have also gained momentum.

Synthetic polymers are broadly used for drug delivery and they often include esters such as poly(lactic acid) (PLA), poly(glycolic acid) (PGA) and the copolymer poly(lactic-co-glycolic acid) (PLGA). This class of polymers degrades via the hydrolytic cleavage of the ester bonds in their backbone [146]. In general, synthetic polymers have several advantages over the natural ones as their properties can be tailored and have lower level of toxicity.

PLGA is synthesized by means of random ring-opening co-polymerization of glycolic acid and lactic acid monomers. During the process of polymerization, successive monomeric units of glycolic and lactic acid are linked together in PLGA by ester linkages; therefore, yielding linear, aliphatic polyesters as products. The hydrolysis of PLGA leads to metabolite monomers, lactic acid and glycolic acid as shown below in Figure 2.20.

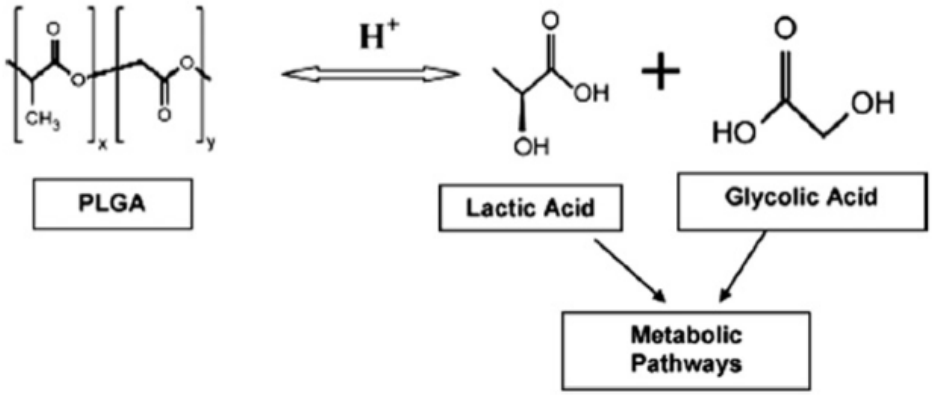

FIGURE 2.20. Hydrolysis of PLGA into lactic acid and glycolic acid. [Taken from 146]

Therapeutic carriers such as polymeric microspheres are small spherical microparticles of a size ranging from 1μm to 1000μm (Figure 2.21) that offer

functionality for application-specific industries. Therapeutic agents can be dispersed uniformly throughout the polymer matrix by dissolving the agent in the solution before processing. They have a number of interesting attributes that make them particularly suitable for microencapsulation: (i) controlled release of encapsulated materials, (ii) protection of the encapsulated materials against degradative reactions which can also result in an improved shelf life and (iii) high surface-to-volume ratios [14,15].

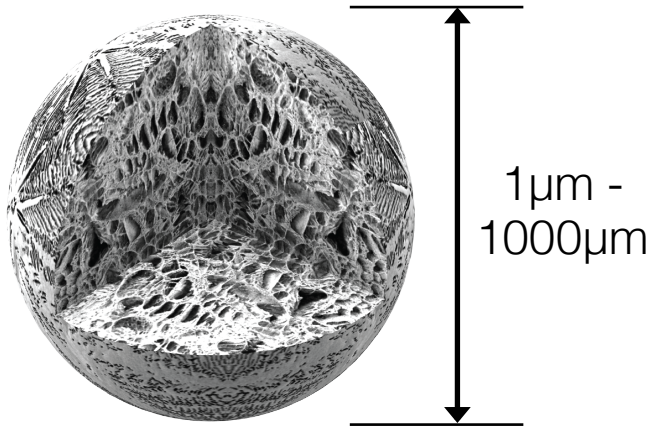

FIGURE 2.21. Cross-sectional diagram of a porous microsphere.

Many studies have reported and demonstrated their promise as effective delivery vehicles [117, 147-152], (for the controlled release of an agent) but have failed to report on the effect of size and its porosity on the release kinetics of the particle. This study aims to address this shortcoming by quantifying the porosity of particles of different sizes and assessing their release performance.

2.8.1 CONTROLLED RELEASE

Mechanisms of drug release in controlled release systems are based on a combination of diffusion and polymeric degradation processes. In these systems, biodegradable (or bioerodible) polymers are adopted for fabrication of the drug carriers. These biodegradable polymers are finally absorbed by the body due to their biocompatibility, eliminating the need for surgical removal. In bioerosion, the drug is preferably distributed uniformly throughout a polymer matrix. In this form, the drug is released as the polymer surrounding the drug is eroded as shown in Figure 2.22 (the particle appears smaller after erosion).

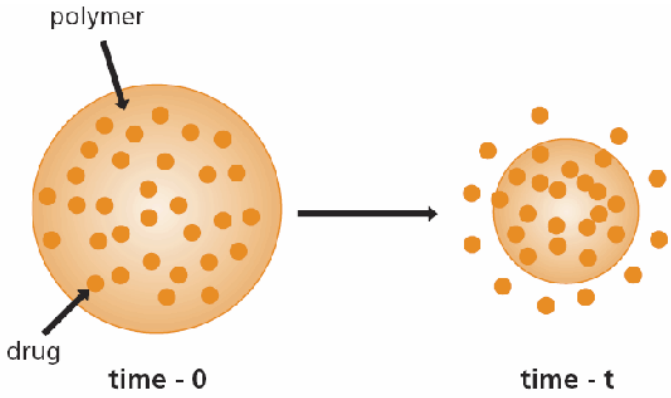

FIGURE 2.22. Schematic of a biodegradable (bioerodible) drug delivery vehicle. [Taken from 153]

There are a number of different descriptions for degradation and erosion [154]. However, the following definitions are adopted in this study: *Degradation* is based on a chemical process and exclusively refers to bond cleavage and the chain scission process during which polymer chains are sliced to form oligomers and monomers. *Erosion* is fundamentally a physical phenomenon dependent on dissolution and diffusion processes and lead physically to a loss

of material [155].

The mechanisms of polymer erosion can be divided into two types:

1. Surface erosion. When surface erosion occurs, polymers lose material from the surface; therefore, they become smaller in terms of size but keep their original geometric shape. With surface eroding polymers, the rate of erosion exceeds the rate of water permeation into the bulk of the polymer. Due to kinetics of erosion, the mechanism of surface erosion is often considered to be desirable in drug delivery systems, and hence the rate of release is highly predictable and reproducible.

2. Bulk erosion. In the case of bulk eroding polymers, erosion is not limited to the surface of the polymer. Therefore, the size of the structure may remain constant for a substantial period of time during its application. Bulk erosion occurs when the rate of water permeation into the bulk of the polymer exceeds the rate of surface erosion. As a result, polymer molecules in the bulk are hydrolyzed. The kinetics of polymer bulk erosion is more complicated than for surface eroding polymers and the majority of biodegradable polymers adopted in release of drugs undergo bulk erosion rather than surface erosion [156].

Encapsulation, biocompatibility and active agent release from microspheres are closely related to their structural properties, therefore maintaining close control over its size, shape and skeletal porosity can dictate their performance in biological microenvironments and ensure consistent reproducibility. For example, the release rates of active molecules depend on the degradation of the polymer and/or diffusion of active molecules. This can be controlled by the molecular mass of the polymer, the microsphere size and also its porosity [16-18, 157].

3. EXPERIMENTAL METHODS

PART A

This section describes the materials, methods and characterization techniques used to prepare, fabricate and synthesize the materials used throughout this project.

3.1 FABRICATION OF POLYMER NANOFIBRES

3.1.1 ELECTROSPINNING APPARATUS

Electrospun nanofabrication of polymer fibres was realized using the experimental setup sketched in Figure 3.01.

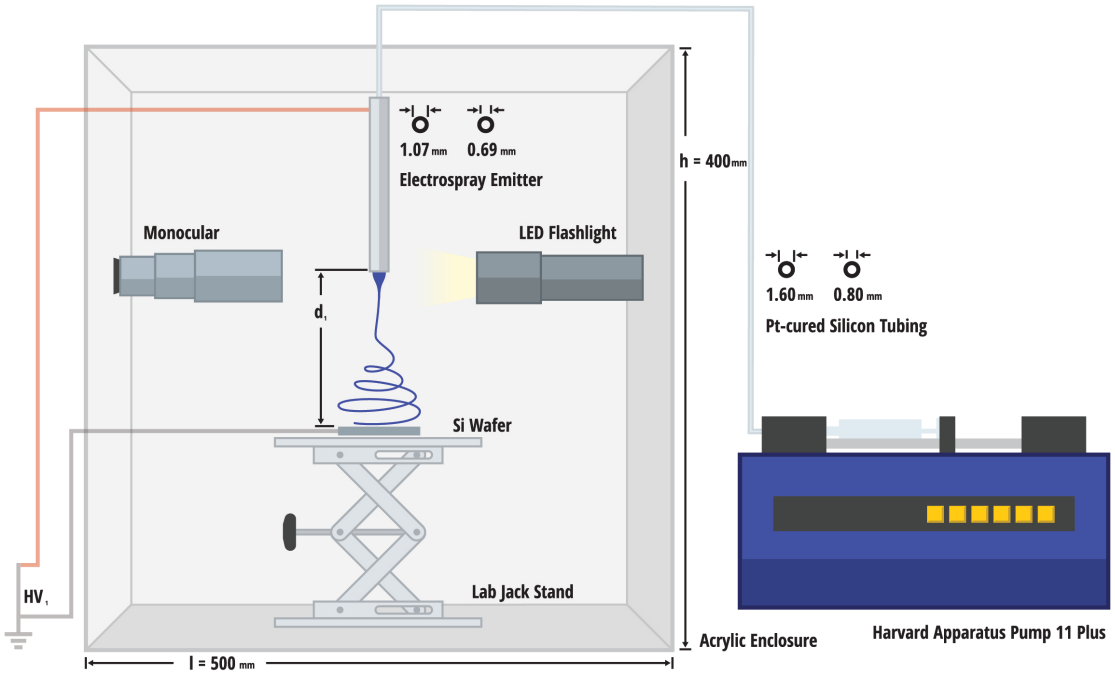

FIGURE 3.01. Schematic representation of the experimental electrospinning configuration confined within a 8mm thick Perspex enclosure and stabilized on an anti-vibration optical bench. Discharge distance d_1 was constantly held at 100mm for optimized collection onto a 1cm^2 silicon (Si) wafer. A stable cone-jet mode was preserved by monitoring the jet optically and electrically at the emitter tip.

3.1.2 MATERIALS

Poly(ethylene oxide) (PEO) (average molecular weight (Mv) 600,000Da, viscosity 4,500-8,800cP), gold(III) chloride trihydrate ($HAuCl_4 \cdot 3H_2O$) (ACS reagent, ≥49.0% Au basis) and sodium citrate was obtained from Sigma-Aldrich (Poole, UK). Deionized (DI) Water (Elga LabWater, PURELAB) was the solvent used to dissolve the polymer and to prepare the gold nanoparticles (Au

NPs). All materials were used as received.

3.1.3 CONCENTRATION

Nine polymer solutions of water-soluble PEO were prepared in DI water at the following concentrations, 1-9 wt. %. Fresh solutions were magnetically stirred continuously for 24h at room temperature, vortexed (60 seconds) and sonicated in an ultrasonic bath for 30 minutes to minimize the formation of microbubbles prior to electrospinning.

All nine solutions were electrospun in the cone-jet mode at 0.05mL/hr using a single-electrode configuration; a single 19G chamfered emitter ($Ø_{OD}$=1070µm, $Ø_{ID}$=690µm) source positioned vertically 100mm above a grounded collector plate. The electrode was maintained at a constant potential (Glassman Europe Ltd, Tadley, UK) to achieve the desired electric field with $V_{NEEDLE} > V_{COLLECTOR\ (GND)}$ and hence to ensure a stable Taylor cone was retained throughout the spinning process. A voltage of 6.5-7.2kV applied to the needle for all solutions produced electric field strengths of ~0.65-0.72kV/cm. All experiments in *Part A* and *Part B* were carried out in ambient laboratory conditions; a room temperature of 21°C and relative humidity of 45%.

3.1.4 ELECTRIC FIELD STRENGTH

Controlled distances between 60mm-150mm were chosen to vary the strength of the electric field on the fabrication process. A fresh 5% (w/w) PEO solution was prepared (using the same method reported in Section 3.1.3). Here, a single 5% (w/w) PEO solution was electrospun in the cone-jet mode at 0.05mL/hr using a single-electrode configuration; a single 19G chamfered emitter ($Ø_{OD}$=1070µm, $Ø_{ID}$=690µm) source positioned vertically above and

varied from 60mm-150mm above a grounded collector plate. Voltages of 4.9-9.5kV applied to the needle for all distances produced electric field strengths of ~0.49-0.95kV/cm.

3.2 SYNTHESIS OF GOLD NANOPARTICLES AND POLYMER/GOLD SOLUTION PREPARATION

Citrate-capped gold nanoparticles (Au NPs) were prepared using the Turkevich *et al.* method [158] to produce an as-prepared metallic Au NP solution at a concentration of 0.225mM. Briefly, a 5 mM $HAuCl_4 \cdot 3H_2O$ solution (9 mL) was dissolved in DI water (9 mL) to give a clear, pale yellow solution. The mixture was heated to boiling point and boiled for 2 minutes. 0.075 M sodium citrate solution (0.5 mL) was added dropwise over 20 seconds. The mixture was heated for a further 10 seconds and subsequently removed from the heat. A rapid colour change from clear, pale yellow to a turbid, brick red solution was observed. The solution was then left to cool to room temperature.

A 5% (w/w) PEO solution was prepared in DI water and four different concentrations of PEO loaded with passivated Au NPs subsequently mixed with the polymer, at loading concentrations of 10%, 20%, 30% and 40% (w/w). The four solutions containing gold had the following ratio of Au NP: PEO, by weight% (w/w):

1. 10:90
2. 20:80
3. 30:70
4. 40:60
5. 0:100*

*For a comparative study, a reference was also prepared, i.e. PEO without gold nanoparticles.

An IKA T-25 Digital Ultra-Turrax® homogenizer fixed with a stainless steel rotor dispersing element operated at a circumferential speed of 3000rpm was used for mixing all solutions and to ensure particles were well distributed within the polymer solution. All solutions were then mixed under continuous magnetic stirring for 24h followed by sonication (30 minutes) prior to electrospinning.

3.2.1 SPECTROSCOPIC ANALYSIS OF SOLUTIONS

3.2.1.1 NANOPARTICLE TRACKING ANALYSIS

Nanoparticle sizes were analysed using a NanoSight NS300 Nanoparticle Tracking Analysis (NTA) (Malvern, UK) system, equipped with a 532 nm laser module and a high sensitivity CMOS camera. The sample was citrate-capped gold nanoparticles suspended in Millipore water. Millipore water was used as the diluent and the sample was diluted 10,000 times. All measurements were recorded at 25 ˚C and the viscosity of water (0.9 cP) was used to calculate the particle size (hydrodynamic diameter). For accuracy and repeatability, the sample was analysed as a multiple of five runs and the results are shown as an amalgamated plot (Chapter 4).

3.2.1.2 UV-VISIBLE SPECTROSCOPY

Inorganic nanoparticles commonly aggregate in polymer solution and in order to examine whether homogenization affected particle dispersion (i.e. aggregation) and nanoparticle monodispersity, UV/Vis measurements were recorded for each sample. The presence of Au NPs in polymer solutions was

determined by spectroscopic measurements using UV-Visible Spectroscopy (Shimadzu UV-1800 Spectrophotometer). Absorption spectra were recorded over the spectral range 400-800nm (1nm resolution) using quartz cells with a 10mm path length. Detection of the Au NPs in polymer was measured by analyzing the fluorescence emission at 550nm peaks relative to a control sample of Au NPs. All stabilized PEO/Au NP blends displayed a characteristic absorption peak, which was assigned to the surface plasmon resonance (SPR) band typical of Au NPs [159].

3.3 FABRICATION OF NP/POLYMER COMPOSITES

3.3.1 SOLUTION CONDUCTIVITY

The solution conductivity was inferred by measuring the electric current passing through a column of liquid of known length and cross-sectional area connecting two opposite electrodes. Current–Voltage (I–V) measurements were performed at room temperature using a Keithley 4200–SCS (Semiconductor Characterization System) probe station and the mean resistance (R) was read out. Solution conductivities were subsequently calculated using the following formulas:

$$\rho = \frac{RA}{L} \quad , \qquad (1)$$

and,

$$\sigma = \frac{1}{\rho} \ , \qquad (2)$$

where, ρ (Ω.m) is the resistivity, R (Ω) is the resistance, A (m^2) is the cross-

sectional area of the column, *L* (m) is the length between both electrode tips and σ ($S.m^{-1}$) is the solution conductivity.

3.3.2 FABRICATION

Solutions were fed with a programmable syringe pump (Harvard Apparatus Pump 11 Plus) infused into the jetting-capillary using (Pumpsil) Pt-cured silicon tubing (Watson-Marlow). The viscoelastic solutions were electrospun in the cone-jet mode at 0.05mL/hr using a single-electrode configuration; a single 19G chamfered emitter ($Ø_{OD}$=1070µm, $Ø_{ID}$=690µm) source positioned vertically 100mm above a grounded collector plate. The electrode was maintained at a constant potential (Glassman Europe Ltd, Tadley, UK) to achieve the desired electric field with $V_{NEEDLE} > V_{COLLECTOR\ (GND)}$ and hence to ensure a stable Taylor cone was retained throughout the spinning process. A voltage of 5.5-5.9kV applied to the needle for all solutions produced electric field strengths of ~0.55-0.59kV/cm. All experiments were carried out in ambient laboratory conditions; a room temperature of 21°C and relative humidity of 45%.

The electric field driving the fibres between the emitter electrode and the collector was high enough to avoid reversal and retraction of the droplet motion near the extractor, maintaining control over the charged fibre speed and trajectory. Here, the rate of mass transfer to the emitter was coupled with the strength of the electric field to ensure a stable cone-jet mode at the apex of the liquid meniscus. The region between the emitter and equipotential grounded surface, known as the 'jetting region' was kept constant at 100mm; an optimized distance to keep the field strength sufficiently high yet prevent droplet breakup and avoid electrohydrodynamic atomization (i.e. electrospraying). Additionally, this limited viscous drag (from air) and jet drift effects and ensured a consistent fibre deposition footprint. The back-

illuminated cone-jet was monitored visually with a StereoZoom 20× microscope and electrically by measuring current emitted, and current collected. A steady emitted current ensured a stable Taylor cone was preserved throughout the spinning process.

3.4 MICROSCOPIC CHARACTERISATION

3.4.1 SCANNING ELECTRON MICROSCOPY

Polymer/gold composites and control samples were structurally characterized using SEM to examine their morphologies. Fibres were collected on 1cm^2 Si wafers (1mm thick) for 300 seconds and promptly dried in air for 24 hours to ensure solvent evaporation prior to physical characterization. Sample wafers were mounted onto aluminium stubs via adhesive carbon tabs and sputter-coated (Quorum Technologies, Q150R) with a thin layer of gold (typically a few nm) for 180 seconds in an argon atmosphere. Fibres were imaged under SEM (JEOL JSM-7401F) equipped with a Gatan digital camera at an accelerating voltage of 1.0 kV and working distance of 5mm. Micrographs were captured at several magnifications.

3.4.2 TRANSMISSION ELECTRON MICROSCOPY

For visual characterization of Au NPs, a 5µl aliquot of nanoparticle suspension was placed on a plain carbon-coated copper TEM grid and allowed to evaporate in air at room temperature for 180 minutes. Fibres were collected on plain holey carbon-coated copper TEM grids (Agar Scientific) for 30 seconds, and promptly dried in air for 24 hours to ensure solvent evaporation prior to physical characterization. Bright field TEM images were obtained using a JEOL-1010 microscope at 80 kV equipped with a Gatan digital camera.

3.4.3 SCANNING TRANSMISSION ELECTRON MICROSCOPY

All STEM images were acquired using a FEI Titan TEM in (Scanning-TEM) STEM mode, where a ~0.3 nm probe was raster-scanned over a sample region, forming an image with electrons that were forward-scattered to high angles (>50 mrad). The intensity of the images is inversely proportional to the local atomic number of the sample material, so Au NPs show bright contrast and the polymer appears dark. Images were acquired using an acceleration voltage of 80 kV to minimize beam damage.

3.5 FABRICATION OF ELECTRICAL NANODEVICES

3.5.1 NANODEVICES – RESISTIVE SWITCHING

The device here has a simple structure consisting of the electrospun polymer film sandwiched between two electrodes. A top and bottom Aluminium (Al), Chromium (Cr) or Platinum (Pt) electrode with a thickness of ≈150nm was deposited by thermal evaporation in a chamber under a pressure of $1x10^{-6}$ Torr. The active layer was formed by electrospinning linear composite PEO/AuNP nanofibres onto the Cr/Al/Pt-coated SiO_2/Si substrates, to create a sandwich-like structure (Figure 3.02). Both the top and bottom electrodes have a width of 0.5mm, and the device covers an area of $0.25mm^2$. All following I-V measurements were performed at room temperature using the Keithley-4200 Semiconductor Characterization System (SCS).

3.6 ELECTRICAL CHARACTERISATION

3.6.1 ELECTRICAL PROBE STATION

Electrospun composite nanodevice (current-voltage) I-V measurements were performed at room temperature using a Keithley 4200-SCS probe station. Connection to the sample was made using two 1.25" Signatone tungsten contact probes (SE-10T) and the current was measured by applying varying voltages up to +/- 30V. Compliance current was set to 100mA.

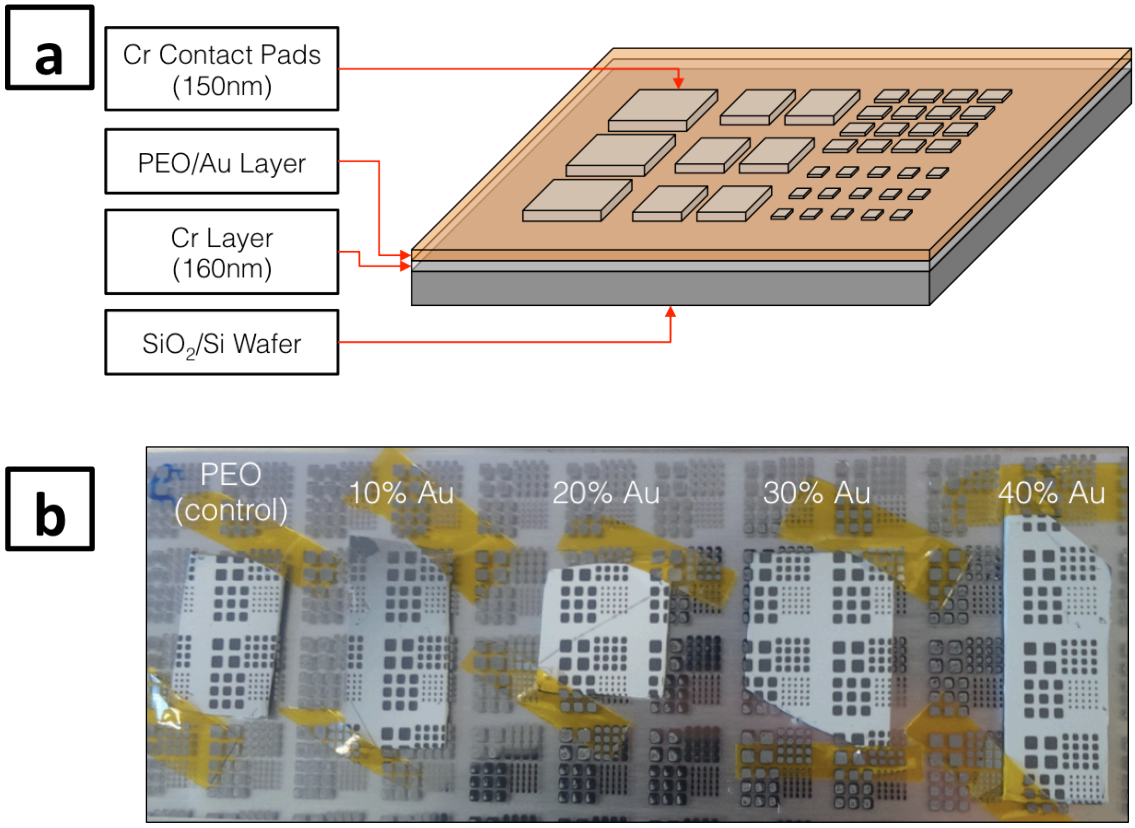

FIGURE 3.02. (a) Schematic configuration of the electrospun PEO/Au device structure for electrical measurements. The contact pad material was altered with Al, Cr or Pt material. (b) Photo of the nanodevices.

PART B

3.7 SYNTHESIS OF PLGA TIPS MICROSPHERES

3.7.1 ELECTROSPRAYING APPARATUS

Electrospray synthesis of polymeric particles was realized using the experimental setup sketched in Figure 3.03.

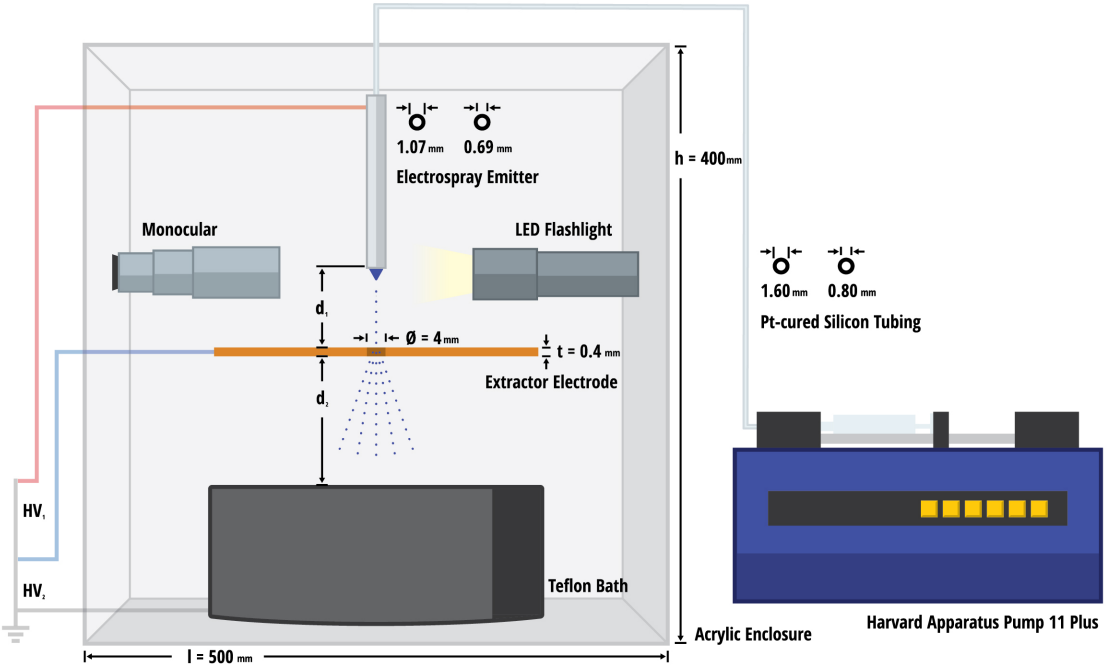

FIGURE 3.03. Schematic representation of the experimental ES configuration confined within a 8mm thick Perspex enclosure used for this study. Distances, d_1 and d_2 were constantly held at 1mm and 40mm, respectively, for optimized collection into the Teflon cryogenic vessel. Distances remained constant throughout the investigation.

3.7.2 MATERIALS

Acid terminated PLGA (Purasorb PDLG 5004A, 50:50 DL-lactide/glycolide copolymer) was obtained from Corbion Purac (Netherlands). Dimethyl carbonate (DMC) (Reagent Plus 99%), Formic acid (Reagent grade ≥95%) and Rhodamine 6G (Dye content 99%) were all purchased from Sigma-Aldrich (Poole, UK). Rhodamine 6G (R6G) was used as a drug surrogate to monitor release. Liquid Nitrogen (LN_2) was purchased from the British Oxygen Company (BOC) (London, UK). All materials were used as received.

3.7.3 SYNTHESIS

A 5% (w/v) polymer solution of PLGA (Purasorb PDLG 5004A, 50:50 DL-lactide/glycolide copolymer) was prepared using a solvent formulation of dimethyl carbonate (DMC), formic acid and deionized (DI) water with the following ratio, 99:0.5:0.5 (v/v), respectively. Due to its low conductivity, DMC was not electrosprayed in the cone-jet mode. To enable its stability in this spray regime, traces of formic acid and DI water were added to the bulk DMC formulation. Fresh solutions were magnetically stirred continuously for 120 minutes at room temperature, vortexed and sonicated in an ultrasonic bath for 30 minutes to minimize the formation of microbubbles prior to electrospraying. Solutions were fed using a programmable syringe pump (Harvard Apparatus Pump 11 Plus) connected to the ES apparatus using (Pumpsil) Pt-cured silicon tubing. The solution was electrosprayed in the cone-jet mode (shown in Figure 3.04) at 1mL/hr using a dual-electrode configuration (i.e. needle and extractor plate) with one 19G ($Ø_{OD}$=1070μm, $Ø_{ID}$=690μm) stainless steel ES emitter (vertically) positioned concentrically 1mm above a 4mm diameter extractor hole opening.

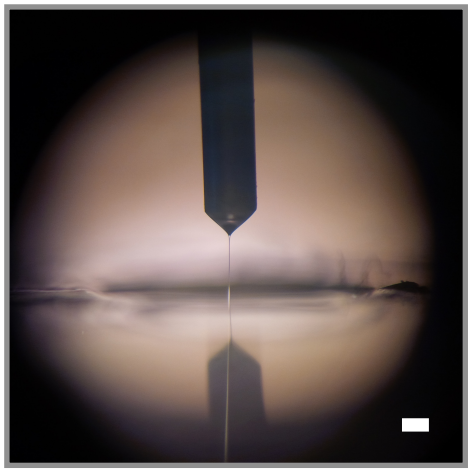

FIGURE 3.04. Photo of electrospraying in the cone-jet mode. Scale bar: 500μm.

Care was taken to avoid misalignment between the nozzle and the extractor hole, which may cause the jet to discharge asymmetrically leading to an electrical short between the two components. The region between the emitter and extractor plate is known as the 'jet-forming region' and the distance between the extractor and LN_2 collector is known as the 'spray region'. The spray region was kept constant at 40mm, an optimized distance to keep the field strength sufficiently high yet prevent droplet freezing at the capillary exit ensuring the nozzle temperature remained above the Leidenfrost temperature. Additionally, this particle transport distance held above the nitrogen vapour layer limited air viscous drag, spray drift and space charge effects.

The electrodes were maintained at different potentials to achieve the desired electric field with $V_{NEEDLE} > V_{EXTRACTOR} > V_{COLLECTOR\ (GND)}$. The voltages applied (using a Glassman High Voltage Power Supply, Glassman Europe Ltd, UK) to the needle and extractor were 10.2kV and 7.0kV, respectively, producing

electric field strengths of 102.0 kV/cm (between emitter and extractor) and 1.75 kV/cm (between extractor and LN_2 free surface). The electric field driving the droplets between the extractor electrode and the collector was high enough to avoid reversal of the droplet motion near the extractor, maintaining control over the charged droplet speed and trajectory. The back-illuminated spray was monitored visually with a StereoZoom 20x microscope and electrically by measuring current emitted, fly-back (at the extractor electrode) and current collected. Particles were collected in a liquid nitrogen bath (40mm below the extractor plate) held within a non-stick Teflon casing to rapidly induce the phase separation. ES-emission was performed for 60 minutes and collected particles were promptly transferred to a freezer (-80°C) and subsequently lyophilized for 24 hours in a freeze dryer (LTE Scientific Ltd, Oldham, UK), as shown in Figure 3.05. Post-lyophilisation, particles were stored in their containers for characterization.

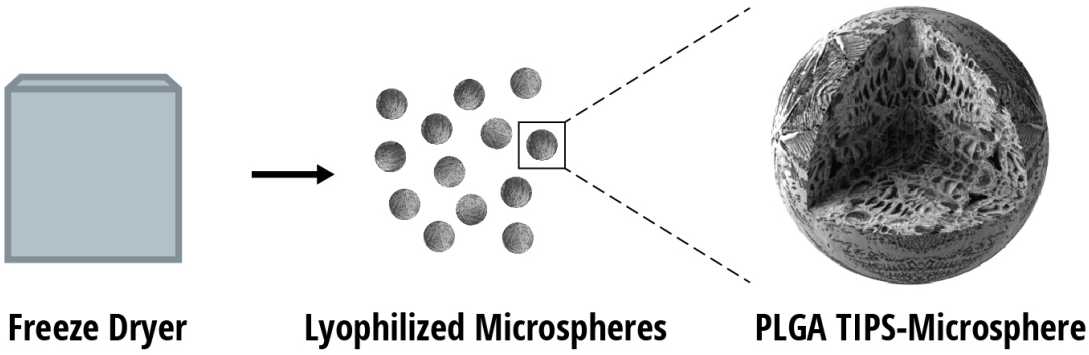

FIGURE 3.05. Post-lyophilisation of the electrosprayed PLGA particles.

A scaling law was applied prior to solution preparation describing the dependency of the diameter of electrosprayed droplets on the physical properties of the liquid being atomized. Regardless of the scaling law

considered, the solution electrical conductivity (*K*) and flow rate (*Q*) at which the liquid are fed are the primary parameters that control the overall size of ES particles. Droplet sizes were estimated using:

$$d \approx G(\varepsilon)\left(\frac{Q\varepsilon\varepsilon_0}{K}\right)^{\frac{1}{3}}, \qquad (3)$$

where *d* is the droplet diameter, *G* (ε) is an empirical function of the order unity, $G(\varepsilon) = -10.87\varepsilon^{-6/5} + 4.08\varepsilon^{-1/3}$, *Q* is the solution flow rate, ε is the dielectric constant of the liquid, *K* is the electrical conductivity of the solution, and ε_0 is the permittivity of free space [142]. If a stable cone-jet is preserved, flow rates can only be varied within a certain range defining the ES stability regime. In this case, electrical conductivity was sufficiently raised by adding trace amounts of formic acid and DI water to subsequently decrease droplet diameters. Liquid flow rates were adjusted to 1 mL/hr, 2 mL/hr, 5 mL/hr, 10 mL/hr, 20 mL/hr and 30 mL/hr to manufacture particles of six different sizes.

3.8 CHARACTERISATION

3.8.1 SOLUTION CONDUCTIVITY

The solution conductivity was inferred using the same methodology reported in Section 3.3.1. Here, conductivities were used to estimate droplet diameters using Equation 3 for particles synthesized at 1 mL/hr as demonstration of the smallest TIPS microsphere that could be manufactured within the ES stability regime.

3.8.2 SCANNING ELECTRON MICROSCOPY

TIPS microsphere populations were structurally characterized via SEM to examine their exterior morphologies. Samples were mounted onto aluminium stubs via adhesive carbon tabs and sputter-coated (Quorum Technologies, Q150R) with a thin layer of gold (Au) (typically a few nm) for 180 seconds in an argon atmosphere. Particles were imaged under a scanning electron microscope (JEOL JSM-7401F) equipped with a Gatan digital camera at an accelerating voltage of 1.0kV and working distance of 5mm. Micrographs were captured at several magnifications.

3.8.3 FOCUSED ION BEAM

Internal morphologies of small (~10–20μm) and large (~200–250μm) TIPS microspheres were analyzed by SEM after cutting with an FIB (Carl Zeiss XB1540 CrossBeam FIB). Particles were loaded onto specimen holders and prepared using the same techniques as described for SEM analysis. In situ three-dimensional cuts of rectangular cross-section were performed over deposits of particles using a finely focused beam of gallium (Ga^+) ions. Low beam currents selected for milling were typically in the range of 500pA to 1nA between subsequent shots of milling process to ensure minimal damage to the polymer matrix. After the initial milling, polishing was carried out at a lower beam current (typically 100pA) in order to minimize the surface roughness induced by the initial higher current milling. Particle cross-sections were captured after milling using gallium-free imaging by a thermal field emission scanning electron microscope (FE-SEM), integrated into the FIB system.

3.8.4 MORPHOLOGI G3SE – SIZE AND SHAPE ANALYSIS

Particle size and shape analysis were evaluated using the Morphologi® G3SE system (Malvern Instruments, Malvern, UK); a microscopic image analysis-based particle characterization system. Samples prepared at two different flow rates, 1 mL/hr and 15 mL/hr were loaded into an aluminium sample entrainment spool (SES) (sprayed with anti-static spray), dry-dispersed using the instruments sample dispersion unit (SDU) and then prepared according to a standard operating procedure (SOP). A gas injection pressure of 1 bar (at 0.05 bar increments) was applied to the SES to cause turbulent flow within the chamber and even mixing of the particles. $19mm^3$ of sample was dispersed (homogenously distributed without particle-particle collision) with a sample settling time of 180 seconds and imaged through a 20×-magnification objective (Nikon CFI 60 brightfield/darkfield). Five scan areas were distributed across the dispersion area and the results combined comparing both small (prepared at 1 mL/hr) and larger (prepared at 15 mL/hr) ES TIPS microspheres. Two key particle size and shape factors were reported: (i) Circular Equivalent Diameter (CED); the diameter of a circle with the same area as the projected area of the particle image and, (ii) High Sensitivity Circularity (HSC); a measure of the closeness of a particle shape to that of a perfect circle: a value of 1 represents a perfect circle and an irregular shape will have a value less than 1.

3.8.5 CONFOCAL RAMAN MICROSCOPY

Prior to analysis, samples were mounted on stainless steel specimen stubs (Agar Scientific, UK). Raman spectra acquisition and mapping images were obtained using a WiTec Alpha 300R (LOT Oriel, UK) operating a 0.3 W single frequency 785 nm solid state diode laser (Toptica, USA), a 20× objective lens

and an Acton SP2300 triple grating monochromator/spectrograph (Princeton Instruments, USA). Spectra were recorded over the wavenumber range 0–3,200cm^{-1} at a mean resolution of 3cm^{-1}. Images were created by mapping the intensity of the peak with centre wavenumber 1,763 cm^{-1} over a 175 x 175 pixel grid, covering an area of 175µm x 175µm. Images were also recorded in vertical stacks of horizontal slices, at 12.5µm height intervals.

3.8.6 MERCURY INTRUSION POROSIMETRY

To determine the porosity/void fraction of small (~10–20µm), medium (~100–150µm) and large (~200–250µm) particles, microsphere samples were each weighed and added to a glass penetrometer suitable for powder samples. The penetrometer was sealed and the sample analysed using an AutoPore IV 9500 mercury (Hg) porosimeter (Micromeritics, UK) at pressures in the range 3 kPa - 207 MPa. Hg intrusion into the sample was analysed using the Washburn equation in order to determine the pore diameter distribution and data was recorded on in-built AutoPore software;

$$D = -\frac{4\gamma}{P}\cos\theta\,, \qquad (4)$$

where D is pore diameter, γ is the surface tension of Hg at 20°C, which is assumed to be 0.485 N/m, P is the applied pressure, and θ is the contact angle between the Hg and the porous solid, which is assumed to be 130° [160].

3.8.7 THERMOGRAVIMETRY

Thermogravimetric analysis (TGA) was performed on ES-PLGA TIPS microspheres and PLGA granules (as-received) from Corbion Purac (Netherlands) using a NETZSCH STA 449C TGA system. The instrument's thermobalance and ceramic crucible were calibrated prior to measurement in a vacuum-tight furnace chamber. Data were recorded from 25 to 45°C with a constant heating rate of 1°C minute^{-1} in a nitrogen atmosphere at 0.5 bar. Measurements were averaged for triplicate readings and the mean thermograms displayed.

3.9 SYNTHESIS OF DYE-LOADED PLGA MICROSPHERES

3.9.1 SYNTHESIS

R6G-loaded PLGA microspheres were synthesized following the same method reported earlier (with non-dye-loaded PLGA microspheres). Briefly, a single mixture of 5% (w/v) polymer solution of PLGA (using the original solvent formulation) loaded with R6G dye at 10ppm was prepared. The dye was dissolved following continuous stirring for 120 minutes at room temperature and 30 minutes sonication to form a dye-PLGA blend. Using the same ES-configuration as seen in Figure 3.03, the solution was electrosprayed in the cone-jet mode at 1 mL/hr, 15 mL/hr and 30 mL/hr each for 30 minutes into a glass beaker (externally wrapped in aluminium foil) containing LN_2 surrounded by a cryogenic vessel also topped with LN_2. The vessel minimized LN_2 evaporation and balanced the heat capacity between beaker and vessel; both were electrically grounded components. A voltage drop ranging from 2.8-3.4kV between the emitter and extractor (charged at 8.0kV) generated sufficiently high electric fields to produce a stable cone-jet mode for the three flow rates. A

second field between extractor electrode and LN_2 free surface held at 2.0 kV/cm facilitated the acceleration and trajectory of particles into the cryogenic medium held on an equipotential surface. Particles were collected for 30 minutes and promptly transferred to a freezer (-80°C) and subsequently lyophilized for 24 hours in a freeze dryer.

NB: Only a small concentration of active agent was purposefully chosen to avoid significant changes to the conductivity of the PLGA solution. The choice of active agent loading is not a limitation of the ES-based synthesis protocol.

3.9.2 ENCAPSULATION EFFICIENCY

Freeze-dried R6G-loaded PLGA TIPS microspheres for small (~10–20μm), medium (~100–150μm) and large (~200–250μm) particles with known dye loading concentrations (10ppm) and masses were immersed and re-dissolved back into the ES solvent formulation of DMC, formic acid and DI water with the following ratio, 99:0.5:05 (v/v) to each produce a 1% (w/v) concentration solution for each sample. All three samples were first agitated and magnetically stirred continuously for 360 minutes at ambient temperature under sealed conditions to release the total content of R6G dye entrapped within the polymer matrix. Following centrifugation, supernatants were collected, filtered (Millipore, pore size 0.45μm) and the total R6G content determined by UV-Visible Spectroscopy (Shimadzu UV-1800 Spectrophotometer). Absorption spectra were recorded over the spectral range 300-800nm (1nm resolution) using quartz cells with a 10mm path length. R6G peaks were detected at 515nm for each sample. The encapsulation efficiencies (EE) were calculated according to the following equation:

$$EE(\%) = \frac{Total\ amount\ of\ dye\ in\ PLGA\ microspheres}{Total\ amount\ of\ dye\ loading} \times 100, \qquad (5)$$

where, the total amount of dye in the microspheres is the amount of dye encapsulated in/on the polymer and the theoretical dye content is the amount of dye added to the polymer solution for ES-synthesis. The dye contents were then calculated by reference to a standard calibration curve, formed from 6 different concentrations (0.5ppm – 150ppm) in the same solvent. The calibration curve was found to be highly linear and reproducible, with a coefficient of determination (R^2) of ≥0.98. All measurements were performed in triplicate and averaged.

3.9.3 *IN VITRO* RELEASE STUDY

Dissolution studies were performed by dispersing dry TIPS microspheres (at known quantities) in distilled water. R6G-loaded PLGA particulates were prepared at 1% (w/v) concentrations for each release sample and magnetically stirred at 37°C for 7 days. At predefined time intervals, aliquots of 2mL of the dissolution medium were withdrawn, centrifuged and filtered (Millipore, pore size 0.45μm). After spectroscopic measurement, the same volume of dissolution medium withdrawn was returned to the same sample flask (i.e. not replaced with fresh medium). Detection of the released dye was measured by analyzing the fluorescence emission at 515nm peaks and the amount of R6G released was determined by interpolation from a standard calibration curve. In vitro release spectra were recorded in triplicate and data shown is the mean of the results. Error bars are indicated on cumulative release curves and relative standard deviation (RSD) for the three measurements remained consistently ≤5%.

4. RESULTS

ELECTROSPUN FABRICATION OF COMPOSITES

4.1 OPTIMISATION – PEO CONCENTRATION

As part of the solution optimisation, I carried out a systematic investigation to study the effects of material and processing parameters for electrospinning PEO fibres. Primary experiments before the fabrication of electrospun 1D nanofibre composites (containing metallic Au NPs) involved optimising the polymer concentration and the distance between the needle orifice and the grounded collector screen. Nine polymer concentrations were electrospun and examined under SEM analysis (Figure 4.01).

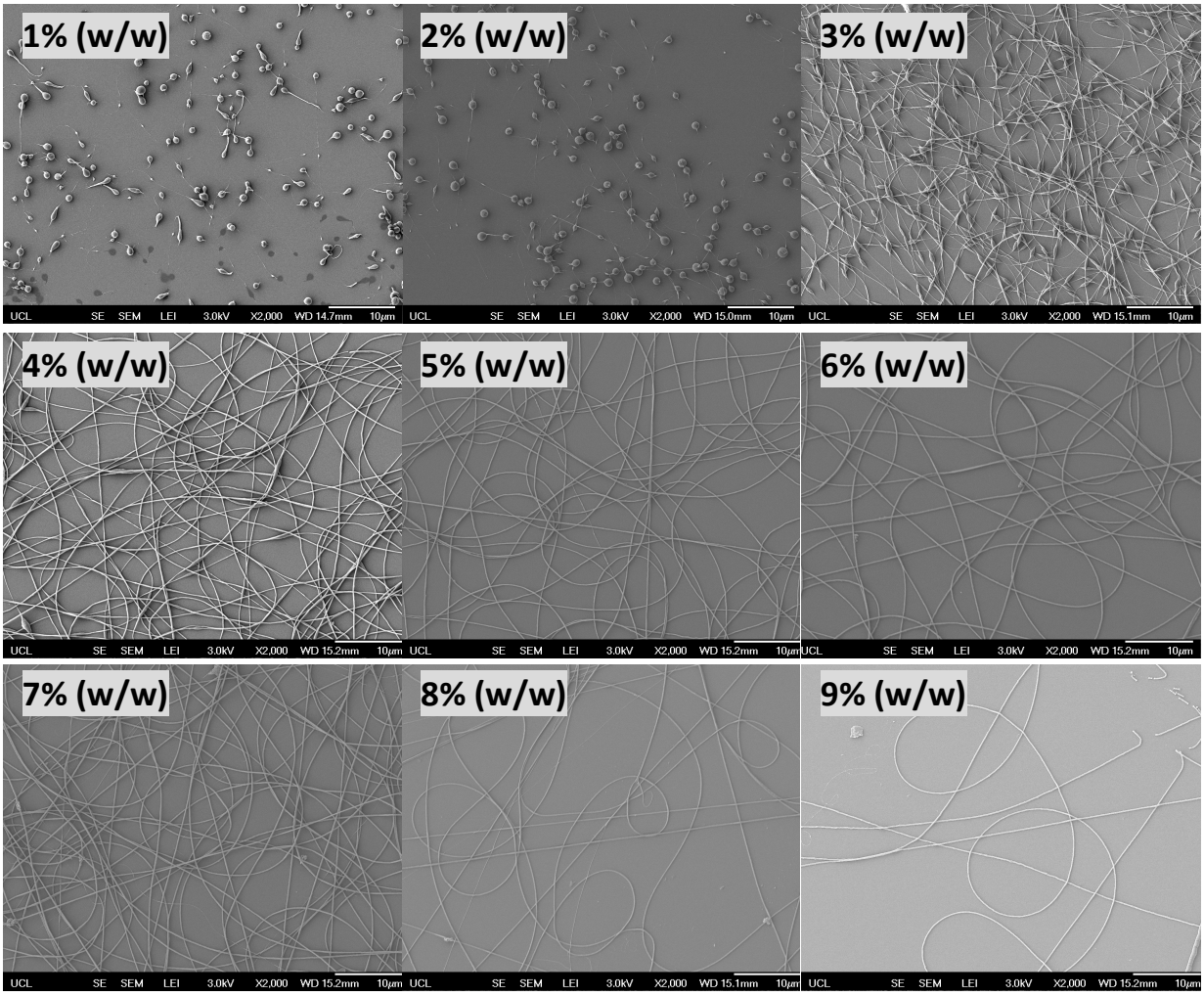

FIGURE 4.01. SEM images of the nine electrospun concentrations (concentration labeled in micrograph).

In this optimisation study, uniform PEO fibres of varying thickness were produced, with diameters ranging from 30nm – 195nm across the concentration range of 1-9% (w/w). It is important to note that the smallest average diameter measured here does not include the presence of beads.

Images recorded with fibres containing bead/spindle-like structures were not investigated any further due to their non-uniform morphology. A general trend was observed with increases in concentration; the surface morphologies changed continuously from a spherical shape to a fibrous one; spheres were observed at 1% and 2%, spindle-shaped particles within fibres at 3% and 4% and fibres with uniform diameters between 5% - 9%. At lower viscosities, it is more likely to spray droplets rather than fibres due to insufficient polymer chain entanglements, which would explain the particle-like structures seen at 1% and 2%. At higher concentrations (and hence viscosities), the increased stretching of the polymer jet allows the droplet exiting the orifice to undergo elongation and consequently fibre production.

Visually from Figure 4.01, the thinnest fibre whilst retaining uniform diameter and morphology was found at 5% (w/w) concentration. The mean diameter for 5% was 153.98±2nm (≈154nm). Concentrations below this produced beaded fibres and particles. Concentrations above 5% manufactured smooth fibres although at greater thickness, graphically seen in Figure 4.02. For this reason, PEO at 5% (w/w) was selected for all the follow on studies.

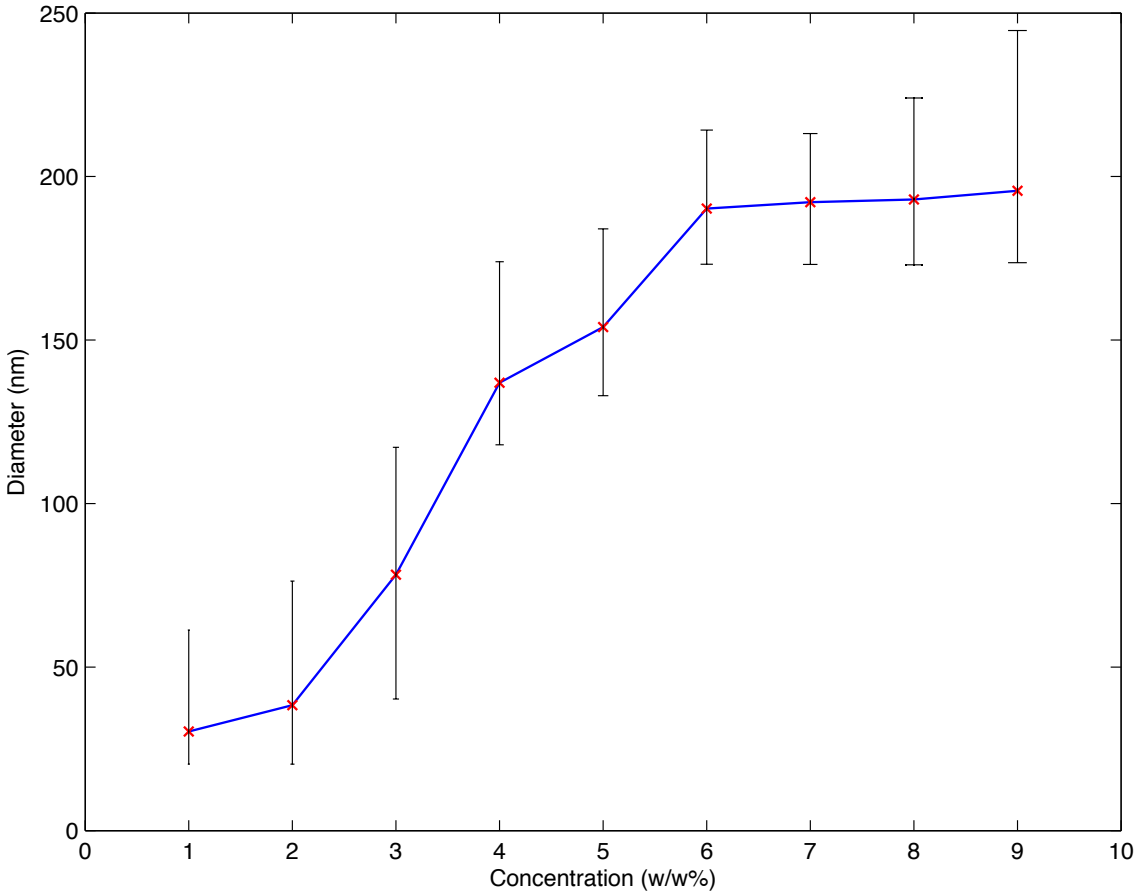

FIGURE 4.02. The effect of PEO concentration on the diameter of electrospun fibres.

Figure 4.03 represents the diameter distribution of 5% (w/w) for 100 fibres analysed after SEM analysis. Data was gathered using ImageJ analysis instrument tool. The smaller and larger diameters recorded below and above the mean diameter of 154nm were most likely due to greater stretching forces applied to the jet during the electrospinning process and also due to the non-linear and unpredictable behaviours occurring during solvent evaporation

processes. Greater solvent evaporation effects during the process as a result of minor changes in temperature and humidity may lead to slight alterations to the fibre in the jetting region.

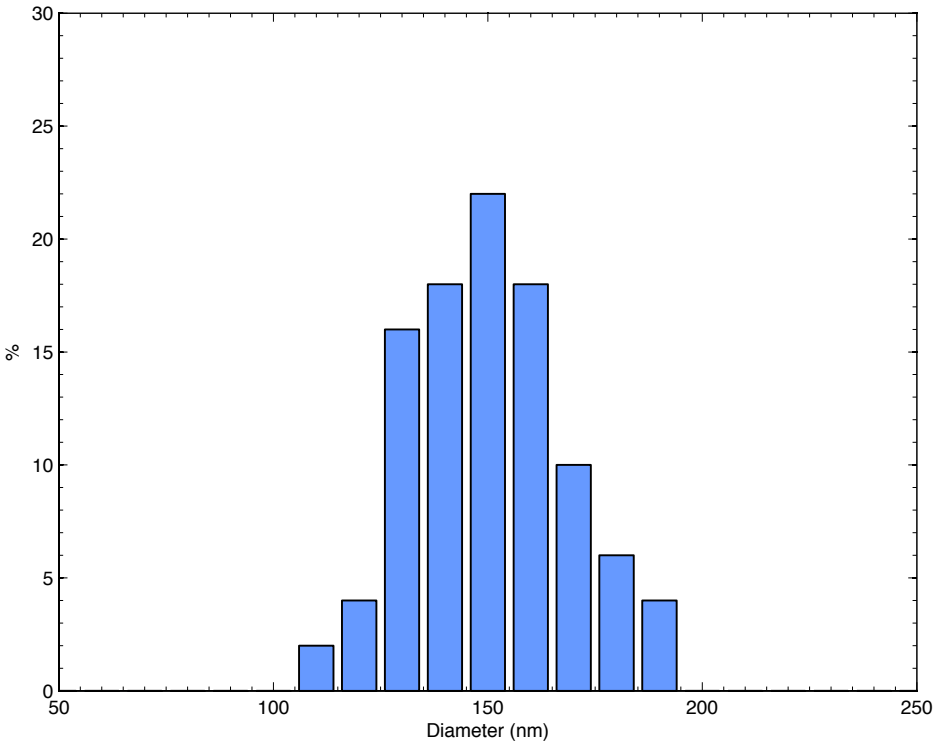

FIGURE 4.03. Histogram showing the frequency distribution of fibre thicknesses recorded at 5% (w/w) PEO concentration.

4.2 OPTIMISATION – DISTANCE

To investigate the effect of distance between tip and collector on the diameters of fibres, a 5% (w/w) PEO polymer solution was prepared. Ten distances were chosen, ranging between 6-15cm. Samples were also analysed under SEM.

With an increase in distance, it can be seen from the SEM images recorded in Figure 4.04 that fibres get thinner as distances are increased (Figure 4.05) due to the longer time of flight between the tip and collector, which allows further stretching of the polymer and greater solvent evaporation. Subsequently this results in a thinner fibre. At 6cm and 7cm, droplets and spindle-like fibres were deposited, respectively, as the distance between the needle and the grounded collector is insufficient for spinning fibres. In this experiment, the optimal distance was found at 10cm, producing the thinnest fibre whilst also retaining a uniform morphology. The mean diameter measured at 10cm is 144.43±2nm (≈144nm), and therefore the following experiments involving the incorporation of nanoparticles were electrospun at 10cm using a PEO polymer concentration of 5% (w/w).

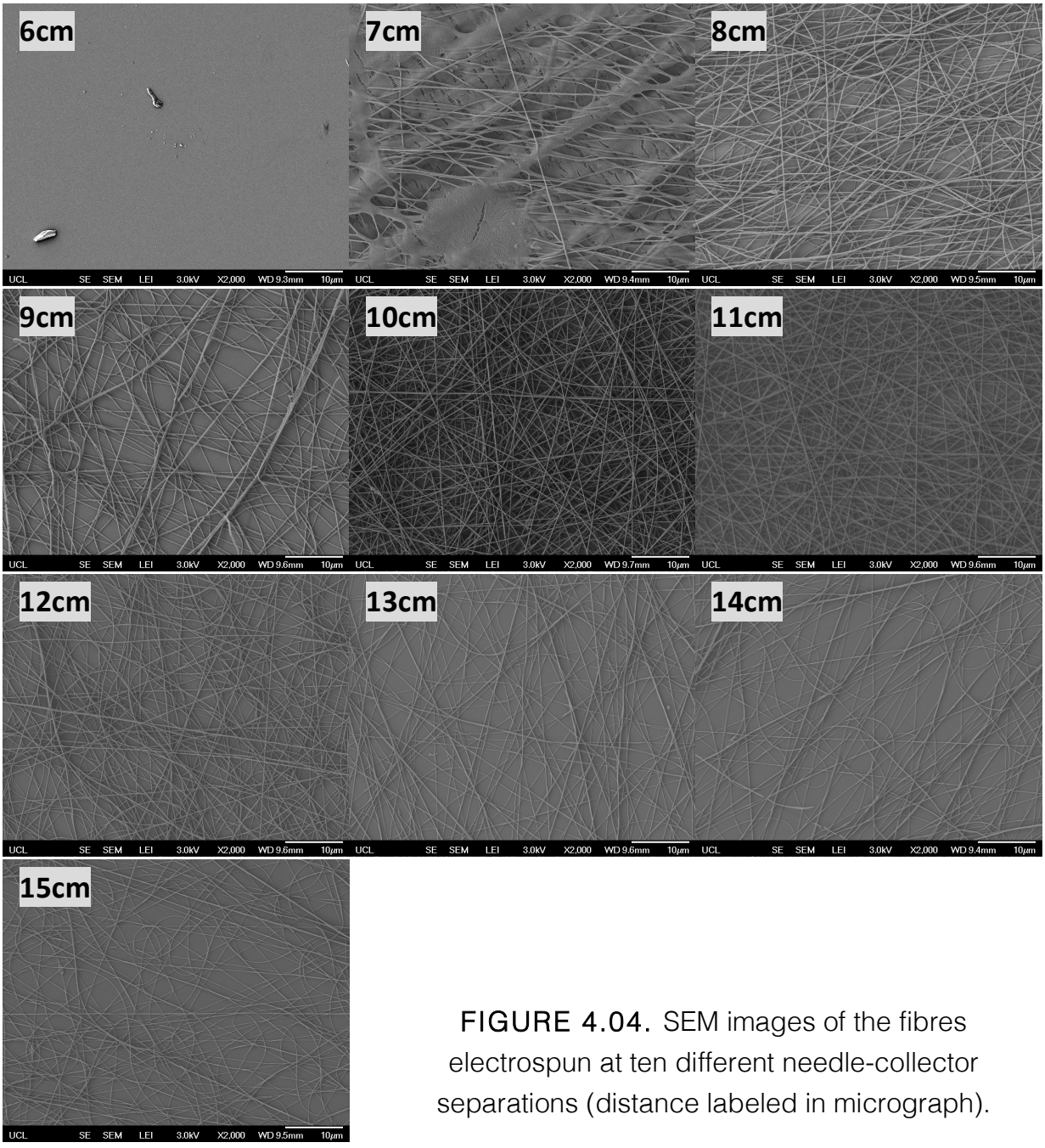

FIGURE 4.04. SEM images of the fibres electrospun at ten different needle-collector separations (distance labeled in micrograph).

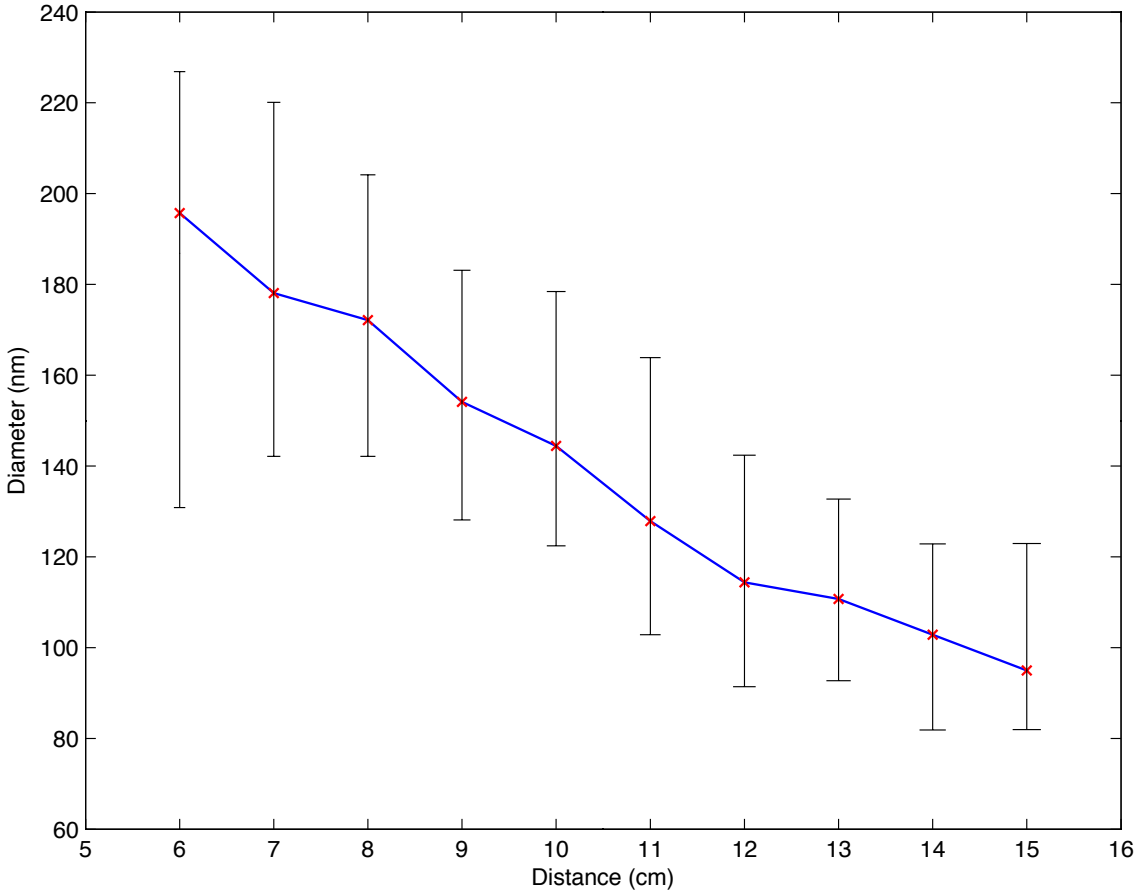

FIGURE 4.05. The effect of collector distance on the diameter of electrospun fibres. Fibres above the optimal distance (10cm) were smaller in diameter but suffered from continuous break up due to the extend distance.

Figure 4.05 demonstrates the gradual reduction in fibre diameter over the range of distances used in this study. Although the SEM images recorded for samples between 11cm and 15cm distances may represent an even fibre profile, there was consistent break-up of fibres, and therefore distances above 10cm were not considered as they are not continuous or linear in structure.

Figure 4.06 represents the diameter distribution of 100 sampled fibres at the optimal 10cm collector distance. There is still a high proportion of fibres recorded above the mean diameter of 144nm and this was specifically associated with a potential break up of fibres within the jetting region. Breaking up of fibres could explain the smaller diameters seen where the continuous jet is disrupted and the thinner tail is deposited. Regardless of jet break up, this was not evident in the SEM images recorded at a jetting distance of 10cm and was more common between samples electrospun at 12cm – 15cm but could potentially explain the range of thicknesses recorded post-SEM.

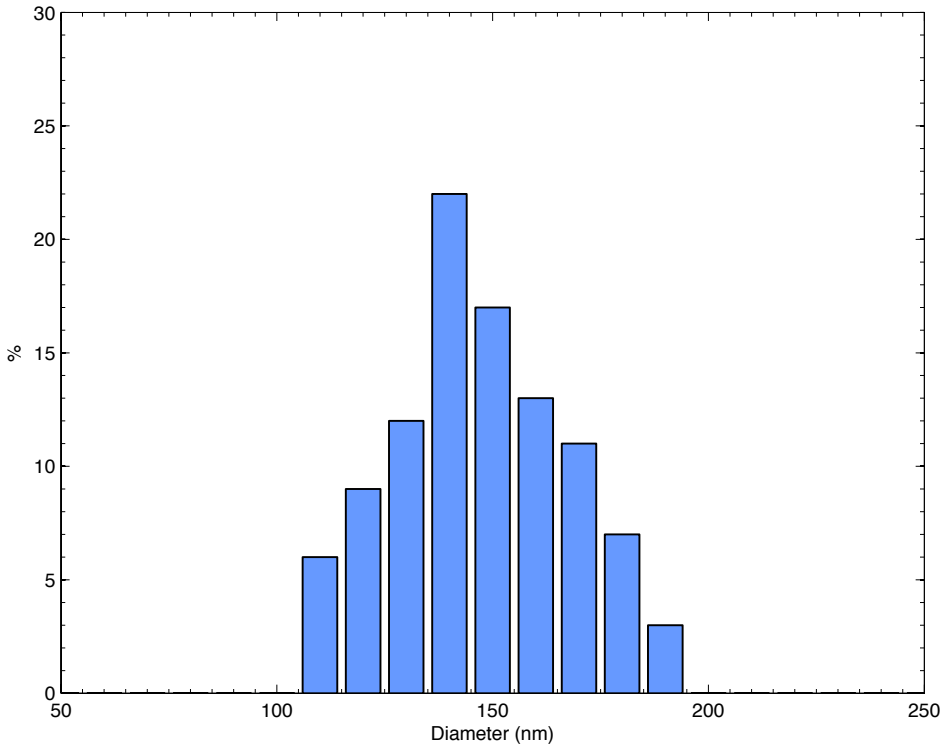

FIGURE 4.06. Histogram showing the frequency distribution of fibre thicknesses recorded at 10cm collector distance.

4.3 CHARACTERISATION OF GOLD NANOPARTICLES

4.3.1 TRANSMISSION ELECTRON MICROSCOPY

Microscopic analysis was used to determine the dispersion of Au NPs. Transmission Electron Microscopy (TEM) micrographs revealed a mean particle diameter of 35.7nm for the citrate-capped nanoparticles. Figure 4.07 reveals Au NPs imaged immediately after homogenization. This was used to encourage particle break up and therefore prevent the aggregation of particles as seen in Figure 4.08 (i.e. without homogenization).

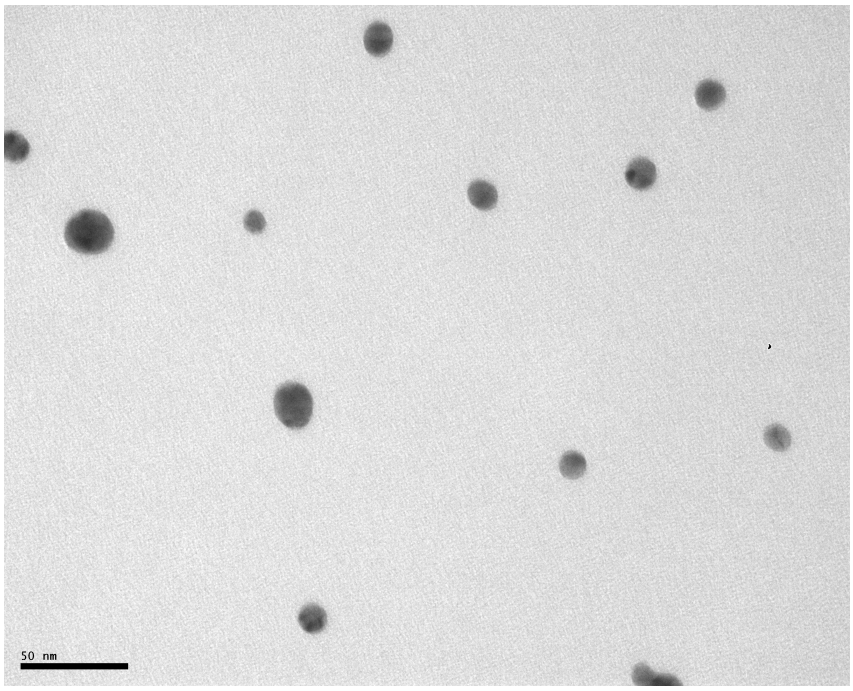

FIGURE 4.07. TEM micrograph of a dried Au NP suspension (with homogenization). Image taken at x80k magnification and accelerating voltage 80kV.

Ensuring nanoparticles are individual is an important factor to consider when preparing polymer/nanoparticle-based composite systems. Control of interparticle spacing will ensure control of the manufactured nanostructure and subsequently the final device structure for functional purpose. The homogenization step taken in this study clearly reveals that passivation of particles alone was not sufficient to prevent aggregation effects (Figure 4.08) within the colloidal suspension and has demonstrated that this is an important preparation step needed for preparing the polymer-colloidal solutions.

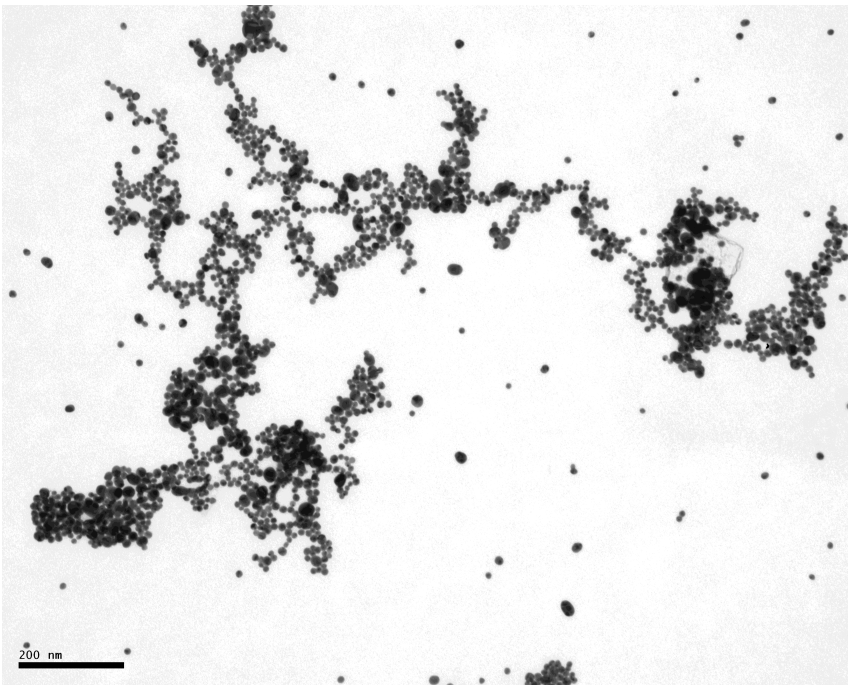

FIGURE 4.08. TEM micrograph of a dried Au NP suspension (without homogenization). Image taken at x150k magnification and accelerating voltage 80kV.

4.3.2 NANOPARTICLE TRACKING ANALYSIS

Particle sizes were analysed using NanoSight NS300 Nanoparticle Tracking Analysis (NTA) (Malvern, UK) instrument and software, which revealed a narrow particle size distribution and size ranging from 25nm up to 80nm. The mean and modal particle sizes are 31.1±0.4nm and 35.2±0.2nm, respectively. All measurements were recorded at 25 ˚C, analysed for multiple runs and the results are shown as an amalgamated plot, Figure 4.09. The particle tracking data verified the results analysed under microscopic analysis and confirmed the particle sizing data manually captured via TEM (section 4.3.1).

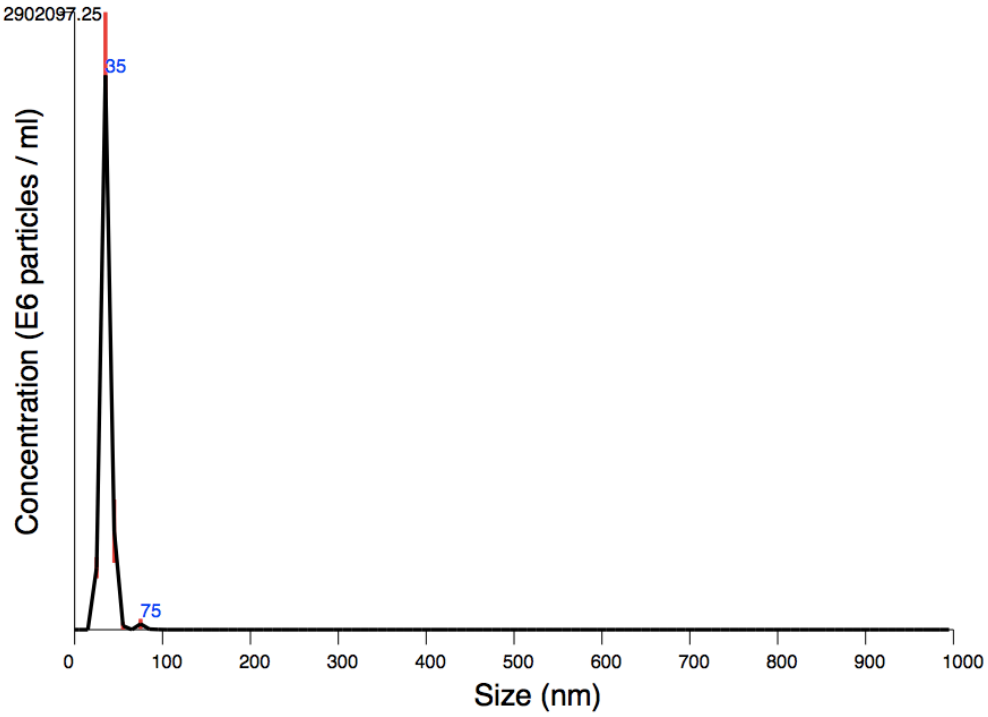

FIGURE 4.09. Au NP size distribution, obtained using nanoparticle tracking analysis. Red vertical lines indicate +/- standard mean error.

4.3.3 UV-VISIBLE SPECTROSCOPY

To examine the presence of metallic AuNPs in solutions, UV/Vis measurements were recorded for each sample, Figure 4.10.

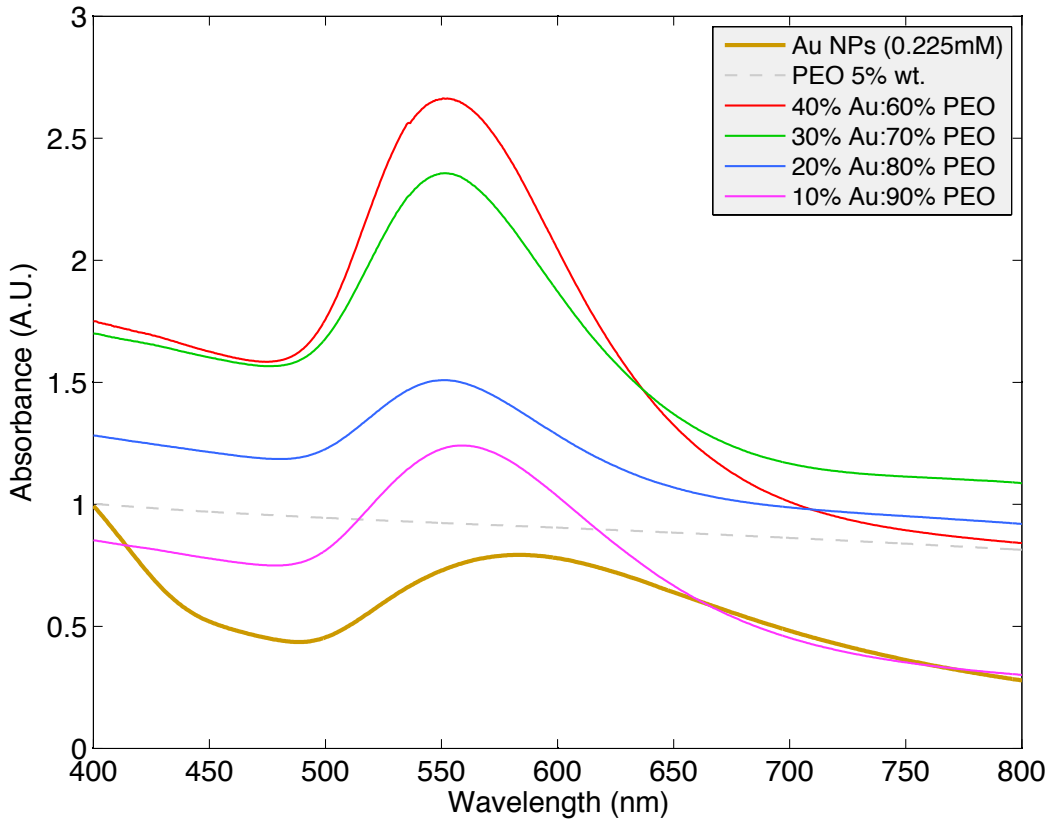

FIGURE 4.10. UV-Vis spectra for as-prepared citrate passivated Au NPs suspension at 0.225mM (solid gold line) in DI water, a 5% wt. PEO control solution (grey dashed line), and solutions containing Au NPs loading at 10% (pink), 20% (blue), 30% (green) and 40% (wt.) (red).

The presence of Au NPs in polymer solutions was determined by

spectroscopic measurements using UV-Visible Spectroscopy (Shimadzu UV-1800 Spectrophotometer). Absorption spectra were recorded over the spectral range 400-800nm (1nm resolution) using quartz cells with a 10mm path length. Detection of the Au NPs in polymer was measured by analyzing the fluorescence emission at 550nm peaks relative to a control sample of Au NPs.

All stabilized PEO/Au NP blends displayed a characteristic absorption peak, which was assigned to the surface plasmon resonance (SPR) band typical of Au NPs [159]. The PEO solution alone had no absorption around 550nm, thus did not interfere with the examination of Au NPs. With increasing Au NP doping concentration, the intensity of SPR peaks amplified accordingly and strengthened the hypothesis that a greater presence of nanoparticles will be visible in the electrospun composite fibres as the concentration is increased.

4.4 CHARACTERISATION OF PEO/AU NP COMPOSITES

4.4.1 SOLUTION CONDUCTIVITY VS. CONCENTRATION

The electrospinning jet is caused by surface charges on the spinning solution and it is clear that if the conductivity of the solution is increased the jet can carry more charges to encourage uniaxial stretching to produce thinner fibres. Later, SEM analysis will reveal the dependence of fibre thickness on the solution conductivity. The addition of metallic Au NPs determined the solution conductivity for the nanofibre composites and by increasing Au NP loading concentrations, the solution conductivity increased (Figure 4.11).

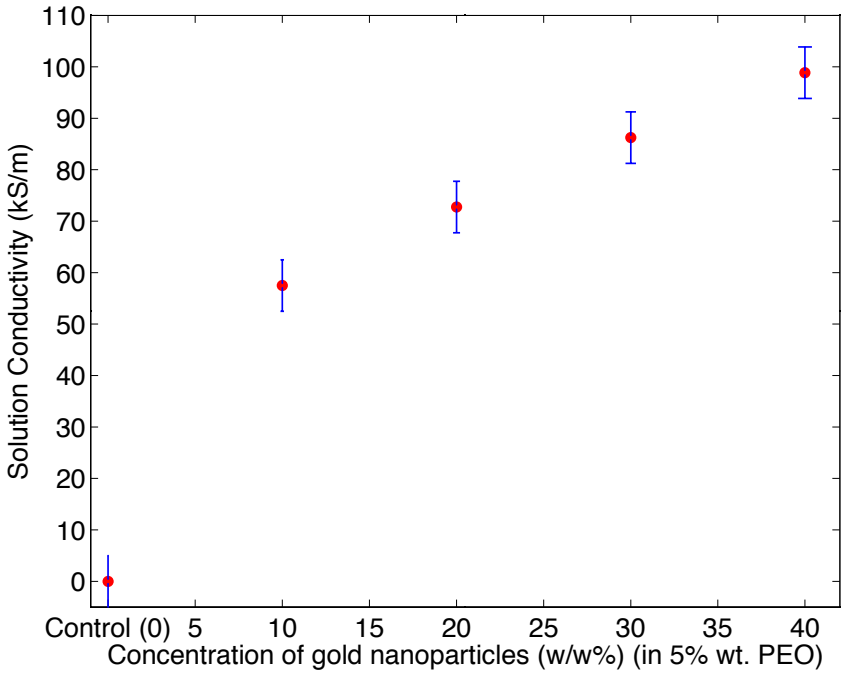

FIGURE 4.11. The effect of gold nanoparticle loading on the solution conductivity.

4.4.2 SCANNING ELECTRON MICROSCOPY

Polymer/gold composites were structurally characterized using SEM to examine their morphologies. The images captured can be seen below in Figure 4.12 although do not expose the nanoparticles. The dispersion of nanoparticles will be analysed in section 4.4.4. SEM was used simply to determine the thickness of composites and examine whether fibres were structurally altered due to the presence of Au NPs in the solution. A control sample (without Au NPs) was electrospun to comparatively examine whether any clear change was visible with the fibres containing nanoparticles.

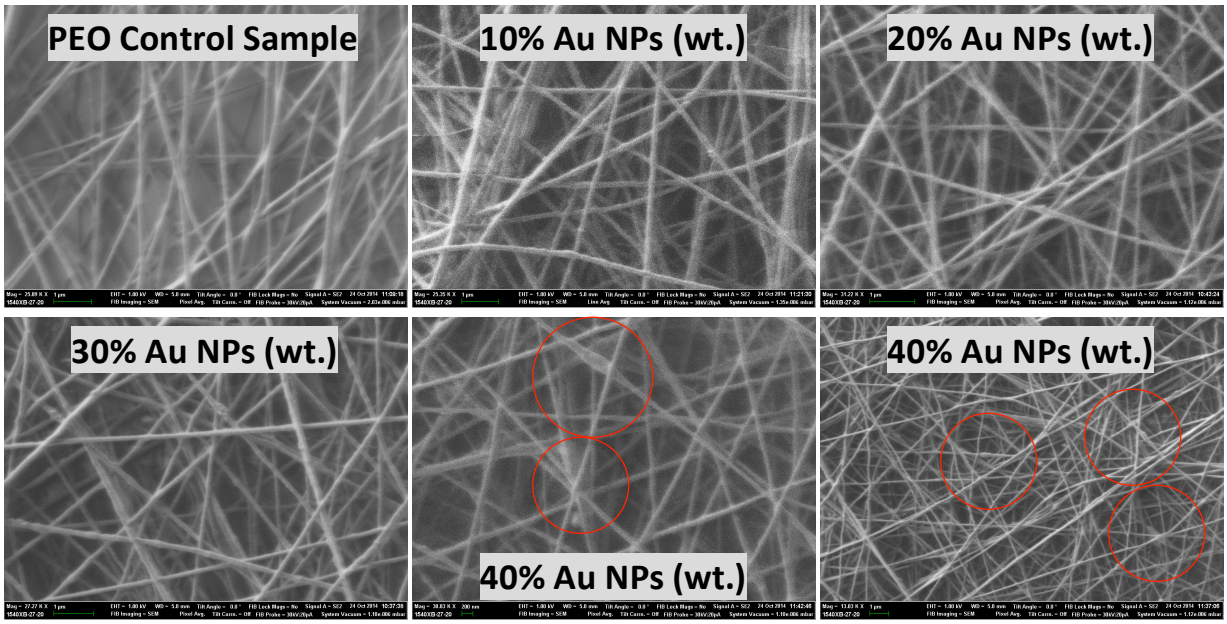

FIGURE 4.12. SEM images of the composite fibres electrospun at four concentrations with a control sample (labeled in micrograph). Red (solid line) circles highlight the presence of minor beading within the composite fibres.

Increasing Au NP loading concentrations effectively reduced the diameter of fibres (Figure 4.13) and introduced very minor beading effects at greater loading. This is most likely the result of an increase in solution conductivity (Figure 4.11), suggesting that higher conductivities induced greater electrostatic forces on the droplet tip and caused greater stretching and elongation of the polymer droplet to produce thinner fibres, simultaneously triggering fibre break-up. The graph seen in Figure 4.13 (section 4.4.3) reveals a clear dependence of fibre thickness on the concentration of Au NPs in the spinning solution. With solutions containing Au NPs, thicknesses of fibres ranged from 116nm – 141nm in size. Also to note, at higher gold concentrations, the presence of beads and spindle-shaped structures were observed. Specifically at a 40% (wt.) nanoparticle loading, minor beading effects were noted (red circles highlight beading in Figure 4.12). This is a result of the greater degree of stretching and fibre break-up.

4.4.3 FIBRE DIAMETER VS. AU NP CONCENTRATION

The results seen below in Figure 4.13 reveal the clear dependence of the thickness of electrospun fibres on the concentration loading of Au NPs.

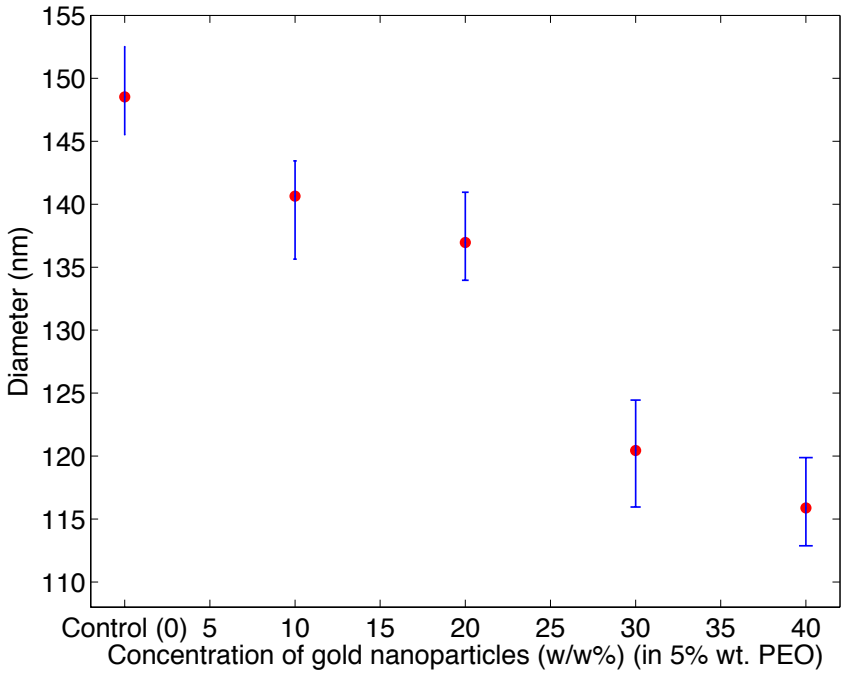

FIGURE 4.13. The effect of gold nanoparticle loading on the diameter of the electrospun composite fibres.

We can conclude that higher conductivities induce greater electrostatic forces on the droplet tip and cause greater stretching and elongation of the polymer droplet to produce thinner fibres. However, there is a limit to the reduction in fibre diameter. As the solution is stretched, there is a greater viscoelastic force acting against the Coulombic forces and this may encourage fibre break-up and contribute to the introduction of minor beading at higher Au NP loading,

which was evident at 40% (wt.) Au NP concentration. To overcome the presence of beading in fibres, the addition of surfactants, salts, acids and alcohols could be used in the precursor formulation. The addition of these substances have previously been shown to manufacture fibres with fewer beads or bulky structures [68, 73].

Two primary reasons for avoiding the addition of surfactants, salts, acids and alcohols (e.g. ethanol) in this study was simply to keep the solution formulation simple without the addition of chemical precursors that would adjust the surface tension of the solution. Controlling surface tension of electrospinnable solutions is extremely difficult and is known to produce non-linear behaviour, effectively limiting the reproducibility control of the study. Secondly, the addition of these substances will raise the charge of the jet, leading to greater instability of the jetting process, which results in fibres being deposited over a larger area, offering less control over the process [73]. Furthermore, avoiding a jet that is undergoing greater instability is key to manufacturing functional nanodevices. A jet offering minimal control over the deposition of fibres is more difficult to control and is not specifically suited for the printing of composite fibres as tracks for wiring nanocomponents. Therefore, minimal efforts were taken here to address the beads visible at 40% (wt.).

In conclusion, the concentration offering a composite fibre manufactured with the smallest diameter, yet retaining its uniform morphology, was 30% (wt.). This was also achieved at nanoparticle concentrations of 10% and 20% (wt.) although 30% (wt.) retains the highest concentration of Au NP, important for achieving a highly doped nanoparticle assembly.

4.4.4 TRANSMISSION ELECTRON MICROSCOPY

The dispersion of Au NPs within the electrospun fibres was examined by TEM. TEM images were obtained of composite fibres electrospun directly onto carbon-coated Cu holey grids. This enabled the nanoparticle composites to be imaged as nanofibres were deposited over holes in the holey carbon films to minimize variation in the background contrast.

Figure 4.14 shows the first sample containing Au NPs at 10% (wt.) in PEO. Thinner fibres were obtained with a 10% (wt.) loading (relative to the control sample), although gold nanoparticle clusters can be seen within nanometer-sized beads, represented by the blue solid line. These tiny beads were not visible under SEM analysis. Such tiny-beaded fibres can form as a result of surface tension forces causing the PEO solution to build up at the needle orifice of the electrospinning jet [23]. Once the repulsive forces of the charged solution overcome the surface tension forces, jetting occurs from the point of the bead as it detaches from the needle tip, leaving a fibre with a bead-like morphology, which can explain the build-up of Au NP clusters within the composite nanofibres. Furthermore, it is possible for Au NPs to aggregate in the solution as the droplet size increases in size. This observation may be related to the differences in surface tensions between bead formation and non-bead formation, resulting in an increased particle density within the beads [23]. This could be overcome by increasing the flow rate to the emitter however control of the fibre diameter and morphology will be compromised.

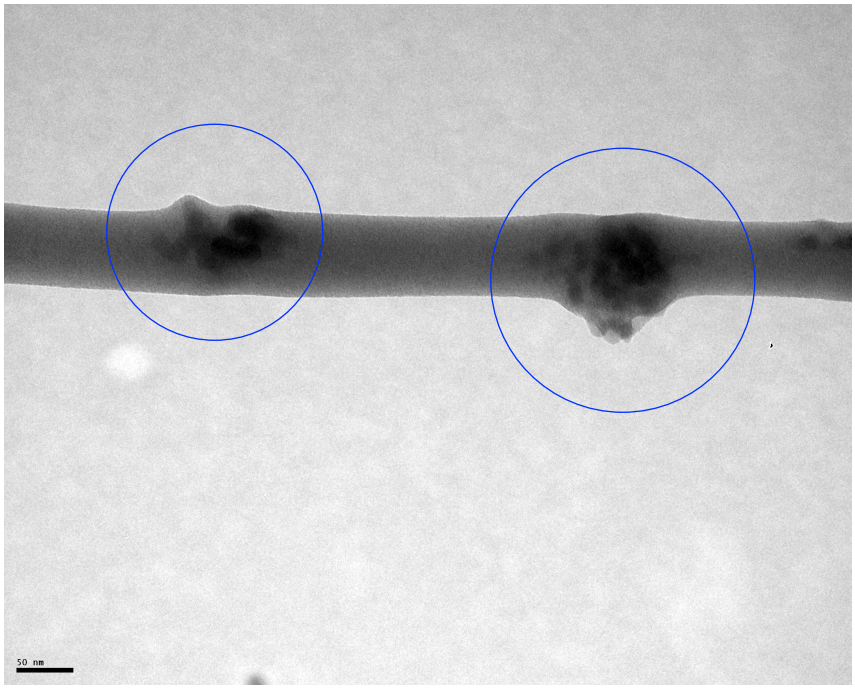

FIGURE 4.14. TEM image of a single fibre electrospun at 10% (wt.) Au NP concentration containing nanoparticle clusters (circled in blue solid line).

Au NPs appear as dark black spots inside the nanofibre structures and from Figures 4.15 and 4.16, there is clearly a denser population of Au NPs with increases in nanoparticle concentration. At 20% (wt.) (Figure 4.15), particles appeared individually and have fewer clusters than seen at 10%. 30% and 40% (wt.) concentrations revealed greater populations of nanoparticles although there is more evidence of aggregation and particle clusters. The nanoparticles tend to pack together within the nanofibres, possibly due to agglomeration in the polymer solution, although more importantly, isolated nanoparticles were also observed at all electrospun concentrations.

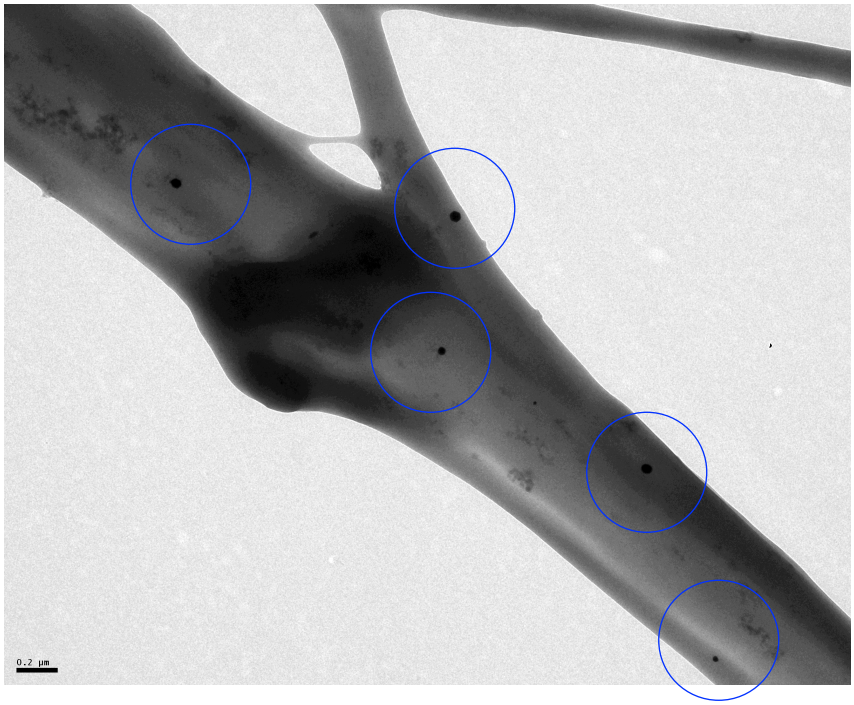

FIGURE 4.15. TEM image of a single fibre electrospun at 20% (wt.). Individual nanoparticles can be seen in the blue circles.

The nanoparticles seen at 30% (wt.) revealed dark regions of fibres under TEM analysis (Figure 4.16). The darker regions suggest a denser population of nanoparticles however lighter regions without any dark spots suggest the total absence of nanoparticles. This could be due to the nanoparticles having settled in the syringe whilst the solution is pumped and electrospun. Additionally, the resolution is limited by the power of the microscope and it should therefore be possible to resolve the smaller clusters at higher beam energies. Fortunately, the particles were found to be stable (within PEO nanofibres) in the beam in contrast to those dried particle suspensions loaded onto carbon films which showed considerable instability during imaging, so there is a high probability that the samples will remain stable when imaging at

higher beam energies.

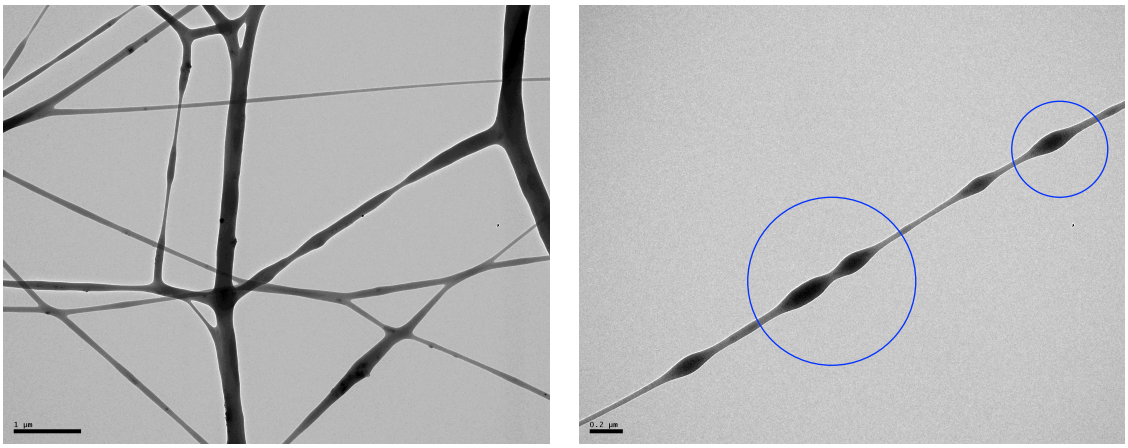

FIGURE 4.16. TEM images of single fibres at 30% (left) and 40% (wt.) (right) Au NP concentrations. Bead morphologies (circled in solid blue line) were common amongst samples electrospun at 40% (wt.).

In conclusion, fibres containing Au NPs revealed an uneven distribution of nanoparticles throughout the nanofibres and this was generally common amongst all concentrations. The length of these assemblies are several hundreds of micrometers, a common feature attributed with the benefits of electrospinning technology.

4.4.5 SCANNING TRANSMISSION ELECTRON MICROSCOPY

Scanning Transmission Electron Microscopy (STEM) analysis was performed on all samples containing nanoparticles. In the bright field mode, the intensity of the images is inversely proportional to the local atomic number of the sample material, so Au NPs show bright contrast and the polymer appears dark (see Bright Field STEM images captured in Figure 4.17). Images were acquired using a higher resolution microscope operated at an acceleration voltage of 80 kV to minimize damage to the beam.

Interestingly from the observations noted in Figure 4.17, several of the nanofibres exhibit nanochain-like Au inclusions, and protrusion of Au NPs is also evident from the fibre surface. This can be attributed to the combined effect of the applied electric field on the polymer and the differences between the electrical conductivity and polarizability of the polymer and the Au NPs. Because the nanoparticles are solids, the polymer chains must stretch around these obstacles, causing a loss in conformational entropy that increases with particle radius. In the absence of specific interactions, larger nanoparticles are expelled from the bulk of the polymer, whereas smaller particles are not. This significantly affects the spatial distribution of nanoparticles within the global structure of the particle-filled systems. Additionally, localized alignment of Au NPs to form short nanochains at 10% (wt.) Au NP loading was observed. Previously it has been shown that orientation of polarizable dielectric colloidal species can be produced by the presence of an electrical field by inducing mobility and interaction between particles through dielectrophoretic process [97, 161]. In turn, the interactions between the dipoles induced in the particles can initiate assembly during electrospinning and lead to formation of particle chains [162].

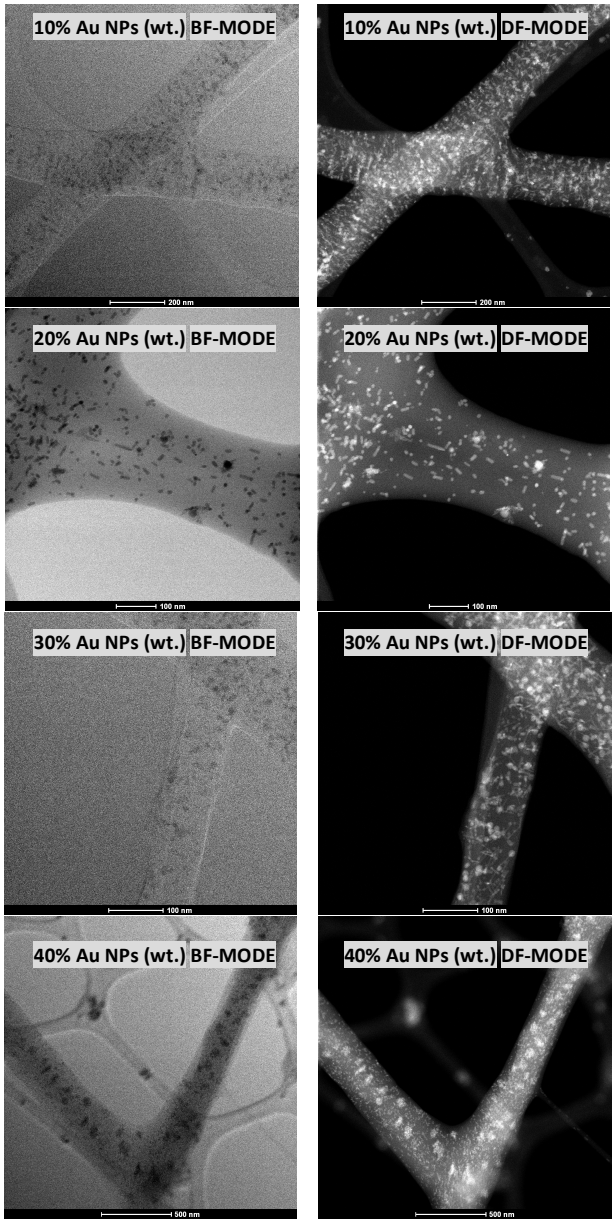

FIGURE 4.17. Bright-Field (BF) (left column) and Dark-Field (DF) (right column) STEM images of electrospun composite fibres. DF STEM images illustrated a clear contrast between the polymer matrix and Au NPs.

Evidently there is an increasing number of particles present within the polymer fibres as the concentration increases; however, we can see that at 40% (wt.) of Au NP concentration, particles have clustered together, evident by the brighter regions within the electrospun fibres. This was not so evident in samples electrospun at 30% (wt.) however the structures of individual nanoparticle chains seen here were similar to the assemblies seen at 10% (wt.). 20% (wt.) was the only sample to expose clearly individual nanoparticles, validating the findings seen under TEM analysis.

To aid in the understanding of the STEM images obtained here, a study by Saquing et al. [97], describes that electrospinning PEO acts as both the reducing agent for the metal salt precursor and the protecting agent for the resulting metal nanoparticles in solution. Although this work involves the use of as-prepared Au NPs before mixing the polymer-nanoparticle complexes, remaining gold metal salts may not be fully reduced through the initial preparation (as samples are not repetitively filtered), which might explain the non-spherical elements present in the fibres. Filtration of the solutions repetitively prior to electrospinning will be extended for the follow on studies to ensure reduction agents are not present in the spinning solutions. Furthermore, low molecular weight PEO has been shown to transform Au complexes (using $NaAuCl_4$ and $HAuCl_4.3H_2O$ as precursors) into their corresponding Au NPs in an aqueous system at ambient conditions [97, 163].

Aside from its reduction potential, PEO can also act as a stabilizer for Au. Reports in the literature suggest that in the presence of an excess of capping agents (i.e. citrate-ligands), digestive ripening is known to occur for gold and silver nanoparticles even in mild conditions. Digestive ripening is the break up of larger particles into smaller monodisperse nanoparticles, which might make it difficult to distinguish from the TEM images recorded here relative to the

control sample. With such a large amount of PEO polymer present (PEO/Au mass ratio 90:10 or 80:20), it could provide the necessary conditions for digestive ripening to occur [164, 165]. Figure 4.17 reveals that at lower concentrations of Au NP (i.e. higher concentration of polymer), specifically at 20% (wt.), particles appear individual and monodisperse whereas at higher concentrations of Au (i.e. 30% and 40%), particles have clustered together to form bulk structures of Au. Due to the smaller amounts of PEO in the solution, there is less chance that digestive ripening will occur. Digestive ripening can significantly reduce the average particle size and polydispersity [164]. Many particles significantly smaller than the average Au NP size (i.e. 35nm) were visible under STEM imaging although remained highly monodisperse, a feature commonly attributed to digestive ripening processes. The process generally involves the refluxing of Au NPs in the presence of an excess capping ligand and transforms even an extremely polydisperse colloid into a highly monodisperse one.

In summary, composite fibres have been electrospun containing citrate-capped Au NPs encapsulated within PEO polymer. The fibres were electrospun using process parameters optimized for polymer concentration and electric-field strength (i.e. distance between tip and collector). SEM, TEM and STEM analysis were used as effective imaging tools to analyze the morphology of fibres and expose dispersions of nanoparticles within the polymer matrices. Scanning Transmission Electron Microscopy proved most effective in analyzing single fibres containing Au NPs and Dark Field imaging effectively revealed the nanoparticle distribution within the fibres, discriminating by contrast using the local atomic number of the material. This is the first time STEM has been used for electrospun PEO/Au NP composites.

5. RESULTS

ELECTRICAL PERFORMANCE STUDIES

Resistive switching is a rapidly developing field. Two-terminal resistive switching devices have generated broad interest among industry and academic researchers for potential, industry-disruptive memory and logic applications [166-169]. Experimentally, resistive switching devices are usually fabricated with a metal-insulator-metal (MIM) structure, in which “M” could be any metal or compound electrode material with high conductivity and “I” is one or multiple switching medium layer(s) sandwiched by the two conducting electrodes [169].

In this chapter, we have combined the economical merits of manufacturing (using electrospinning) the insulator layer with the PEO/Au NP-based nanocomposites produced using the techniques outlined in Chapter 4. Using the MIM configuration, the composite fibres so manufactured were tested for their resistive switching potential using the nanodevices fabricated in Section

5.1 below. I-V measurements were recorded for devices manufactured with three different contact electrodes: aluminium (Al), chromium (Cr) and platinum (Pt). The concentration of gold nanoparticle loading within the fibres was also varied for each test with different electrodes. The following gold nanoparticle loading concentrations were used for each device: 10%, 20%, 30% and 40% (wt.). These are the first attempts to measure the electronic resistive switching performance of electrospun PEO/Au NP-based nanocomposites.

5.1 FABRICATION OF NANODEVICES

The typical construction of PEO/Au NP based-nanodevices is shown in the schematic below, Figure 5.01, which illustrates a device with chromium contacts. Each device was prepared using a Si substrate with a thick (4μm) thermal oxide layer (SiO_2) to electrically isolate the device from the substrate. The fibres were electrospun onto an evaporated metal layer (either Al, Cr or Pt) on top of the SiO_2, which formed the bottom contact. The thickness of the insulator layer (i.e. the electrospun composite fibres) was ≈3.3-3.5μm across all samples. The range of insulator layer thickness stems from the random deposition of fibres on the substrate. As fibres are electrospun at high electric fields (>0.5kV/cm), the Taylor cone is less stable and smaller in size, which causes greater jet instability therefore the deposition of fibres is random on the substrate. This random deposition subsequently affects the thickness across the layer.

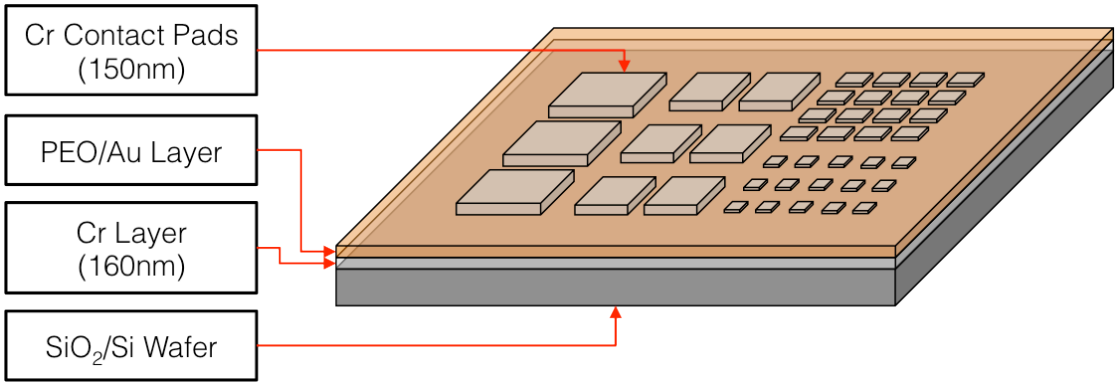

FIGURE 5.01. Schematic of the electrospun PEO/Au NP device structure for electrical I-V measurements. The electrospun composites are sandwiched between the metal electrodes and form the dielectric (insulator layer).

The electrodes were deposited by thermal evaporation. Thin metal layers of 150nm were deposited onto different glass slide substrates by thermal evaporation through shadow mask. The resulting square electrode contact pads were of four different sizes: 200μm×200μm, 400μm×400μm, 600μm×600μm and 800μm×800μm. Connection to the electrodes for each sample was made using two 1.25" Signatone tungsten contact probes (SE-10T); current was measured when applying varying voltage sweeps up to +/-30V. Compliance current was set to 100mA.

In order to demonstrate whether thermal evaporation of the top metal contact lead to thermal degradation of the nanofibres (below the contact), SEM images were acquired to reveal the cross-section of the fibres and their microstructure, shown in Figure 5.02 (d). No thermal degradation was seen as the nanofibres retained their microstructure, as seen in Figure 5.02 (b) and (d). Furthermore, thermal evaporation of metal meant the top contact layer was deposited following the contour of the nanofibre layer, as seen in Figure 5.02 (b).

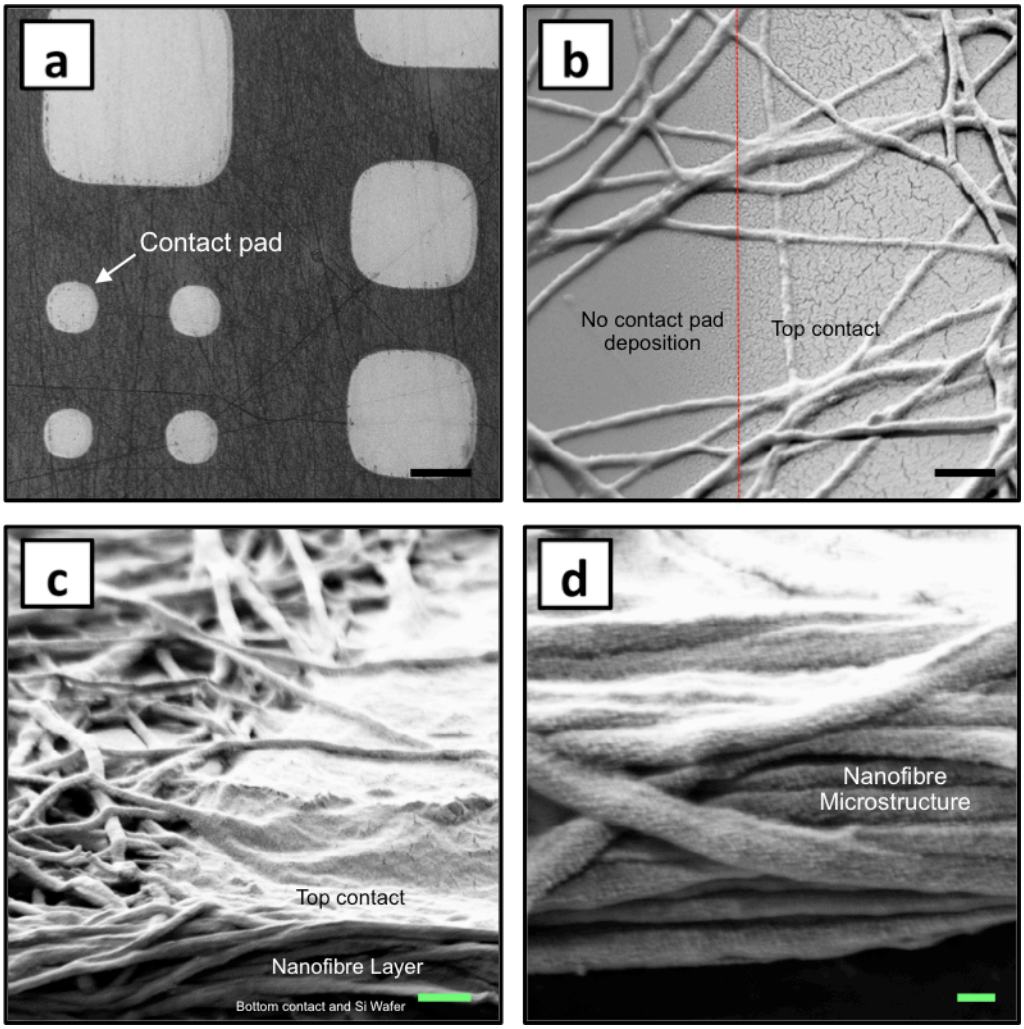

FIGURE 5.02. SEM micrographs of the MIM structure. (a) Top view of the contacts (scale bar: 200μm), (b) Top view of the interface between the contact pad and region of the device without contacts demonstrating no thermal degradation of the fibres (scale bar: 1μm), (c) Cross-sectional view of the nanofibre layer with top contacts (scale bar: 1μm) and (d) cross-sectional view of the nanofibre layer (scale bar: 400nm).

5.2.1 Al CONTACTS – I-V MEASUREMENTS

Measurements recorded on aluminium contacts with electrospun pristine PEO nanofibres revealed no evidence of switching behavior, as expected (Figure 5.03). For pristine samples, charging is expected as the dielectric prevents charge from moving from one electrode to the other; it behaves like a capacitor. Figure 5.02 shows an I-V loop ($0V \rightarrow V_{max} \rightarrow 0V$) for pristine PEO devices. The curve demonstrates that the sample is highly resistive, as the current is very low (10^{-11} A) (point '1'). The region between 1V and 6V (bottom curve, point '2') is very unstable although the reason for this instability isn't immediately clear.

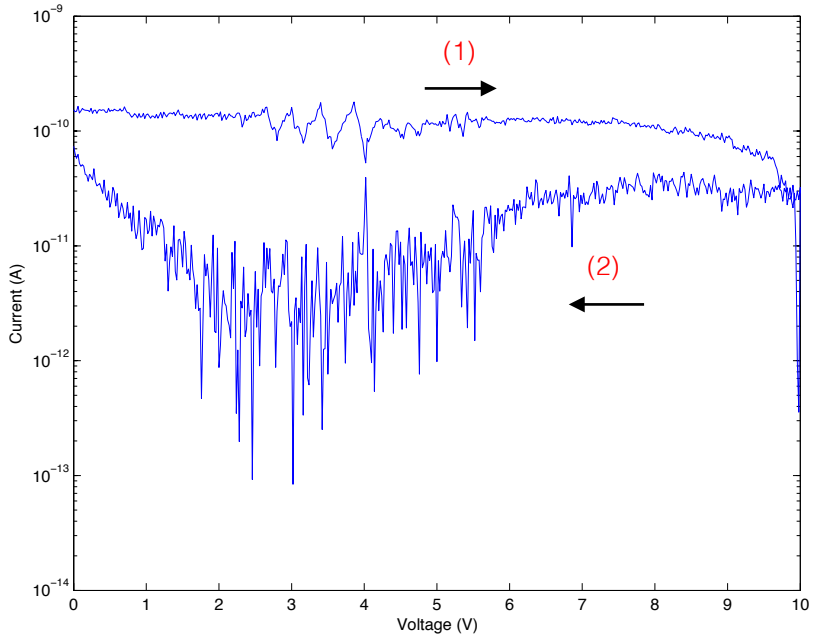

FIGURE 5.03. A typical I-V curve of a pristine PEO device.

Following this, I-V measurements were performed on devices electrospun with encapsulated Au NPs to see whether resistive switching could be achieved when the nanofibres were loaded with Au NPs. The electrospun PEO/AuNP device with a 30% (wt.) Au NP loading exhibited very interesting bistable electrical behaviour, seen in Figure 5.04. As the potential is increased, an abrupt change in current is observed (point '1' on the I-V curve) at +2.5V. This changes the device from a low current (10^{-10} A) OFF state to a high current (10^{-6} A) ON state. The device is stable in the ON state up to a potential of +4.7V. At this point, there is an additional switching event where the device switches back again to the high resistance state (point '2'). At +8V there is another change in current to the ON state (point '3') although the change in current is smaller than the previous switch (10^{-7} A) and this returns back to the OFF state (point '4') at +9V. This device thus demonstrates unipolar switching behavior, as the ON and OFF state voltages have the same polarity.

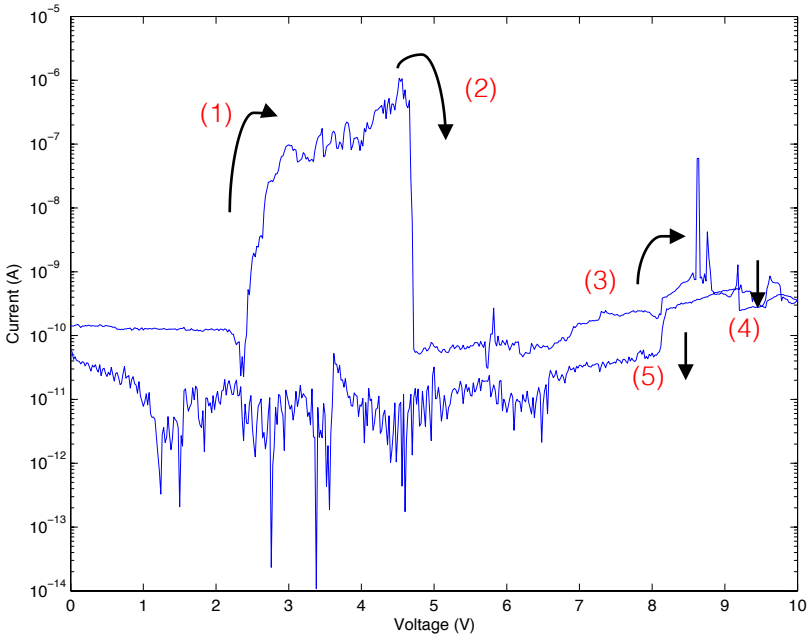

FIGURE 5.04. I-V curve of PEO nanofibres at a 30% (wt.) Au NP loading, showing unipolar resistance switching.

5.2.2 CONDUCTION MECHANISM ANALYSIS

Conduction mechanism analysis provides an insight into the resistive switching behaviour seen in Figure 5.04 and also indicates which mechanism is responsible for the conduction in different states. The conductance depends on the applied electric field. The electric field strength (*E*) through the insulator is expressed by the following equation.

$$E = \frac{V}{d} \quad , \qquad (1)$$

Where, *V* is the applied voltage across the insulator and *d* is the insulator thickness.

In this study, measurements were all performed at room temperature (21°C). The most commonly reported conduction mechanisms through dielectric materials are Fowler-Nordheim, Poole-Frenkel and Trap-assisted Tunnelling (TAT). These are described below in more detail.

Direct and Fowler-Nordheim Tunnelling

Tunnelling is the most common conduction mechanism through thin insulators under high fields. Tunnelling could be direct tunnelling where the electron tunnels through the complete width of a barrier, or Fowler-Nordheim tunnelling where the electron tunnels only through a trapezoidal barrier whose effective width is modified by an applied field, shown below in Figure 5.05.

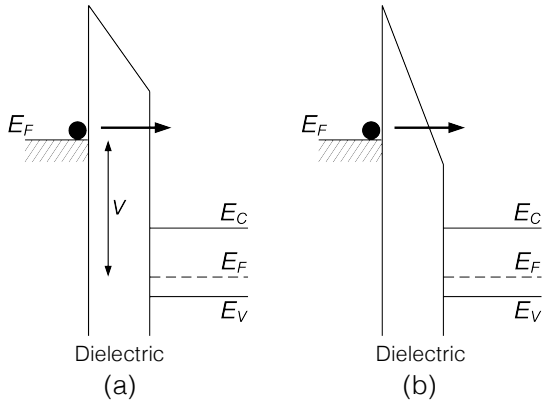

FIGURE 5.05. Energy-band diagram showing the conduction mechanism for (a) Direct Tunnelling and (b) Fowler-Nordheim Tunnelling [170].

Direct tunnelling is likely to occur in ultra-thin insulators (<4nm) during which electrons from the conduction band are transferred across the insulator directly (i.e. without changing energy). The probability of direct tunneling is a very strong function of the width of the barrier the electron tunnels through (i.e. dielectric thickness) and is very unlikely to occur for samples prepared in this study as nanofibre thin films are ≈3.3-3.5μm thick. The expression connecting current density and dielectric thickness is:

$$J_{DT} = \frac{A}{t^2}\exp\left[-2t\sqrt{\frac{2m^*q}{\hbar^2}}\left(\emptyset_B - \frac{V}{2}\right)\right], \qquad (2)$$

Fowler-Nordheim tunnelling relies on a trapezoidal potential barrier, the width of which depends exponentially on the applied field. This tunnelling mechanism is most likely to dominate in structures that are >10nm in thickness. The expression connecting the current density and the electric field in the layer is:

$$J_{FN} = C_{FN}E^2 \exp\left(-\frac{4}{3}\frac{\sqrt{2m^*}}{q\hbar}\frac{(q\emptyset_B)^{\frac{3}{2}}}{E}\right), \qquad (3)$$

The most convenient way to check this mechanism is to plot the experimental I-V characteristic in the form $ln(\frac{J_{FN}}{E^2})$ versus $\frac{1}{E}$. [170] This representation is called a Fowler-Nordheim plot and will yield a straight line if F-N tunnelling is dominant.

Poole-Frenkel Conduction

Conduction may occur without tunnelling. The Poole-Frenkel conduction mechanism describes electrons that are trapped in localized states. The electrons gather enough energy through thermal fluctuations to leave the localized state and move to the conduction band of the dielectric (Figure 5.06). The rate of this excitation of electrons to the conduction band is not high at room temperature, but if a high field is applied, electrons don't require as much thermal energy to be excited as the barrier for thermal detrapping is lowered by the field.

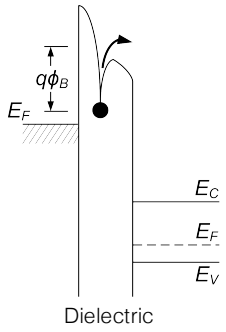

Figure 5.06. Energy-band diagram showing Poole-Frenkel emission. The barrier for thermal detrapping of the electron is lowered by the field [170].

The expression relating the current density and the electric field is:

$$J_{PF} = qn_0\mu E \exp\left[-\frac{q}{kT}\left(\emptyset_B - \sqrt{\frac{qE}{\pi\varepsilon}}\right)\right], \qquad (4)$$

The Poole-Frenkel plot can be represented in the form $ln(\frac{J}{E})$ versus $E^{0.5}$ [170]. For evidence of the Poole-Frenkel effect, the plot should yield a straight line.

Trap-assisted Tunnelling

Where Fowler-Nordheim tunnelling is a one-step tunnelling process, there is also the possibility that any defects (or electron traps) inside the insulator layer allow the tunnelling process to consist of two or more steps. This is referred to as Trap-assisted Tunnelling (TAT) (Figure 5.07). Carriers sequentially tunnel across a series of thin barriers.

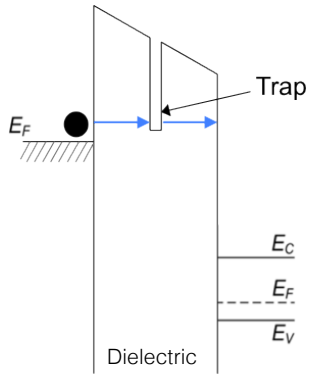

Figure 5.07. Energy-band diagram showing Trap-Assisted Tunnelling (TAT).

A TAT expression relating tunnelling current density with trap barrier height has been proposed and shown to be valid at high electric fields [171].

$$J_S \propto \exp\left[-\frac{8\pi\sqrt{2qm^*}}{3hE}\,\Phi_t^{\frac{3}{2}}\right], \qquad (5)$$

Where, $m^*$is the electron effective mass, h is Planck's constant and Φ_t is the trap barrier height. The most convenient way to check this mechanism is to plot the experimental I-V characteristic in the form $ln(J)$ versus $\frac{1}{E}$. A straight line results if TAT is dominant [170].

5.2.3 ALUMINIUM CONTACTS – CONDUCTION MECHANISM RESULTS

For the resistive switching behaviour observed in Figure 5.04 for the Al electrode (30% (wt.) Au NP concentration in the PEO), Fowler-Nordheim, Poole-Frenkel and TAT do not show a good fit with our results. Data was chosen in the voltage range of 5-7V (upper curve in Figure 5.04). Figure 5.08 provides plots for all three conduction mechanisms.

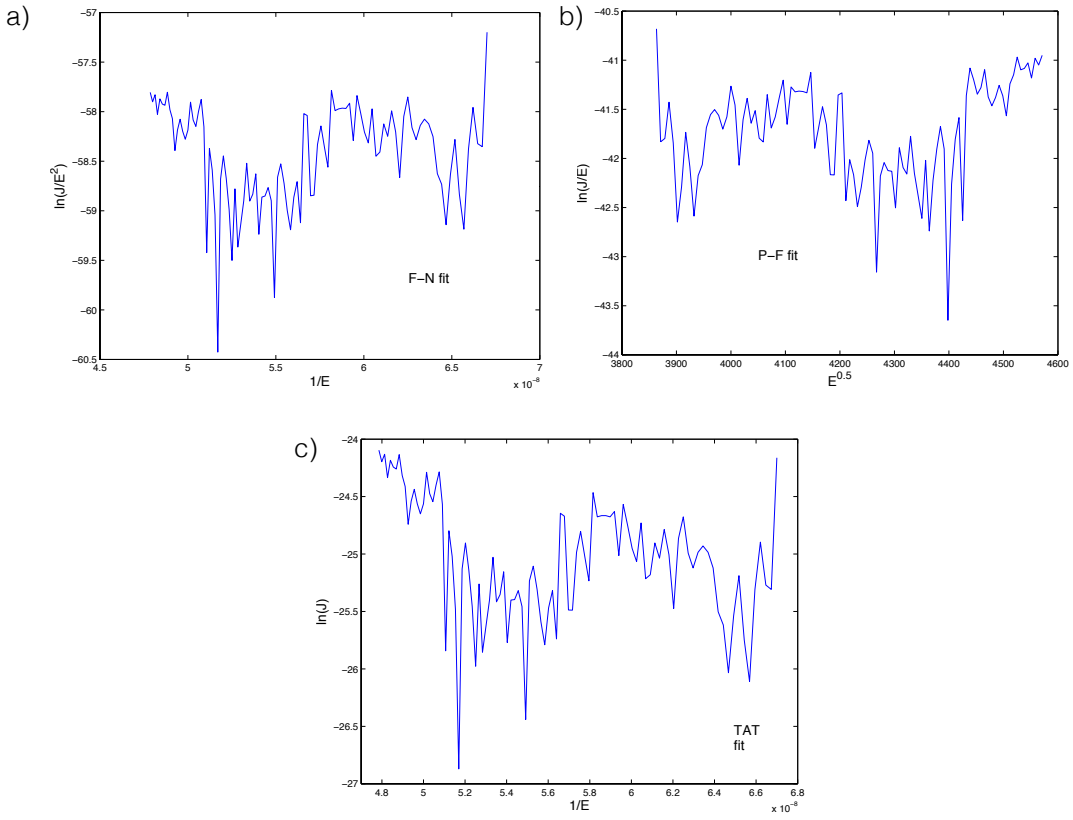

FIGURE 5.08. Plots for voltage range of 5-7V for the 30% (wt.) Au sample. (a) Fowler-Nordheim. (b) Poole-Frenkel. (c) Trap-assisted Tunnelling. Evidently, none of these mechanisms describes current transport in this sample.

It is clear that the plots in Figure 5.08 are highly non-linear and hence the conduction in Figure 5.04 is not described by Fowler-Nordheim, Poole-Frenkel or TAT conduction mechanisms. It is worth noting that one or more mechanisms may simultaneously exist in the sample, although this strongly depends on the range of voltages used, the concentration of Au NPs and distribution of nanoparticles in the thin film insulator. Furthermore, it may also be possible that the electrodes deposited through thermal evaporation may cause Al atoms to diffuse between fibres. These atoms can migrate under the application of an electric field and therefore form filaments for charge transport between the metal contacts.

5.3.1 CHROMIUM CONTACTS – I-V MEASUREMENTS

The contact pad for devices was changed to chromium to investigate whether the electrode material had any influence on the resistance switching of the devices. Unlike aluminium, chromium provides a hard surface. Aluminium is a softer, ductile metal and therefore the application of a long, thin probe proved difficult when making connection to the top electrode. Regardless for all measurements the probe did not pierce through. If the probe penetrated through the electrode, this would have caused an electrical short in the system.

Measurements recorded on chromium contacts with electrospun pristine PEO nanofibres revealed no evidence of switching behavior, as expected (Figure 5.09). For pristine samples, charging is expected as the dielectric prevents charge from moving from one electrode to the other; it behaves like a capacitor. Figure 5.09 shows an I-V loop ($0V \rightarrow V_{max} \rightarrow 0V$) for pristine PEO devices. The curve demonstrates that the sample is highly resistive as the current is very low (10^{-10} A).

Fibres electrospun containing Au NPs at 10-40% (wt.) also did not demonstrate any resistive switching; the measurements yielded an open circuit in the system. Unlike the case of Al, the presence of Au NPs (for all Au NP loading concentrations) did not have any influence on the resistive switching potential of Cr-based devices. The open circuit could be due to the following reasons:

1. The samples are highly resistive and therefore the dielectric separating both electrodes contains too few Au NPs to form a conduction path. It is important to note that samples electrospun with Au NPs were the same solutions used for the Al-based sample. After some time, Au NPs could potentially aggregate in solution and therefore fresh solutions should be prepared to overcome any

potential changes in solution properties with time. Fibres should be electrospun immediately prior to nanodevice fabrication (and imaged using microscopic analysis, i.e. TEM) in order to determine minor changes in fibre thickness or particle size.

2. The chromium reacts with oxygen at room temperature to form chromium oxide. Chromium can naturally self-passivate. Chromium metal left standing in air is unstable and will oxidize to form a thin layer that acts as a protective coating to prevent the metal against further corrosion. This oxide layer is insulating and the oxidation of chromium was evident by the slight 'darkening' of the contacts, shown in Figure 3.02. The insulating oxide layer could have affected the I-V measurements due to poor probe contact with the electrodes, leaving an open circuit.

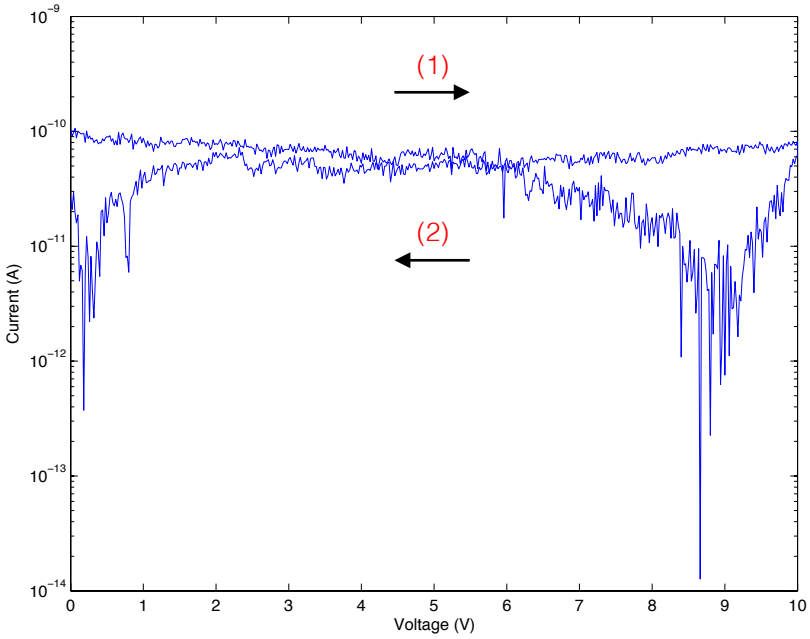

FIGURE 5.09. Typical I-V curve of a pristine PEO device with Cr electrodes.

5.4.1 PLATINUM CONTACTS – I-V MEASUREMENTS

For the final attempt at investigating whether the fibres demonstrated resistive switching, Pt was chosen as the top and bottom contact electrode material. Pt is commonly used in integrated circuit repair and is inert in air, making it an ideal candidate for the test measurements here.

As expected, and consistent with the results from the other electrode materials, pristine PEO devices prepared with Pt contacts demonstrated no evidence of resistive switching (Figure 5.10). Figure 5.10 shows an I-V loop ($0V \rightarrow V_{max} \rightarrow 0V$) for pristine PEO devices. The curve demonstrates that the nanofibre thin film is highly resistive as the current is very low (10^{-10} A) and also without any abrupt jumps in current. The top curve (point '1') shows a gradual increase in current (10^{-10} A to 10^{-9} A), demonstrating charging of the devices due to a build up of charge at the electrode interface. As the voltage is swept back to 0V (point '2'), the device loses some of this charge, shown by the dip in current.

Following this, I-V measurements were performed on devices electrospun with Au NPs to investigate whether resistive switching could be achieved by loading the nanofibres with Au NPs. The device was probed at several points to investigate whether resistive switching was limited to a confined region.

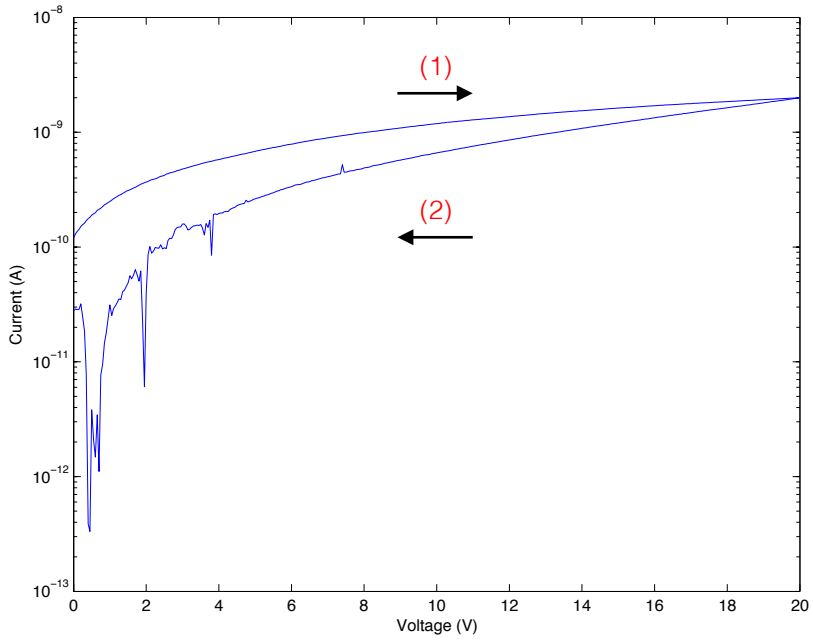

FIGURE 5.10. A typical I-V curve of a pristine PEO device with Pt electrodes.

Devices containing a 30% (wt.) Au NP loading showed resistive switching behaviour. As the potential is increased up to +8V, an abrupt change in current is observed (point '1' in Figure 5.11), a change on four orders of magnitude. This changes the device from a low current (10^{-10} A) OFF state to a high current (10^{-6} A) ON state. The device returns back to the HRS at +12V (point '2' on the curve). An additional switching event is observed also at +14V (point '3'), the device switches to a LRS and returns back to the HRS at +17V (point '4'). This is evidence of multistate resistive switching. Multi-level resistance states are present when there are three or more distinctive states such as this measurement, where we have the HRS, the LRS and the states observed between them, shown between point '3' and '4' on the I-V curve.

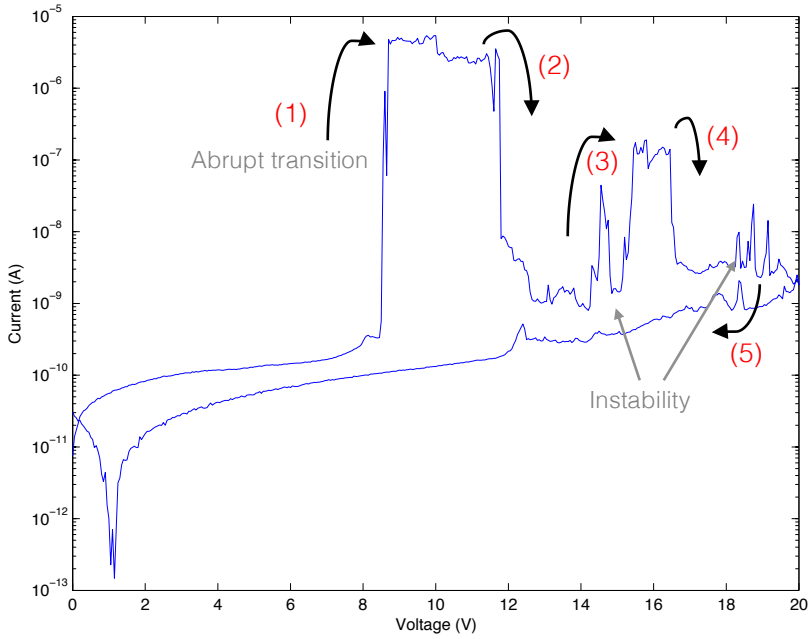

FIGURE 5.11. A typical I-V curve of PEO nanofibres at a 30% (wt.) Au NP loading, showing evidence of multi-level resistance states.

5.4.2 PLATINUM CONTACTS – CONDUCTION MECHANISM RESULTS FOR I-V CURVE SEEN IN FIGURE 5.10

Figure 5.12 provides fits for the three conduction mechanisms described previously for the data presented in Figure 5.11. The data fitting was chosen for the voltage range of 1-7V (top curve in Figure 5.11). It is apparent from the fits in Figure 5.11 that all three curves are highly non-linear although the Poole-Frenkel and TAT model reveal the more interesting data fits. Both fits demonstrate regions of linearity, which require further analysis (below).

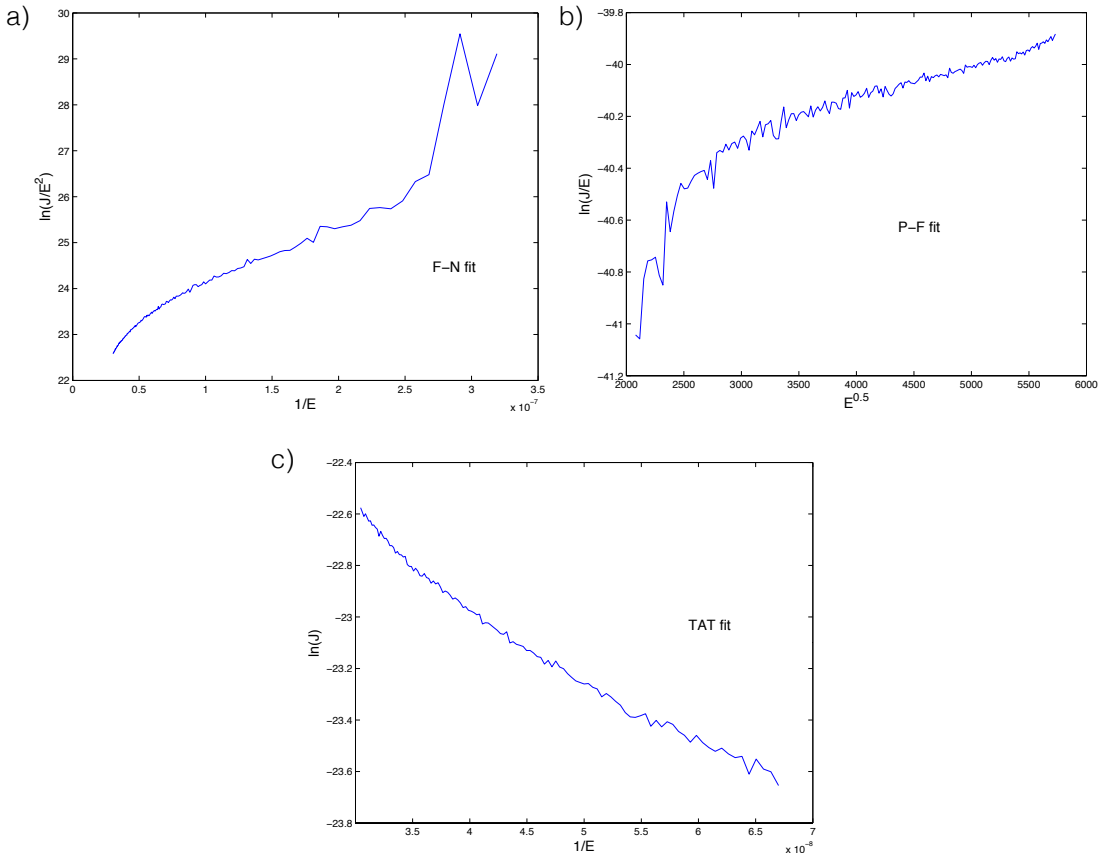

FIGURE 5.12. The data fits for the voltage range of 1-7V. (a) Fowler-Nordheim fit. (b) Poole-Frenkel fit. (c) Trap-assisted Tunnelling fit.

Both the Poole-Frenkel and TAT fits in Figure 5.12 demonstrated a degree of linearity from portions of the curve. A linear region of the curve was chosen both for Poole-Frenkel (Figure 5.12, b) and TAT (Figure 5.12, c) fitting. The data fit can be seen in Figure 5.13 for the Poole-Frenkel model. The data range for $E^{0.5}$ was taken between 2800 and 5000, which corresponds to an applied voltage of 2.3-5.5V.

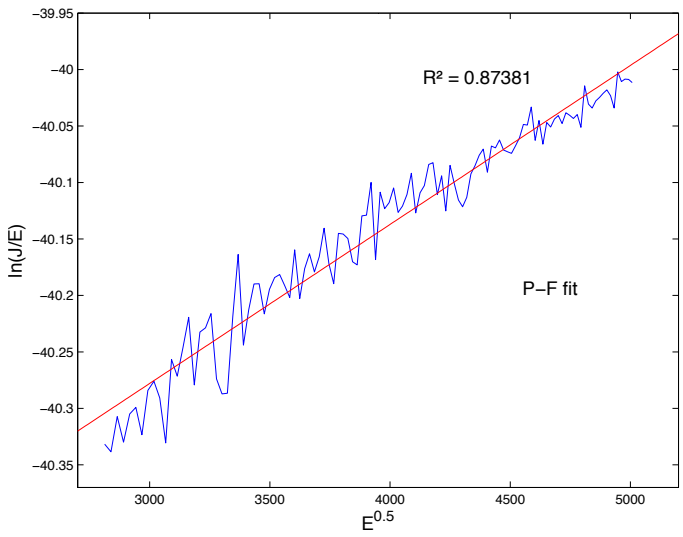

FIGURE 5.13. Data (blue) and fitting line (red). Poole-Frenkel fit for the data range $E^{0.5}$ between 2800 and 5000 (which corresponds to an applied voltage of 2.3-5.5V). Correlation coefficient is 0.87381.

A reasonably good fit is obtained and the correlation coefficient (R^2) is 0.87381.

The TAT fit in Figure 5.12 (c) demonstrated a curve that clearly reveals a higher degree of linearity. Two linear portions of the curve (i.e. different data ranges) were then fitted (Figure 5.14).

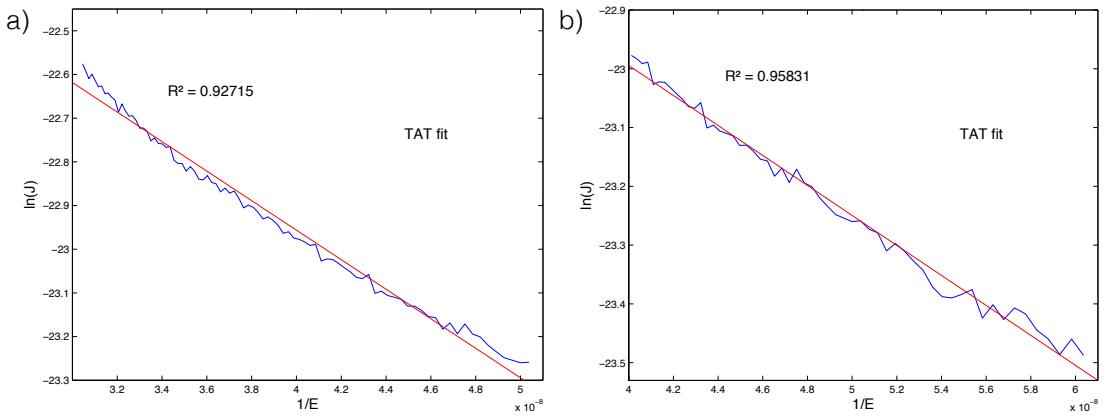

FIGURE 5.14. Data (blue) and fitting line (red). (a) Trap-assisted Tunnelling fit for data range 1/E between 3×10^{-8} – 5×10^{-8} (corresponding to the voltage range 1-4V) Correlation coefficient is 0.92715. (b) Trap-assisted Tunnelling fit for data range 1/E between 4×10^{-8} – 6×10^{-8} (corresponding to the voltage range 2.5-5.5V). Correlation coefficient is 0.95831.

It is clear that the TAT model for the data fits shown in Figure 5.14 provides the best fit of the three possible conduction mechanisms. This suggests the possible existence of defects inside the insulator layer which can introduce traps with the higher electric field and that this potential tunnelling process comprises two or even more steps (through two or more defects). The findings in Figure 5.13 and Figure 5.14 suggest the possible co-existence of two conduction mechanisms.

Both data fits taken from Figure 5.13 and Figure 5.14 have been mapped onto Figure 5.15 to highlight the region of the I-V curve that is dominated by the Poole-Frenkel conduction mechanism, Trap-assisted Tunnelling, and where both conduction mechanisms exist in parallel. The red box (dashed line) in Figure 5.15 reveals that conduction is driven by Poole-Frenkel between 1V and

4.1V. The green box (dashed line) reveals that conduction is driven by Trap-assisted Tunnelling between 2V and 7V and the region between 2V and 4.1V where the highlighted boxes crossover demonstrates the co-existence of both conduction mechanisms (i.e. Poole-Frenkel and Trap-assisted Tunnelling). It is important to note that Trap-assisted Tunnelling is the dominant mechanism at higher electric fields and in the presence of traps (i.e. Au NPs), there is a greater probability for carriers to go through the energy barrier.

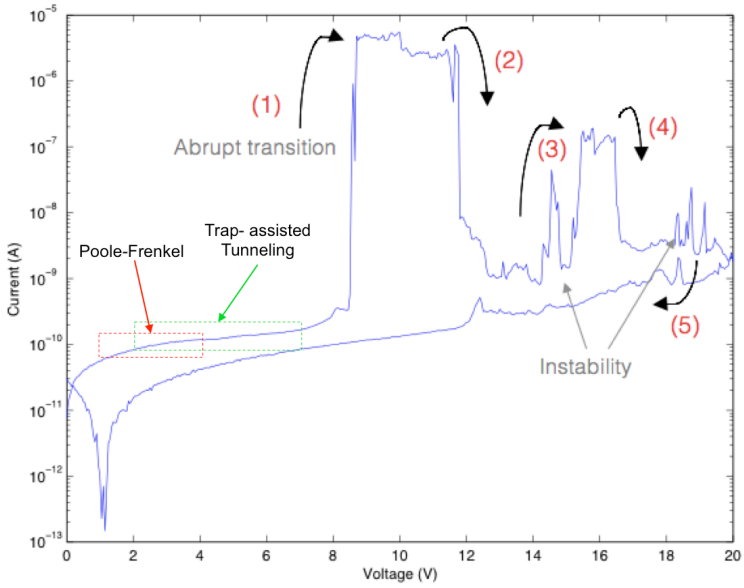

FIGURE 5.15. The original I-V curve of PEO nanofibres at a 30% (wt.) Au NP loading. The curve highlights the regions in which conduction is dominated by Poole-Frenkel (red-dashed box) or Trap-assisted Tunnelling (green-dashed box) in the sample. The region between 2V and 4.1V reveals the co-existence of both conduction mechanisms.

From these results, we can postulate that the encapsulated Au NPs within the polymer matrix take the role of defects. Hence trap-to-trap tunnelling is likely to occur. Carriers can tunnel across these thinner barriers and the probability of conduction across the layer is consequently increased. Figure 5.16 shows a schematic of a possible conduction path connecting the gold nanoparticles across the dielectric.

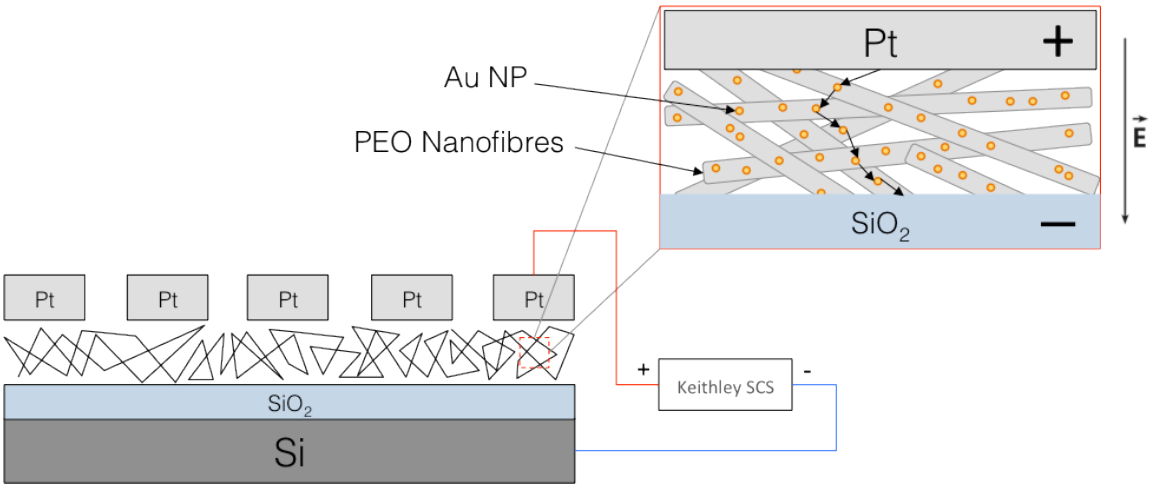

FIGURE 5.16. Schematic of the nanodevice configuration. The magnified box (red border) illustrates tunnelling through the Au NPs.

In a repeat second voltage sweep performed on a different contact electrode, current increases dramatically at +12V (resistance decreases to LRS), (point '1' in Figure 5.17). The device is stable in the ON state up to a potential of +17V. At +17V, the current returns to the original HRS (point '2' on the I-V curve). There is some evidence of an additional switching event at +19.5V although this is not stable and therefore cannot be recognized as a switch to the LRS. This device demonstrates unipolar switching behavior, as the ON and OFF state voltages have the same polarity. Furthermore, there was no evidence of multistate resistive switching as previously seen for the I-V measurements recorded in Figure 5.15.

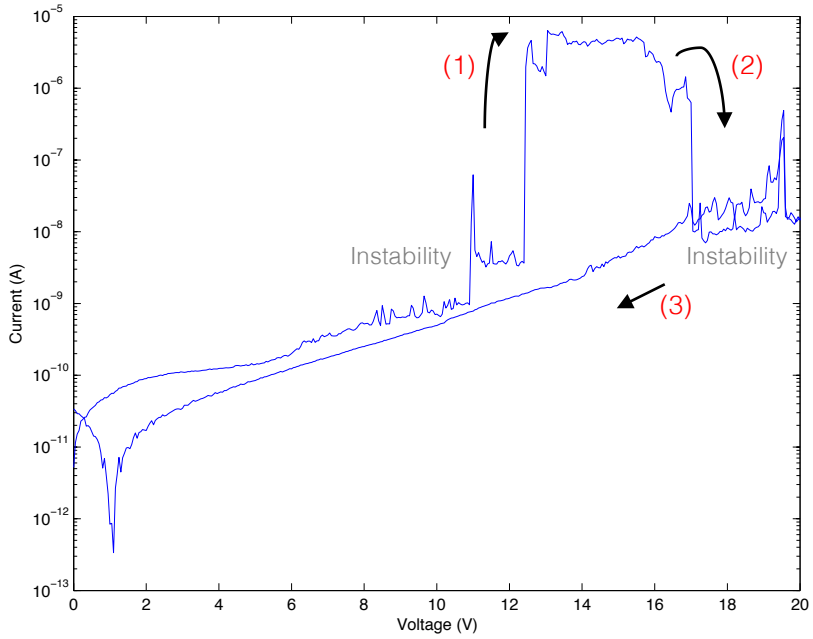

FIGURE 5.17. I-V curve of PEO nanofibres at a 30% (wt.) Au NP loading.

5.4.3 PLATINUM CONTACTS – CONDUCTION MECHANISM RESULTS FOR I-V CURVE SEEN IN FIGURE 5.16

For the resistive switching behaviour observed in Figure 5.17, Figure 5.18 provides fits for all three conduction mechanisms. The data fitting was chosen for the voltage range of 4-11V (bottom curve in Figure 5.17). It is apparent from the fits in Figure 5.17 that all three curves are non-linear. Both Poole-Frenkel and TAT fits were analysed further following the assumption previously that the encapsulated Au NPs within the polymer nanofibres take the role of defects.

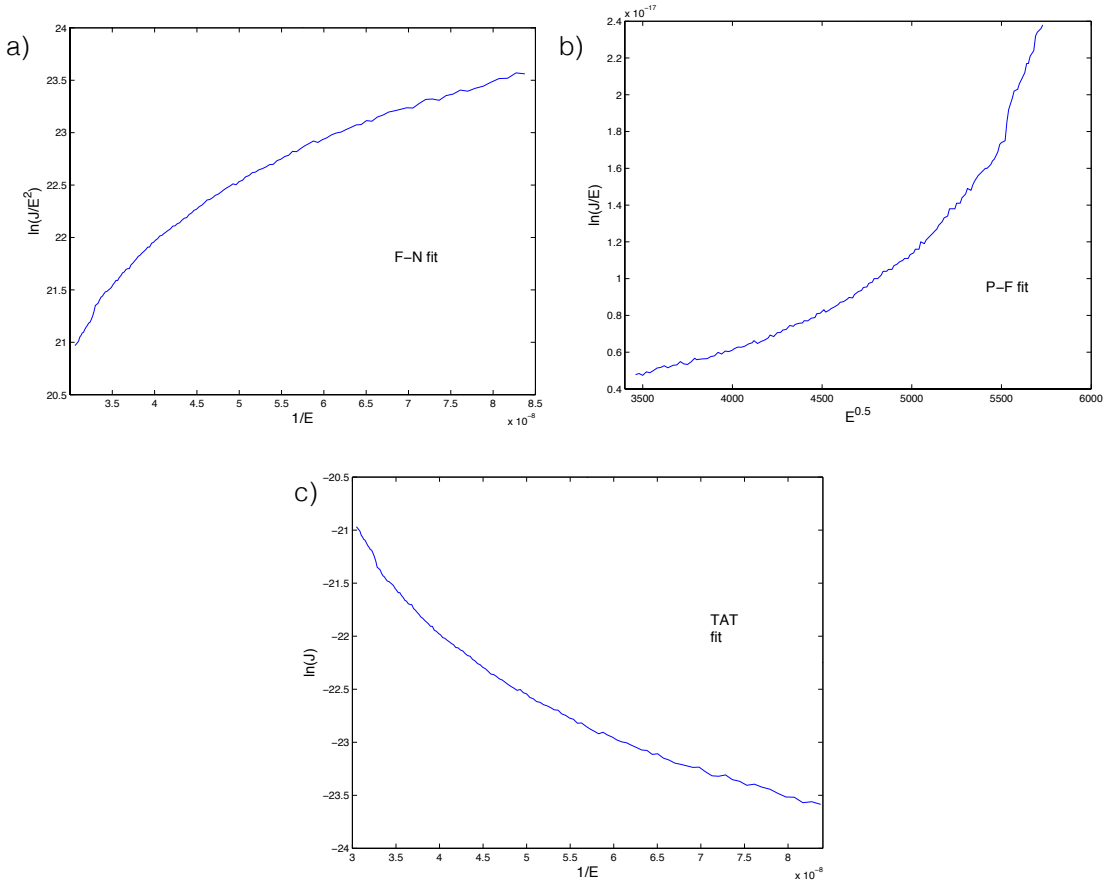

FIGURE 5.18. The data fits for the voltage range of 4-11V.
(a) Fowler-Nordheim fit. (b) Poole-Frenkel fit. (c) Trap-assisted Tunnelling fit.

Data was fitted again to a smaller data range extracted from the Poole-Frenkel model and TAT model shown in Figure 5.18, part (b) and (c), respectively. Once again, the TAT model revealed the best data fit (Figure 5.19, b) with a correlation coefficient (R^2) of 0.97445. The range for 1/E (6×10^{-8} – $8.5\text{x}10^{-8}$) was taken between 8-11V.

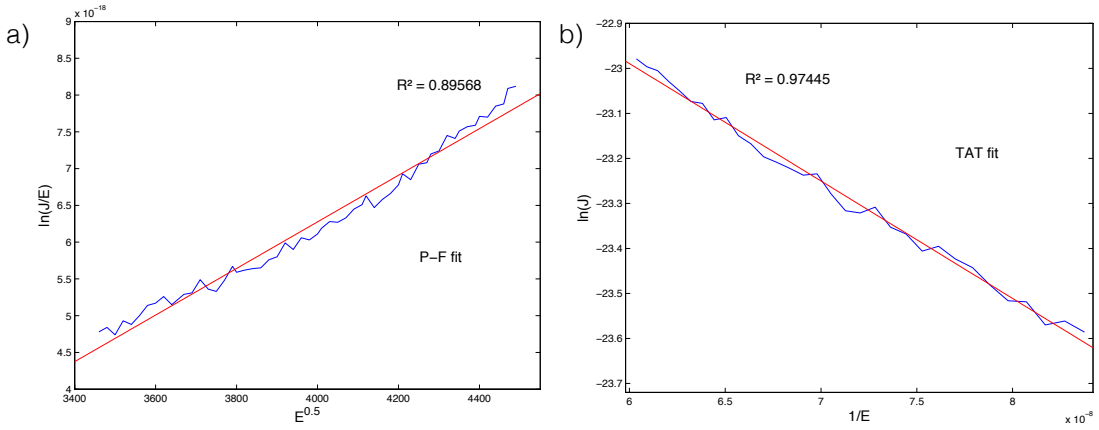

FIGURE 5.19. Data (blue) and fitting line (red). (a) Poole-Frenkel fit for the data range, i.e. $E^{0.5}$ was taken from 3500-4500 (which corresponds to an applied voltage of 4-7V). Correlation coefficient is 0.89568. (b) Trap-assisted Tunnelling fit with correlation coefficient of 0.97445. Data range for 1/E is 6×10^{-8} – $8.5\text{x}10^{-8}$ (which corresponds to an applied voltage of 8-11V).

Once again, both models indicate that current transport in these devices is dominated by Poole-Frenkel conduction and Trap-assisted Tunnelling. Both mechanisms support the presence of a high-density of structural defects (i.e. Au NPs), as previously noted, and this aligns well with the understanding that the fibres have been loaded at a 30% (wt.) concentration. The findings for this second I-V measurement suggest that the conductive pathways through our material are not continuous filaments, but instead a sequence of separate but

neighboring Au NPs, shown earlier in Figure 5.16.

The Poole-Frenkel and TAT data fits in Figure 5.19 have been mapped onto Figure 5.20 to highlight the region of the I-V curve that is dominated by the Poole-Frenkel and the Trap-assisted Tunnelling conduction mechanism. The red box (dashed line) in Figure 5.20 reveals that conduction is driven by Poole-Frenkel between 4V and 6V. The green box (dashed line) reveals that conduction is driven by Trap-assisted Tunnelling between 8V and 11V.

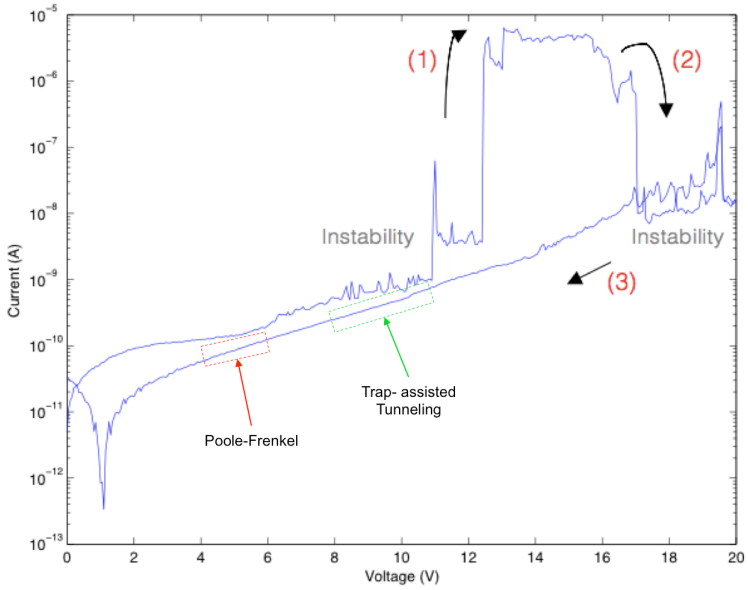

FIGURE 5.20. The original I-V curve of PEO nanofibres at a 30% (wt.) Au NP loading. The curve highlights the regions in which conduction is dominated by Poole-Frenkel (red-dashed box) between 4V and 6V and Trap-assisted Tunnelling (green-dashed box) between 8V and 11V.

In summary, initial resistive switching behaviour has been observed as a result of embedding Au NPs within electrospun PEO nanofibres. It is clear that fibres that were highly doped with Au NPs (30% wt.) exhibited evidence of resistive switching. 10% and 20% (wt.) Au NP samples did not reveal any resistive switching behavior. This could be due to the lower concentration of nanoparticles within the fibres, Figure 4.17.

It is important to note that these attempts are only preliminary and the detailed switching behaviour of these devices has not yet been established, although the initial measurements provide an insight of their potential electronic functionality. A deep understanding of conduction and switching mechanisms is required in order to optimize the device characteristics and also to develop guidelines for scaling, reliability, and reproducibility. Furthermore, research from chemical and electronic viewpoints is needed to elucidate definitively the microscopic origins of conduction and switching.

Finally, the fabrication of devices can strongly determine their electrical behaviour. Electrodes that are inert in air are important to prevent poor probe contact. It is also possible that holes and voids within the electrospun thin film can lead to misleading I-V curves. Metal atoms from the thermal evaporation process may also diffuse between the fibres and migrate under the application of an external electric field and form filaments for charge transport, which could be responsible for the resistive switch [172-180]. This will require further investigation in future studies and could be examined using Scanning Electron Microscopy (SEM) analysis or Atomic Force Microscopy (AFM) to examine the quality and thickness of the electrospun nanofibre film. Furthermore, surface topography measurements will reveal the presence of holes within electrospun films and their uniformity across a large surface area.

Changes in the nanoparticle concentration and electrode material are only a couple of the parameters varied in this study although a plethora of factors can influence the resistive switching potential of these devices. Factors such as the size of the nanoparticles and their concentration, thickness of the fibres and the film, polymer concentration and molecular weight, solution conductivity and the size of the electrodes. Furthermore, refinements in electrospinning fibres with a uniform distribution of Au NPs is important for control and reproducibility when assessing electronic functionality. Although advantages such as low cost fabrication are possible through electrospinning, further investigation is required into the materials' stability and temperature influence, which often plague polymer/nanoparticle devices.

If a reproducible switching protocol can be established coupled with cost-effective electrospinning fabrication technology, these nanocomposite-based MIM devices would be of immediate interest in information technology where devices with high-speed switching and processing are required. It is possible that the attempts made in this study can open doors for investigating new materials to manufacture novel electronic nanodevices and will become a major area of research in the future development of applied device implementation.

6. RESULTS

ELECTROSPRAY SYNTHESIS OF TIPS MICROSPHERES

6.1 CONDUCTIVITY MEASUREMENTS

Conductivity measurements were taken of combinations of DMC, Formic Acid and DI water. These measurements were taken to determine the highest volume concentration of DMC that could be present in the solution whilst retaining a sufficient solvent conductivity to be electrosprayed at the lowest flow rate (i.e. within the cone-jet stability regime). Table 6.1 below lists the conductivities measured using the formulations listed in the table. The aim here is to demonstrate that using process control parameters and solution properties, it is possible to manufacture particles down to 5μm, whilst retaining the bulk properties of the solution necessary to manufacture highly porous particles using the novel TIPS process.

Solvent Formulation	Ratio (Volume %)	Conductivity σ (μS/m)	Calculated Diameter (μm)
DMC/Formic Acid/H_2O	99 : 0.5 : 0.5	6.26	4.74
DMC/Formic Acid/H_2O	98 : 1 : 1	7.87	4.39
DMC/Formic Acid/H_2O	97 : 1.5 : 1.5	10.48	3.99
DMC/Formic Acid/H_2O	96 : 2 : 2	13.55	3.67
DMC/Formic Acid/H_2O	95 : 2.5 : 2.5	22.50	3.09
DMC/Formic Acid/H_2O	94 : 3 : 3	46.08	2.44

TABLE 6.1. Summary of the solvent formulations used to estimate (calculate) the size of electrosprayed particles using Equation 3 (Chapter 3).

A scaling relation (Equation 3, Chapter 3) was used to select the parameters required to manufacture particles down to approximately 10±5μm in diameter. Flow rates and liquid conductivities were varied to prepare TIPS microspheres of different size. The addition of formic acid and water was used to enhance the electrical conductivity of the ES liquid. Calculated diameters with increasing solution conductivity are plotted in Figure 6.01 and reveal that particle diameters ≤5μm are possible at flow rates of 1 mL/hr. Table 6.2 below reveals the experiments conducted to determine the lowest possible flow rate

that could be used with the solvent formulation (DMC (99):Formic Acid (0.5):DI Water (0.5)) whilst retaining a stable cone-jet mode operation and also ensuring all the current emitted at the emitter capillary was preserved (i.e. 100% collection).

Flow Rate, Q (mL/hr)	Cone-Jet Mode (Yes/No)	Emitted Current, I_{EC} (nA)	Collected Current, I_{CC} (nA)
0.1	No, Dripping	11	0
0.2	No, Dripping	13	0
0.3	No, Dripping	14	3
0.4	No, Dripping	19	8
0.5	No, Dripping	22	12
0.6	No, Dripping	23	13
0.7	No, Oscillating	24	14
0.8	No, Oscillating	24	14
0.9	Yes, Oscillating	25	19
1.0	Yes, Cone-Jet	27	27

TABLE 6.2. Summary of the flow rates used to determine the lowest possible flow rate at which a cone-jet mode could be preserved.

The findings in Table 6.2 reveal that most commonly flow rates below 0.7 mL/hr demonstrated dripping modes. The ‘spitting’ spray was the common feature

used to distinguish the dripping mode from any other mode. At 0.7 – 0.9 mL/hr, an oscillating jet was observed. The oscillating jet is a spray that is continuously pulsating in and out of the needle emitter. Retraction of the solution back into the emitter was used to characterize the oscillating jet which was also off-axis and unstable. Although at 0.9 mL/hr a cone-jet mode was visible, the jet was unstable for short intervals and also the emitted current was not entirely collected (i.e. 76% efficient). 1 mL/hr was the most efficient flow rate, with 100% efficiency, operating in a stable cone-jet mode.

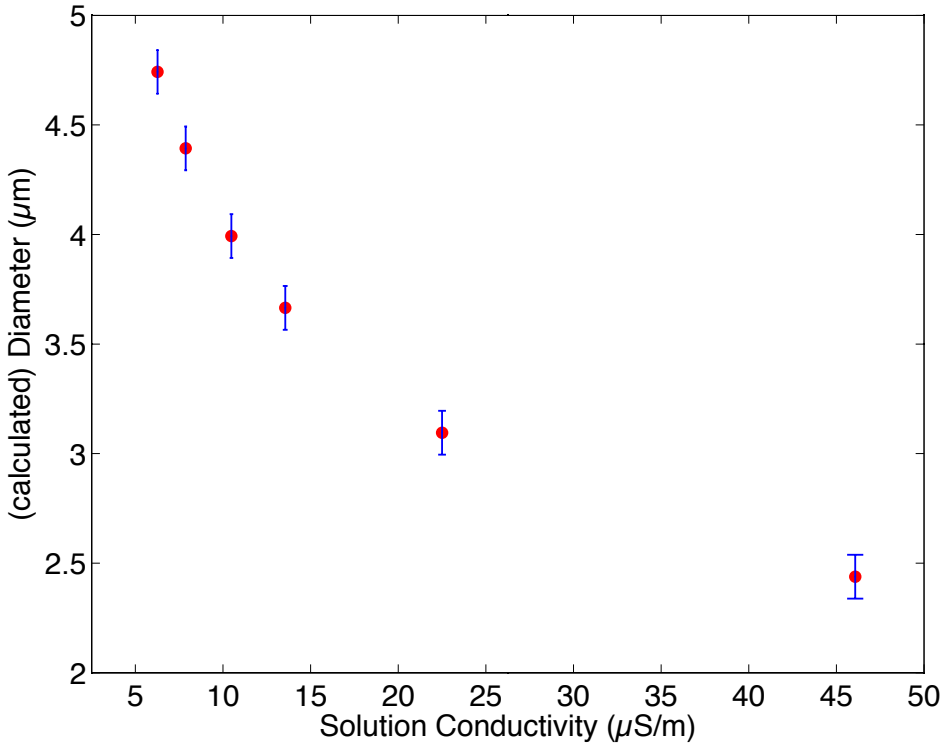

FIGURE 6.01. Dependence of the diameter of electrosprayed droplets on solution conductivity (calculated using Equation 3, Chapter 3). A flow rate of 1 mL/hr was used to calculate the diameters shown in the graph.

Particles were experimentally synthesized at 1 mL/hr to examine whether the calculated diameters of particles aligned with the diameters of particles prepared experimentally. The calculated diameter at 1 mL/hr was 4.74μm and the mean experimental diameter was 10.73μm, fitting well within the aim of manufacturing particles within the limit, 10±5μm in diameter.

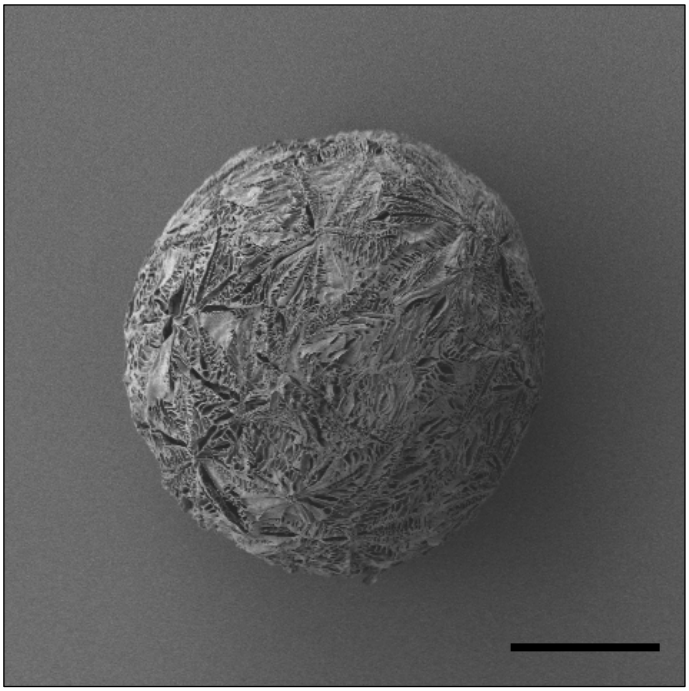

FIGURE 6.02. SEM image of an ES TIPS particle prepared at 1 mL/hr. (scale bar: 5μm)

6.2 FLOW RATE

Flow rate was changed to produce particles of six different sizes. Table 6.3 shows the list of process parameters used to manufacture particles at the flow rates listed, including the voltages applied at each electrode and the currents measured to determine losses, i.e. flyback and collected current at the extractor electrode and in the liquid nitrogen collection bath, respectively.

Flow Rate, Q (mL/hr)	HVPSU1 (kV)	HVPSU2 (kV)	Emitted Current, I_{EC} (nA)	Flyback Current, I_{FB} (nA)	Collected Current, I_{CC} (nA)
1	10.2	7.0	18	0	18
2	10.7	7.2	20	2	18
5	11.0	8.1	26	2	24
10	11.5	8.3	31	3	28
20	12.3	8.8	38	4	34
30	12.8	9.2	43	2	41

TABLE 6.3. Summary of the flow rates used to manufacture particles along with the parameters used to control the preservation of a stable cone-jet mode. The high voltage power supplies (HVPSU) have been indicated along with their number (HVPSU1 is power connected to the emitter, HVPSU2 is power connected to the extractor plate).

Figure 6.03 demonstrates a monotonically increasing trend for diameter against flow rate for PLGA microspheres prepared between 1-30 mL/hr. This

also demonstrates that a stable operation of the cone-jet mode was preserved (specifically between 1-15 mL/hr), as the flow rate can only be varied within a certain range within the ES stability domain. The addition of small amounts of dopants (i.e. formic acid and DI water) to the solvent enabled particles to be sprayed across a range of flow rates while preserving other physical properties, such as the bulk solvent of DMC (at 99%). Ensuring the bulk preservation of DMC in the solvent was critical to synthesizing particles as prepared previously [113].

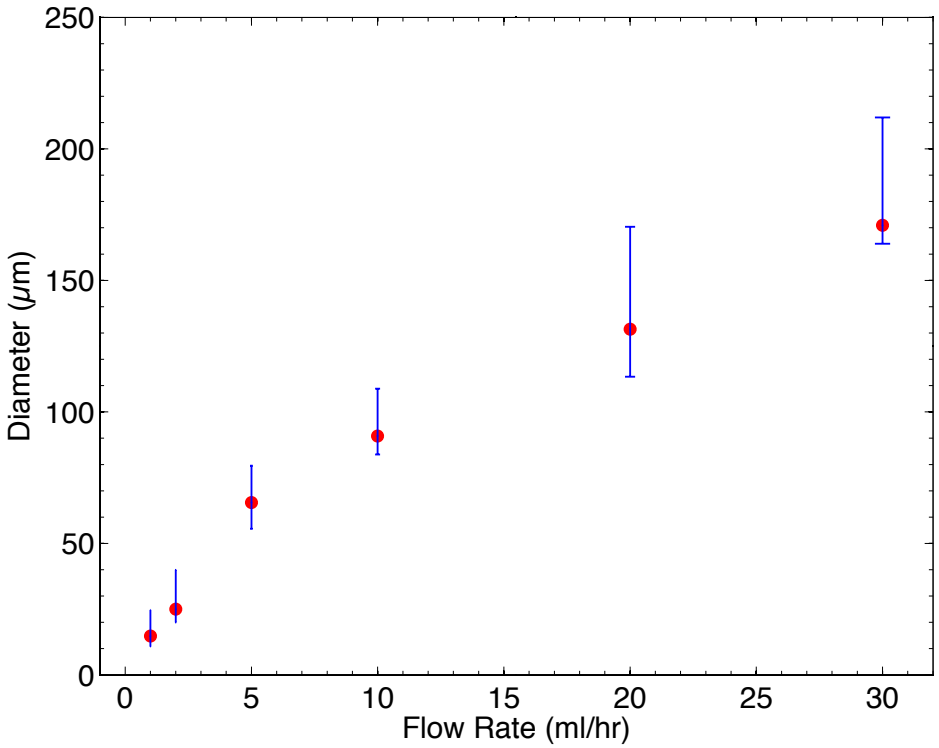

FIGURE 6.03. Measured diameter of PLGA TIPS microspheres as a function of flow rate.

It must also be noted that Figure 6.03 demonstrates the standard deviations in diameter for microspheres electrosprayed at larger flow rates (i.e. 20 mL/hr and 30 mL/hr) were greater than those sprayed at low flow rates. Overall, evidence of maintaining approximate control over the size of the novel TIPS microspheres can be provided by alterations in solution conductivity and liquid flow rate, as the droplet diameter increases monotonically with both parameters. Figure 6.04(i-vi) shows the respective SEM images for ES PLGA TIPS microspheres prepared at the six flow rates listed in Table 6.3.

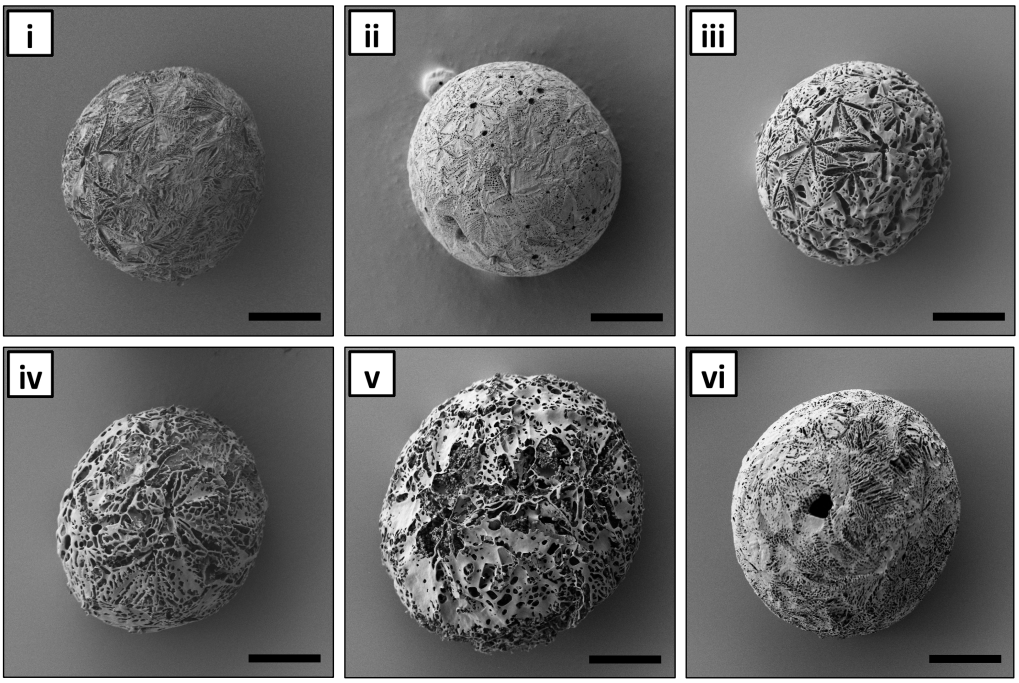

FIGURE 6.04. SEM images revealing representative particle morphology at flow rates: (i) 1 mL/hr (scale bar: 5μm) (ii) 2 mL/hr (scale bar: 10μm) (iii) 5 mL/hr (scale bar: 20μm) (iv) 10 mL/hr (scale bar: 30μm) (v) 20 mL/hr (scale bar: 40μm) (vi) 30 mL/hr (scale bar: 50μm).

6.3 DISTANCE

Distances between the extractor electrode and LN_2 free surface (i.e. the spray region) were varied in order to examine if the distance determined the morphology of the electrosprayed TIPS particles. Throughout all experiments, the spray region was kept constant at 40mm, an optimized distance to keep the field strength sufficiently high yet prevent droplet freezing at the capillary exit ensuring the nozzle temperature remained above the Leidenfrost temperature. Additionally, at 40mm, this particle transport distance held above the nitrogen vapour layer limited air viscous drag, spray drift and space charge effects. Although this distance is key to ensuring the consistent manufacture of TIPS particles as shown in Figure 6.04, it is worth examining whether this distance had significant effects on the size and morphology of the PLGA particles. Table 6.4 shows the three particles distances chosen for this study.

Flow Rate, Q (mL/hr)	Distance between Extractor and LN_2 Free Surface (mm)	HVPSU1 (kV)	HVPSU2 (kV)	Emitted Current, I_{EC} (nA)	Flyback Current, I_{FB} (nA)	Collected Current, I_{CC} (nA)
1	40	10.2	7.0	18	0	18
1	80	12.8	9.4	18	7-9	9
1	120	15.5	12.1	16	10-12	3

TABLE 6.4. Summary of the distances used to manufacture particles along with the parameters used to control the preservation of a stable cone-jet mode. The data documents the collected current to determine the process efficiency.

In summary, from Table 6.4, there is a clear trend that shows that as the distance between the extractor plate and LN_2 free surface increases, the collection efficiency of the process decreases, collectively derived from measurements of emitted current, flyback and collected current. At a distance of 40mm, the efficiency of the process is a 100%, however at 80mm and 120mm, the collection efficiency decreases down to 50% and 18.75%, respectively. The loss in particles is specifically associated with flyback, and spray drift effects. Spray drift was evident as there was a greater presence of particles on the edge of the collection bath and subsequently on the apparatus enclosing the experiment. At 40mm, spray drift was limited and the second electric field ensured particles were directed into the LN_2 medium. The second electric field also accelerated particles into the medium to help overcome viscous drag. Distances held below 40mm, froze the stainless steel needle emitter and also the liquid meniscus at the capillary tip. Freezing of the PLGA solution at distances <40mm caused the build up of a large droplet at the emitter tip, which would eventually detach and drop into the collection bath. This process would generally disturb the flow of the spray and cause wastage of material, therefore it was important to operate at distances that would keep the nozzle temperature above the Leidenfrost point, whereby an insulating vapor layer would surround the needle and disrupt the emission of a spray.

Figure 6.05 shows the respective SEM images captured at the distances listed in Table 6.4. The SEM micrographs were captured to examine if the spray region distance altered the morphology and size of particles. Interestingly the Leidenfrost effect was observed on the surface of the LN_2 medium at 120mm distance. This is due to the repulsive force of the insulating vapor layer causing the polymer droplet to hover over the surface, rather than making physical contact with it. Particles were commonly seen to skitter over the surface at this distance and this is likely to occur as particles have lost their accelerating

energy to penetrate the LN_2 surface.

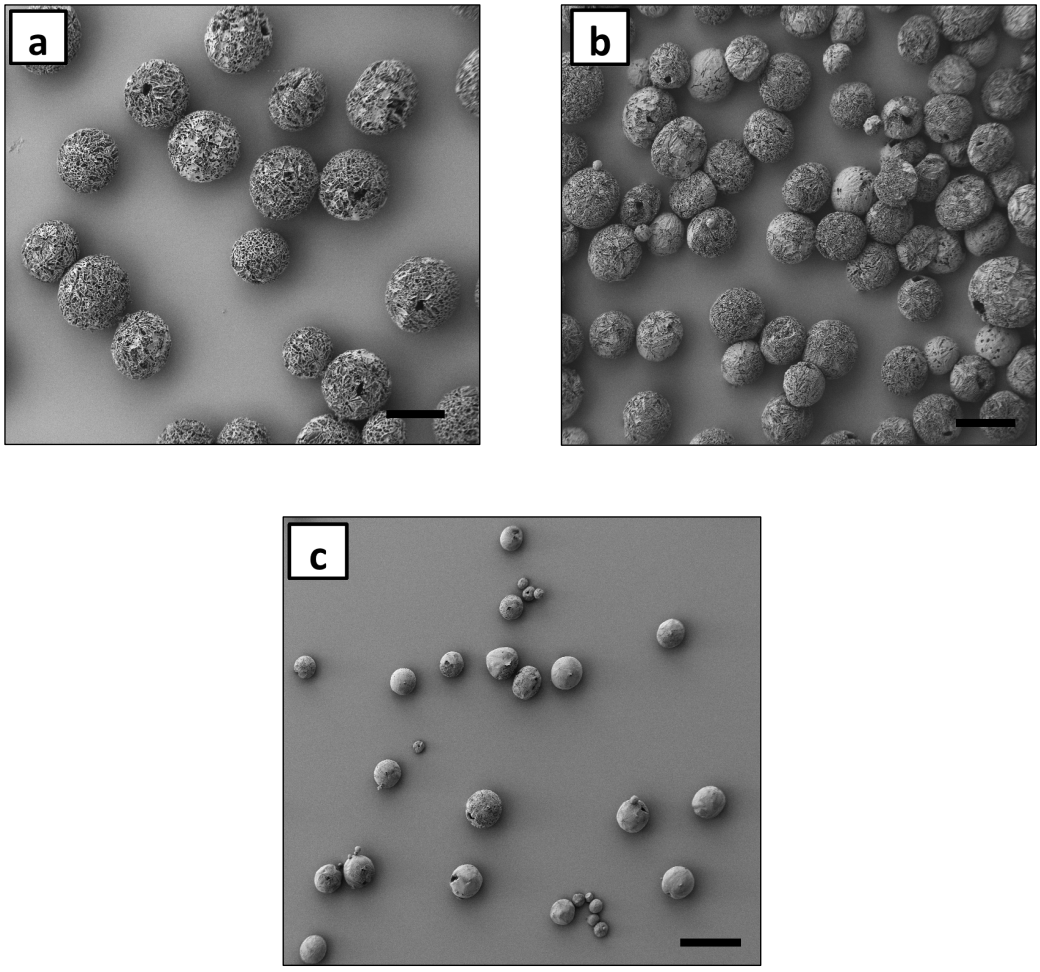

FIGURE 6.05. SEM images of particles electrosprayed at (a) 40mm (scale bar: 10μm), (b) 80mm (scale bar: 10μm) and (c) 120mm (scale bar: 10μm).

The SEM images most importantly reveal that the distance had no major effects on the morphology of particles. However, the spray region distance primarily affected the collection efficiency of particles. Understanding the overall effect

of distance and its effect on efficiency is important for industrial-scale manufacture and this experiment found that in conclusion, the optimal spray region distance was 40mm at which all particles emitted were collected, yet retained their TIPS particle morphology and structure. Particles electrosprayed specifically at the 120mm distance did however reveal the presence of smaller satellite particles under SEM and also particles didn't appear to have the characteristic TIPS signature usually exhibiting an external cavity (i.e. opening) on the particle surface. The difference in appearance is mostly likely due to greater solvent evaporation effects at larger distances. As the distance between extractor and LN_2 free surface is increased, the bulk DMC solvent present in the particle is likely to undergo greater evaporation due to solvent volatility and the longer time of flight the particle has in air (at room temperature) than particles electrosprayed at 40mm. With greater solvent evaporation, the particle will contain less solvent post-ES and therefore will not undergo the same degree of sublimation as particles that contain a greater volume of solvent after freezing in LN_2 and subsequently lyophilisation.

6.4 PARTICLE SIZE AND SHAPE ANALYSIS

To assess particle shape preservation, size and shape analysis was performed on two different microsphere samples prepared using flow rates of 1 mL/hr and 15 mL/hr using an extensive screening process to yield quantifiable size and shape information for thousands of particles. Shape and size affect the bulk behaviour of particles (in powders) and, more importantly, can determine biomedical application. In this case, the two flow rates chosen demonstrate control of the electrospray technique to manufacture TIPS microspheres of different sizes by simple variation of one processing parameter, and additionally represent the variation in particle properties when prepared using ES atomization. Both samples were successfully dispersed with the sample dispersion unit and data were interpreted using the in-built Morphologi software.

Figure 6.06(a) shows the number distributions of Circular Equivalent Diameter (CED). Both samples contain a monodisperse population of discrete particles with no overlapping, and complete isolation from neighboring particles. There is an absence of fine particles and grains, as a distinct peak is visible for both smaller and larger particles. The smaller particles have a CED mean of 16.77μm, while that of larger particles is 122.91μm. Particles prepared at 15 mL/hr also show less polydispersity in terms of size distribution. Polydispersity of particle size may introduce variability in the release rates and shape of the microsphere can also affect particle interaction with macrophages [17, 181].

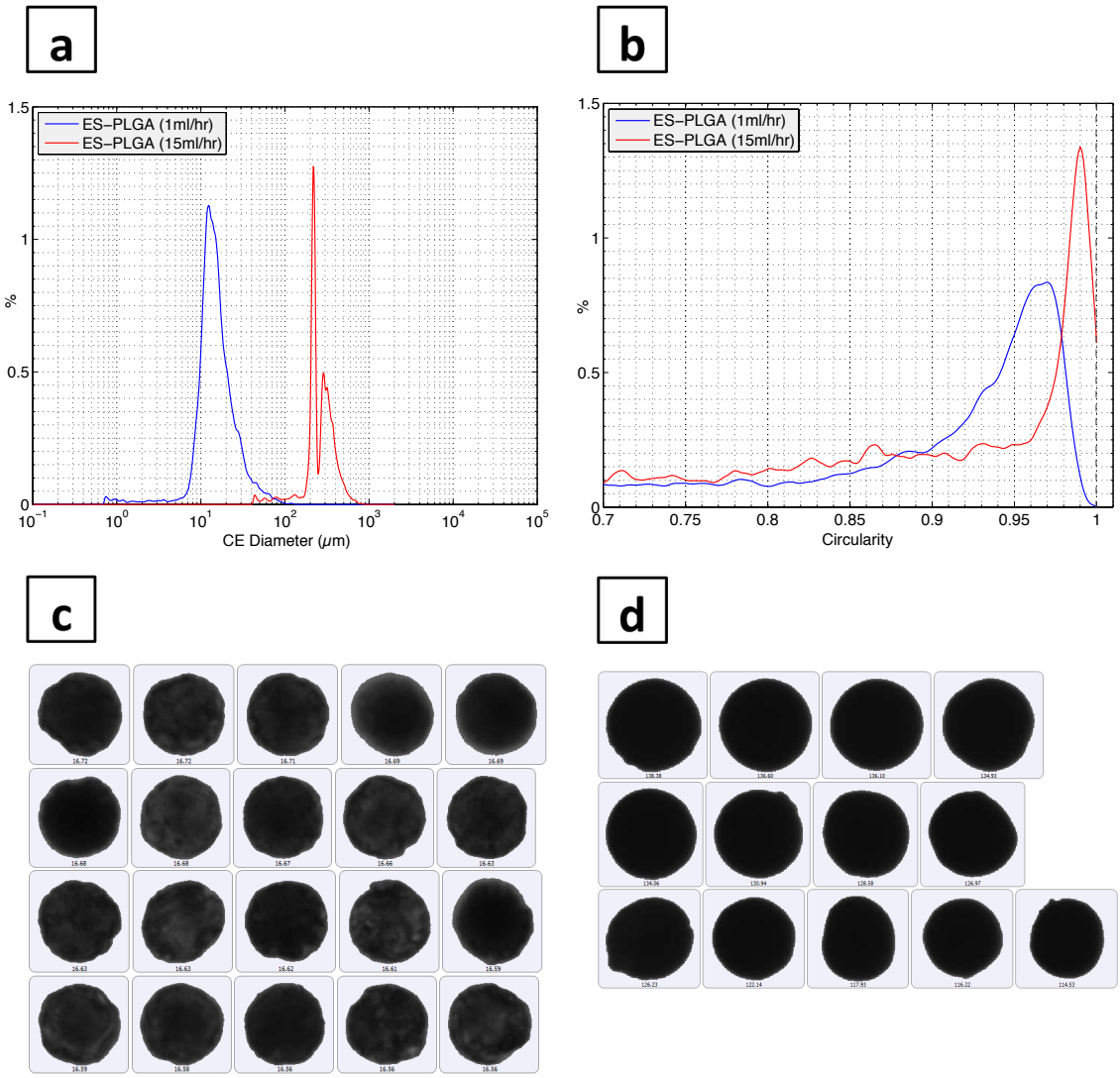

FIGURE 6.06. Distribution plots for (a) Circular Equivalent Diameter and (b) High Sensitivity Circularity for TIPS microspheres. Particles synthesized at 1 mL/hr are indicated with blue lines and particles synthesized at 15 mL/hr are shown in red. Particle images for (c) CED mean of 16.77μm and HSC mean 0.774 synthesized at 1 mL/hr and (d) CED mean of 122.91μm and HSC mean 0.787 synthesized at 15 mL/hr. (CED in μm indicated under each particle).

Figure 6.06(b) shows the High Sensitivity Circularity (HSC) distributions for the two samples screened, indicating that PLGA samples prepared at 15 mL/hr are fractionally more circular than those prepared at 1 mL/hr. As summarized in Table 6.5, there was a larger sample size screened at 1 mL/hr as the sample contained smaller-sized particles and the ability of the instrument to disperse particles equidistantly without neighbouring contact. Due to the larger (mean) size of particles prepared at 15 mL/hr, the number of particles screened was fewer to avoid overlapping of microspheres. Larger particles occupy a greater surface area and therefore avoiding contact with neighbouring particles is key for analysis as particle-particle contact could lead to misinterpretation of a circular object using the instrument software and therefore invalidate the data.

Property	ES PLGA (at 1 mL/hr)	ES PLGA (at 15 mL/hr)
Particles Screened	11349	6267
CED (μm) Mean	16.77	122.91
HSC Mean	0.774	0.787

TABLE 6.5. Summary of size and shape characteristics for particles prepared at 1 mL/hr and 15 mL/hr.

In summary, the findings of size and shape analysis have demonstrated that particles electrosprayed at small (1 mL/hr) and large (15 mL/hr) flow rates are not subject to changes in shape and that a spherical morphology can be retained using electrosprays. Adjusting flow rates to synthesize a range of dye-loaded particles of varying size will form the dissolution tests (in Chapter 7).

6.5 CONFOCAL RAMAN MICROSCOPY

The intensity of the Raman peak with centre wavenumber 1,763 cm^{-1} was mapped at different depths for both electrosprayed PLGA particles and PLGA granules; the peak corresponds to a stretch of the carbonyl moiety. In order to identify changes in chemical composition across particle types, images were obtained by mapping the peak intensity as a function of XY position. Raman spectra were collected with a five-image z-stack of horizontal images, the focal position being adjusted using a piezo scanner. Each image slice through the particle remained consistently 12.5μm below the other and demonstrated that PLGA exhibits little variation in structure as a function of position in either structural form (Figure 6.07). The one significant variation, around 440 cm^{-1}, came from the silicon substrate on which the freeze-dried PLGA TIPS particles were mounted. Lighter regions of the image signify regions of high peak intensity in that section of the particle; darker regions signify lower peak intensity.

Overall, spectra revealed that as anticipated, electrosprayed PLGA microspheres demonstrated the same spectra as PLGA prior to electrospray processing. The chemical composition of the material was unaffected by the electrospray technique and electrical charging of the polymer solution did not influence the physicochemical properties of the polymer. This was demonstrated by comparing the spectra (in Figure 6.07) of the end product with the original polymer granules as received from the manufacturer. The results also reveal that the solvent formulation used in electrospraying has not affected the composition of the material, and verify the complete sublimation of solvent from the particles post-lyophilisation. Total dehydration of solvents from the particle is an important finding for their long-term storage and the effective delivery of drugs and to avoid particles collapsing at room temperature.

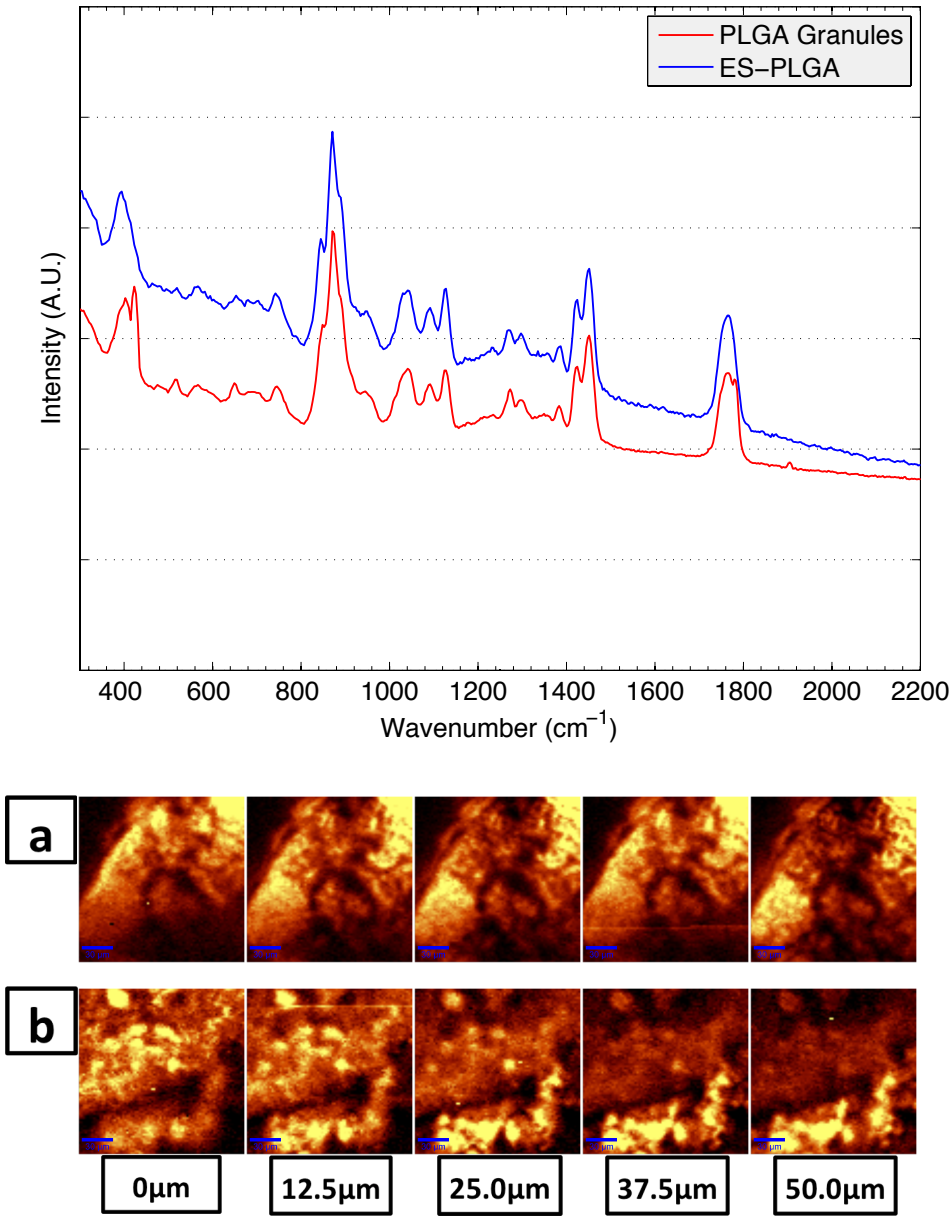

FIGURE 6.07. Raman spectra for ES PLGA TIPS microspheres (blue) and PLGA granules (red), and corresponding 50µm five-image z-stack for (a) PLGA granules and (b) ES-PLGA. Scale bar 30µm. (Depth indicated below particle).

6.6 MERCURY INTRUSION POROSIMETRY – FOCUSED ION BEAM

The porosity of the PLGA TIPS microspheres was investigated for three particle sizes. Results revealed a clear dependence of particle size on void fraction within particles, as seen in Table 6.6. Data were verified by SEM image analysis that provided information from three-dimensional cuts of the porous structure using a Focused Ion Beam (FIB). Figure 6.08 illustrates how porosity decreases with increasing particle size. This finding suggests that smaller particles would have a shorter (i.e. quicker) release profile than larger particles, as water can penetrate the pores more easily.

Property	Small (≈10–20μm)	Medium (≈100–150μm)	Large (≈200–250μm)
Total Intrusion Volume (mL g^{-1})	14.304	2.783	7.461
Total Pore Area (m^2 g^{-1})	64.786	0.05	0.135
Apparent (skeletal) Density (g mL^{-1})	1.1746	0.2569	0.0843
Porosity (%)	94.38	51.68	38.62

TABLE 6.6. Porosimetry measurements for three microspheres of differing sizes, categorized into 'Small', 'Medium' and 'Large'. Measurements of porosity have been highlighted in red colour.

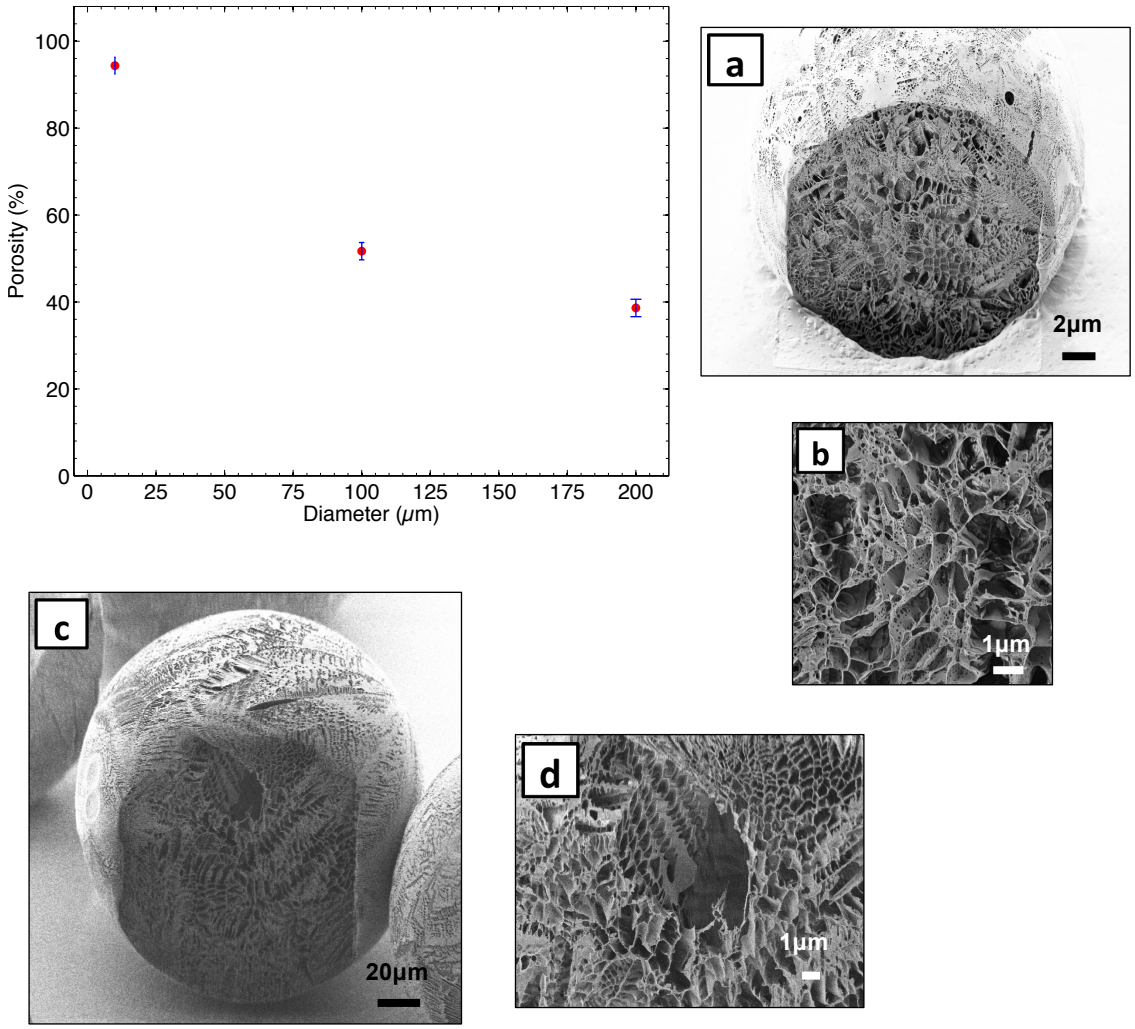

FIGURE 6.08. Porosity as a function size for PLGA TIPS microspheres. (a) FIB three-dimensional cut of a small particle and (b) the internal pore network. (c) Large particle cut and (d) its internal pore network.

Each composition exhibited a smooth surface skin, peppered with pores often arranged in a chevron-like pattern, typical of TIPS microspheres, along with a

large internal cavity [113]. FIB images exposed interconnected porosity with open channels, ideal for the effective transport of release medium, both on the surface of spheres and internally. Unlike characteristic TIPS microspheres synthesized from PLGA (dissolved in only DMC solvent), the internal structure did not contain the channel-like radial tubular macropores reported previously [113, 115]. In this case, image analysis exposed a structure with a continuous distribution of voids within the microspheres and highly anisotropic morphology. During TIPS, the solution is separated into a polymer-rich phase and a polymer-lean phase due to crystallization of the solvent when the temperature of the polymer solution is lower than the freezing point of the solvent. The polymer is expelled from the crystallization front to form a continuous polymer-rich phase. The solvent sublimes to leave pores. This is characteristic of a TIPS particle. The structure observed is likely to have resulted from a slightly adjusted solvent formulation for optimal cone-jet ES and/or a different polymer concentration similar to that previously described for emulsion TIPS microspheres [113].

It should, however, be noted that these porosimetry results represent only one method of porosity measurements and are strictly limited to the Washburn equation (Equation 4), which is based on the cylindrical pore assumption and may not hold for all microspheres. The Total Intrusion Volume (TIV) is measured directly during the intrusion process. All other quantities are calculated using the TIV and the Washburn equation. Further control over porosity could be enabled by varying the polymer concentration, polymer composition and solvent formulation.

6.7 THERMOGRAVIMETRY

Measurements of mass changes (Δm) due to evaporation, decomposition and interaction with the atmosphere were monitored against temperature in an inert atmosphere. In order to observe the best comparison, the heating rate and sample mass were kept the same, except that in this case, degradation was compared for a mix of both electrosprayed medium (~100–150μm) and large-sized (~200–250μm) PLGA TIPS microspheres and PLGA granules (as received in original form). Due to the low throughput of the process, insufficient masses were produced for the small-sized particles to be measured and therefore comparison was made between particles in the size range ~100–250μm and the granular sample.

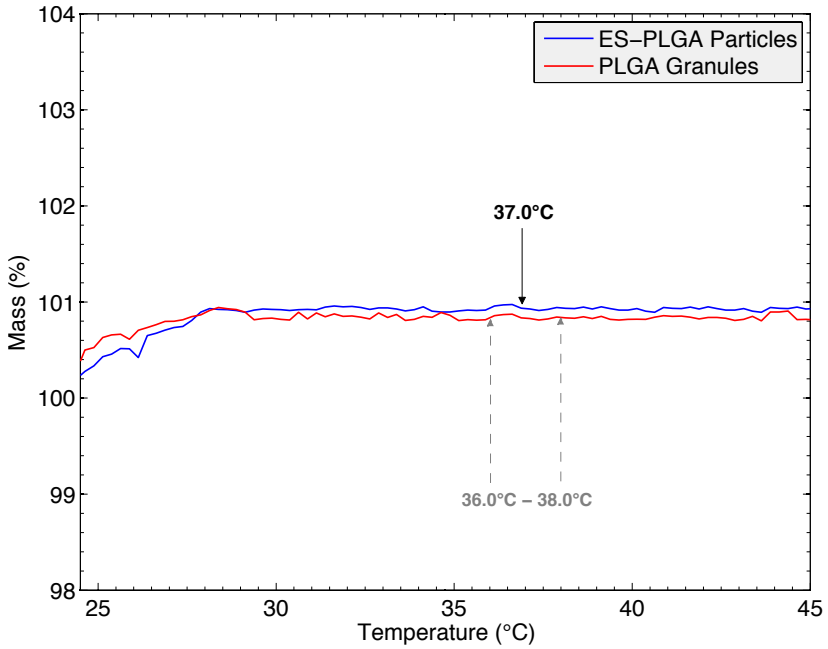

FIGURE 6.09. TG Thermogram of the ES PLGA TIPS microspheres (blue) and PLGA granules (red). No mass loss is observed at 37°C.

Thermogravimetric analysis of the spherical PLGA TIPS microspheres revealed no physical or chemical changes over the narrow temperature range of biological interest (Figure 6.09). Although the TGA instrument is commonly known to suffer from weight stabilization issues, these were noticed before measuring the sample and may have occurred during the measurement however measurements were repeated three times and the mean thermogram displayed.

In summary, PLGA TIPS microspheres have been electrosprayed and their physical and physicochemical properties have been assessed. The electrospray (when coupled with freeze drying) does not alter the physicochemical properties of the polymer microparticles, an important factor when preparing spherical particles for drug delivery. The particles were prepared using a variation of flow rates and distances to determine optimum parameters for electrospraying PLGA TIPS particles down to approximately 10±5μm in diameter and a scaling relation was used to estimate the particle diameters prior to manufacture. The scaling relation was used as a guide to establish fundamental criteria that allow for the generation of particles of a prescribed size, morphology and consistency. Importantly, this is the first time that PLGA TIPS microspheres have been successfully prepared using the ES technique and also the first time particle shape analysis and porosimetry measurements have been performed on electrosprayed particles.

7. RESULTS

DISSOLUTION TEST

7.1 CONDUCTIVITY MEASUREMENTS

Conductivity measurements were taken of solutions of PLGA (at 5% w/v.) containing Rhodamine 6G at various concentrations. The concentrations of R6G were 0.5ppm, 1ppm, 10ppm 50ppm, 100ppm and 150ppm. This range would also help determine the concentration of dye that would ensure the conductivity of the solution was not considerably affected. Therefore the dye concentration was selected based on the conductivity of the solution, ensuring this was as close as possible to the concentration of the solvent formulation, i.e. 6.26 μS/m. This would also ensure the highest concentration of dye that could be present in the solution was selected whilst retaining a sufficient solvent conductivity to be electrosprayed at the lowest flow rate (i.e. within the cone-jet stability regime). Furthermore, having the highest concentration of dye in the solution would allow the detection of fluorescence emission taken under UV-Vis measurements. Table 7.1 below lists the solution conductivities measured using the dye concentrations listed in the table.

PLGA Solution Concentration (w/v)	R6G Concentration (ppm)	Conductivity σ (μS/m)
5%	0.5	8.18
5%	1	11.87
5%	10	15.54
5%	50	54.93
5%	100	94.74
5%	150	136.86

TABLE 7.1. Summary of the solution conductivities measured for three different dye concentrations in a 5% (w/v) PLGA solution.

From Table 7.1, a concentration of 10ppm was chosen as a conductivity of 15.54 μS/m was sufficiently close to the control solvent formulation ensuring particle size would not be radically affected. The UV-Vis measurements demonstrated the strength of the absorbance signal from all different dye concentrations and therefore 10ppm reveals a clear absorbance peak detected at 515nm, shown below in Figure 7.01. This ensured signal detection would be strong from the dye-loaded particles, along with a sufficient conductivity to electrospray in the cone-jet mode.

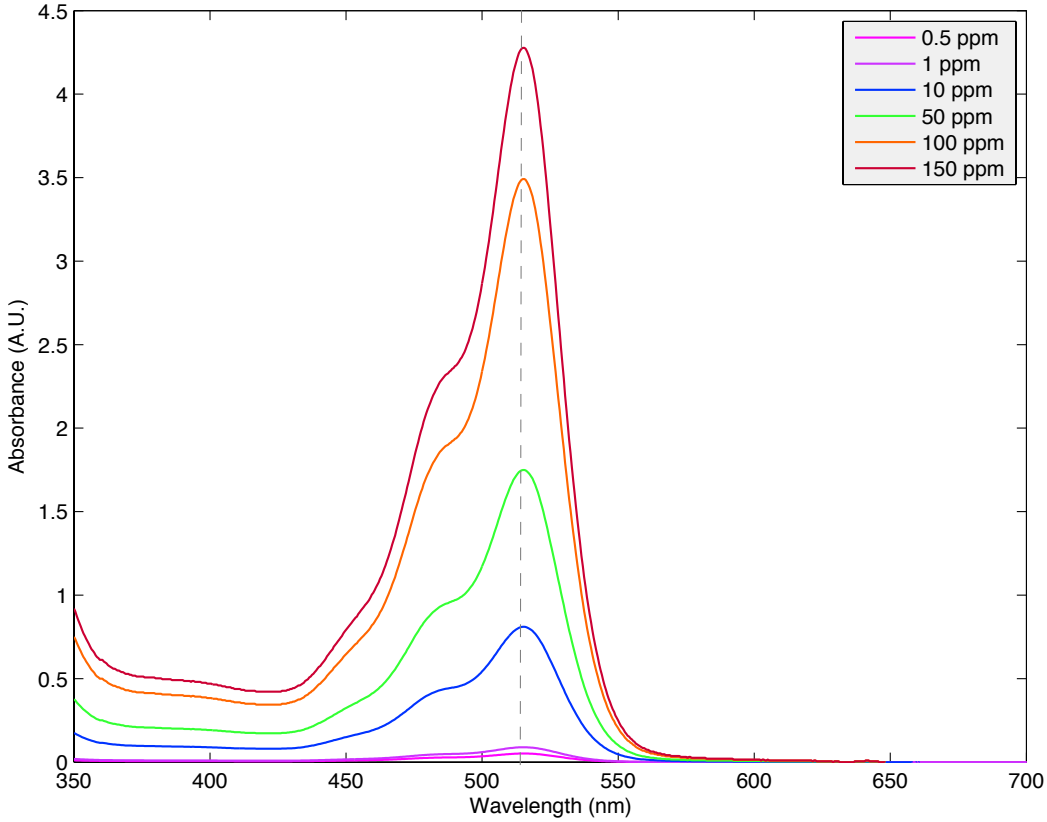

FIGURE 7.01. UV/Vis spectra of R6G dye solutions at six concentrations (shown in key). R6G peaks were detected at 515nm for each sample.

The absorbance signal measured below 10ppm dye concentration were not sufficient for electrospraying particles loaded with R6G as the UV/Vis instrument would not be sensitive enough to detect the released dye from particles in the following dissolution studies.

7.2 ENCAPSULATION EFFICIENCY

The encapsulation efficiencies (EE) were calculated according to Equation 5. The dye contents were then calculated by reference to a standard calibration curve (shown below in Figure 7.02), formed from 6 different concentrations (0.5ppm – 150ppm) in the same solvent (Figure 7.01). The calibration curve was found to be highly linear and reproducible, with a coefficient of determination (R2) of ≥0.98.

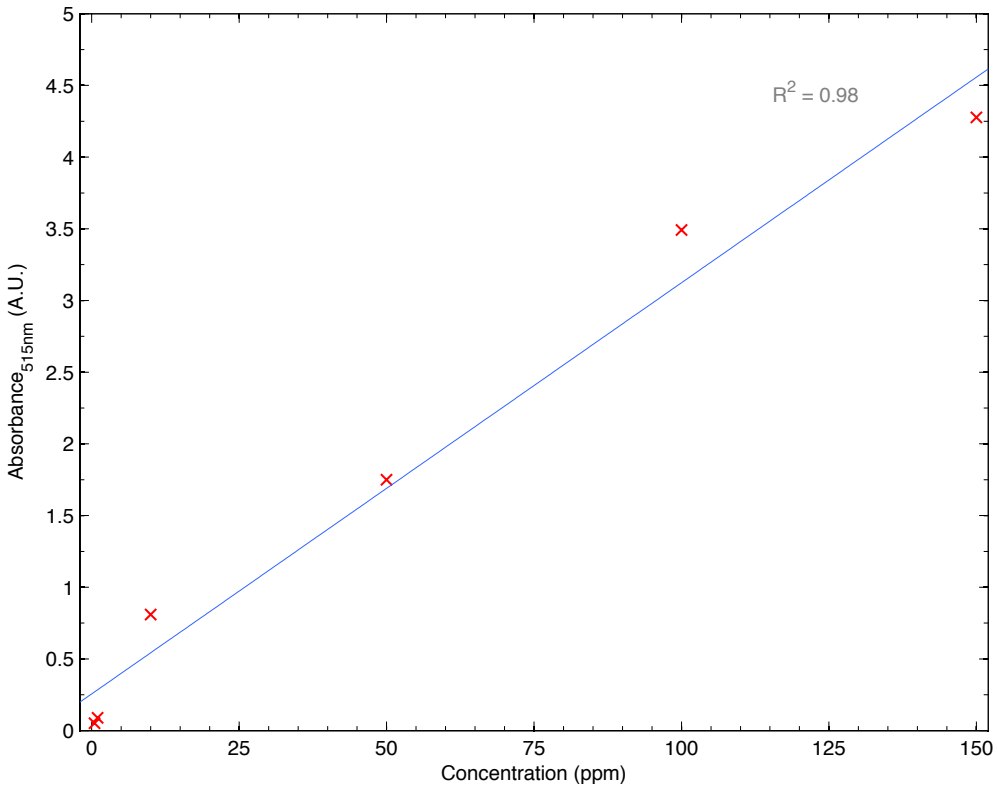

FIGURE 7.02. A standard calibration curve, formed from 6 different concentrations (0.5ppm – 150ppm) of R6G dye. Absorbance was recorded at 515nm peaks (taken in Figure 7.01).

The EE for each particle size category can be seen below in Table 7.2.

(R6G-loaded) Particle Size (μm)	R6G Concentration (ppm)	Encapsulation Efficiency (%)
Small, ~10–20	10	93.28
Medium, ~100–150	10	90.25
Large, ~200–250	10	89.29

TABLE 7.2. Summary of the encapsulation efficiencies reported for the categorized particle sizes (i.e. small, medium and large).

As seen in Table 7.2, particles were categorized as (1) small (~10–20μm), (2) medium (~100–150μm) and (3) large (~200–250μm) with dye concentrations of 10ppm consistently across all three samples. Small particles revealed the largest EE at 93.28% and the EE gradually decreased with increasing particle size, with medium at 90.25% and large particles at 89.29%. It must be noted however that there was no real significant difference between samples and all reported an EE >89%. The differences in EE were believed to have stemmed from the differences in porosity measured for particles without R6G dye and the ability of the micro-vehicle carrier to encapsulate the active agent. Smaller particles without dye (~10–20μm) were reported to have a porosity of 94.38% whereas large particles reported 38.62%. The larger porosity suggests smaller particles would have a larger EE, associated with their ability to encapsulate a larger amount of material within their microporous structure however there was no significant difference here to discriminate against size difference.

7.3 *IN VITRO* RELEASE STUDY – MICROSPHERE SIZE

Dissolution tests overall investigated the effect of TIPS microsphere size on the release performance of an encapsulated agent (i.e. R6G dye) within the polymer matrix of the TIPS particle. This was achieved by mixing PLGA solutions within known concentrations of dye, subsequently followed by electrospraying. The emitter was kept sufficiently close to the LN_2 collection bath (40mm) and this was done to ensure particles accelerated directly into the LN_2 medium, as seen in Figure 7.03. Minimizing particle loses for the dissolution test was important to ensure sufficient mass was produced.

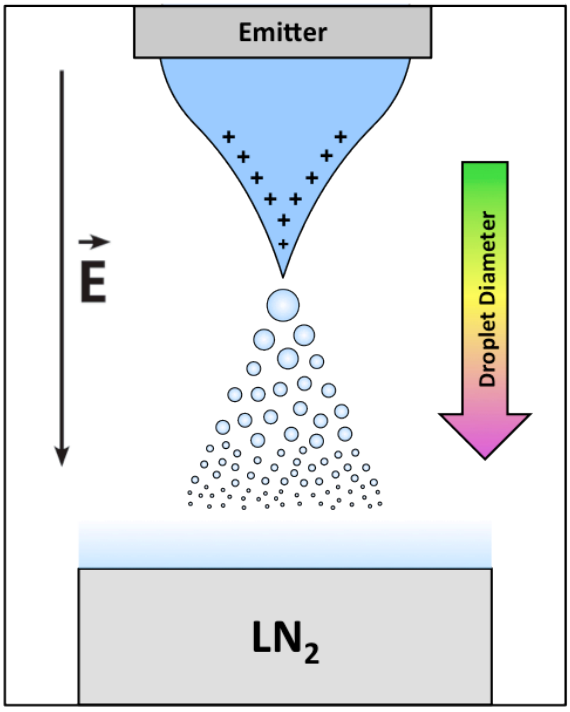

FIGURE 7.03. Electrospraying PLGA droplets into an electrically grounded LN_2 collection bath.

The rate of Rhodamine 6G (R6G) release from biodegradable polymeric microspheres can be driven by several mechanisms. The SEM images in Figure 7.04(a-c) show the synthesized particles have a porous structure and have retained their typical TIPS structure. Here, release is therefore influenced predominantly by three factors, (i) desorption of surface-bound dye, (ii) diffusion of dye through the polymer matrix and (iii) erosion of the polymer matrix [182]. For PLGA particles, the surface-bound dye experiences an initial rapid release due to the large surface area of the particles. The porous structure of the polymeric particle enables diffusion and penetration of water and therefore facilitates its hydrolytic degradation and subsequent dye release [183].

Figure 7.04 demonstrates that the particle diameter increases with flow rate, previously demonstrated with control samples (without dye). Particles appeared to retain their spherical structure and there was no obvious change in morphology when particles were loaded with an encapsulated agent, as seen in Figure 7.04(a-c). Furthermore, electrospraying in the cone-jet stability regime was maintained between 1-30 mL/hr and therefore monodispersity amongst particles within this range was clear under SEM analysis. By varying the flow rate of polymer solution to the emitter, it is possible to control the size of the synthesized particles although monodispersity will be lost when electrospraying outside of the stability regime. The uniform particle morphologies achieved here reveal that irregular-sized particles are not present and any unexpected variations in release kinetics will not be the result of particle dispersity. Samples that are generally polydisperse are likely to result in unpredictable release behaviour.

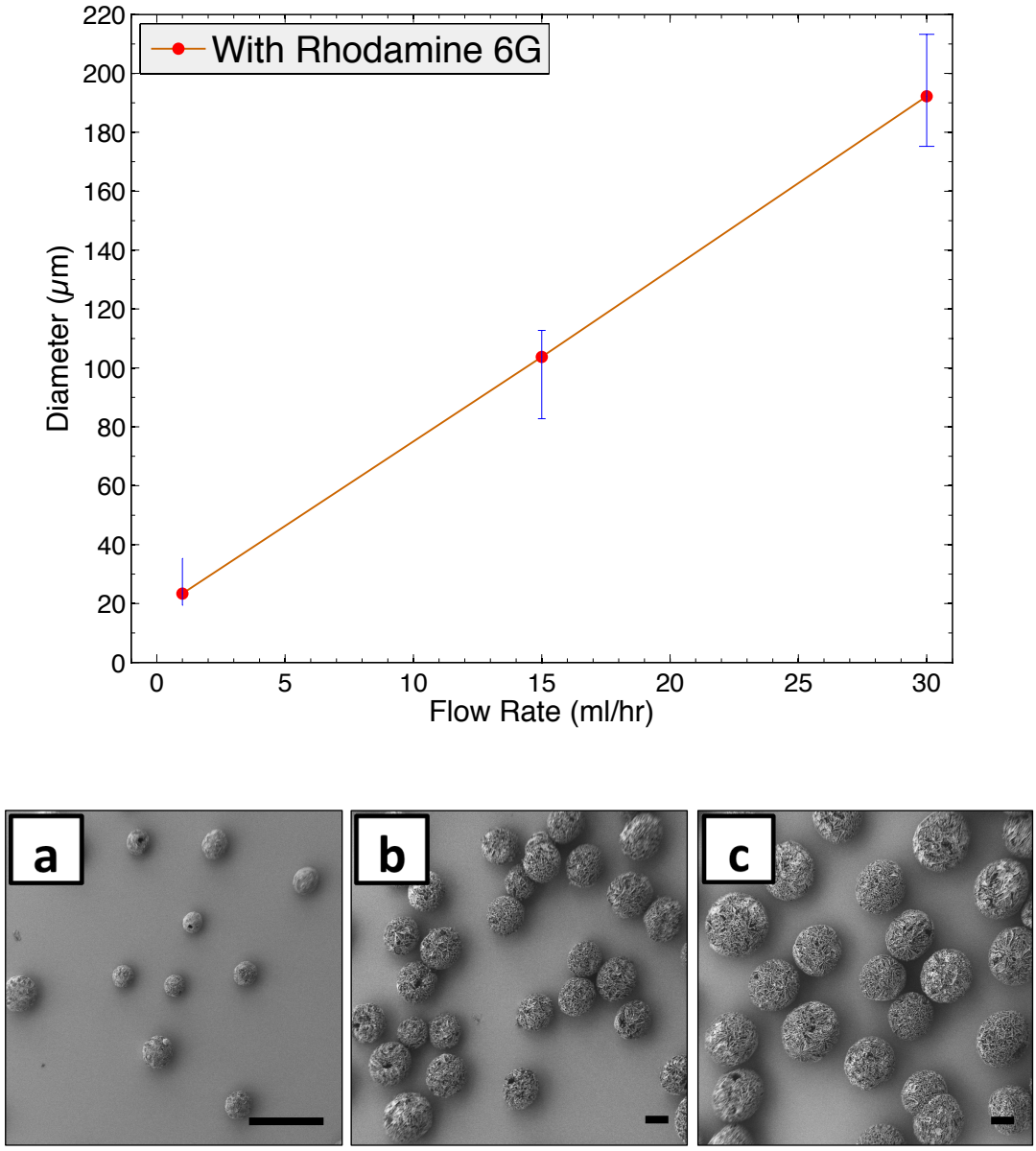

FIGURE 7.04. Dependence of R6G-loaded TIPS microsphere size on flow rate. SEM images of particles synthesized at (a) 1 mL/hr (scale bar: 30μm) (b) 15 mL/hr (scale bar: 60μm) and (c) 30 mL/hr (scale bar: 100μm).

In vitro comparison of the release profiles of R6G from particles was made. Particles were categorized as (1) small (~10–20μm), (2) medium (~100–150μm) and (3) large (~200–250μm) with dye concentrations of 10ppm consistently across all three samples and encapsulation efficiencies >89%. Small particles reported the highest encapsulation efficiency of 93% although more importantly there was no real significant difference between samples. The cumulative R6G release profile for the three compositions in Figure 7.05 demonstrates a clear time-dependent release of R6G for all three samples. The size of the microspheres affects the duration of dye release (larger particles lead to more prolonged release). Larger particles are more likely to have dye trapped in the particle centre and therefore may not release their entire payload. Moreover a longer study would be required to assess whether particles ever release 100% of the encapsulated agent.

Dissolution studies revealed diffusion of the encapsulated agent in two distinct phases in the cumulative release profile: a first phase in which the release is dominated by diffusion and a second phase with a slower release related to the erosion of the polymer matrix. In the first phase, microspheres released most of their payload (≥50%) within 24 hours and for smaller particles, release occurred more rapidly. This also indicates that the percentage cumulative release of R6G from highly porous microspheres was significantly higher than that of particles with lower porosities (i.e. of larger sizes). Initial burst release was seen in all three samples due to the incorporated dye being close to, or on, the particle surface thus was instantaneously solubilized out of the particles in release medium. The internal pore network and surface pores act as channels to allow rapid penetration of the dissolution medium into the core. Following this, a second phase revealed a sustained release over one week (~10,080 minutes) for all particle sizes. Despite this, it must be noted the release profiles of all three cases appear similar; the disparity was believed to

stem from differences in particle surface area-to-volume ratio. Similarity in trends suggests the microspheres are highly monodisperse as each particle size follows a similar path. A polydisperse sample would introduce undesired variations in release kinetics.

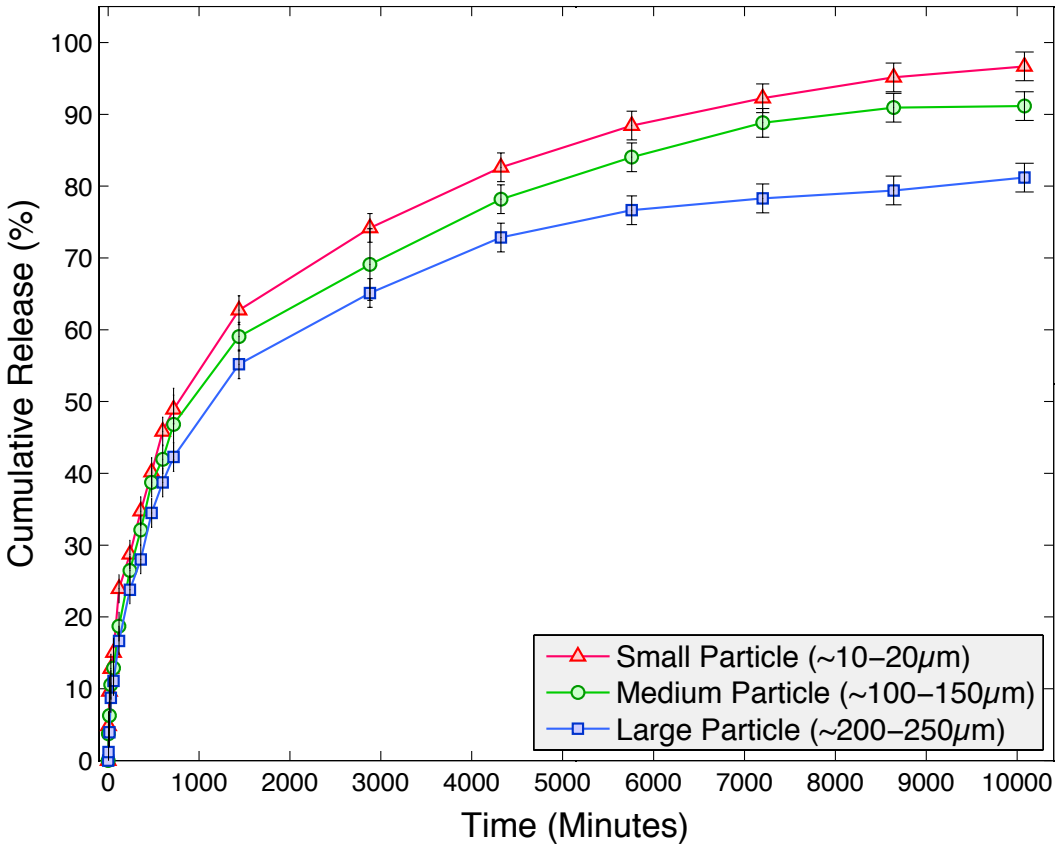

FIGURE 7.05. *In vitro* cumulative R6G release from small (red/triangles), medium (green/circles) and large-sized (blue/squares) PLGA TIPS microspheres.

These results suggest that release kinetics of polymeric carriers can be manipulated by alteration of particle size. Moreover, the study has demonstrated the feasibility of controlling the R6G release behaviour from porous PLGA TIPS microspheres by careful manipulation of flow rate during synthesis.

The microspheres manufactured here have successfully demonstrated long-term delivery (i.e. 1 week) of an active agent, enabling sustained release of the dye without excessive physical degradation, as seen in Figure 7.06. The SEM results demonstrate evidence of minor physical degradation of the particle structure and this is due to the hydrolytic action of the release medium with the particles. Figure 7.06(a) reveal that the highly porous smaller particles suffered severe surface degradation due to the ability of the release medium to enter and penetrate the pores on the surface of the particles. This led to the immediate solubilization of the dye from the particles by diffusive action. This was realized in the first phase whereby a greater release by diffusion was prominent in smaller particles (red curve in Figure 7.05) within the first 24 hours. The difference between small and large particles was more explicit after the conclusion of the 7-day study, at which point large particles had released ~81% of their payload, while smaller particles had released ~97% after the week. Towards the end of the week, it was also clear that medium and large-sized particles had reached a plateau where there was no significant further release of R6G from the particles. This would suggest that any dye trapped within the particle would not be released until the particles were mixed within the original solvent formulation used to prepare them (i.e. DMC, Formic Acid and DI Water). Finally, it must be noted that the images below in Figure 7.06 demonstrate that regardless of the degree of degradation of the particle, each size category retained their shape; an important factor to regulate and control the release of an active agent.

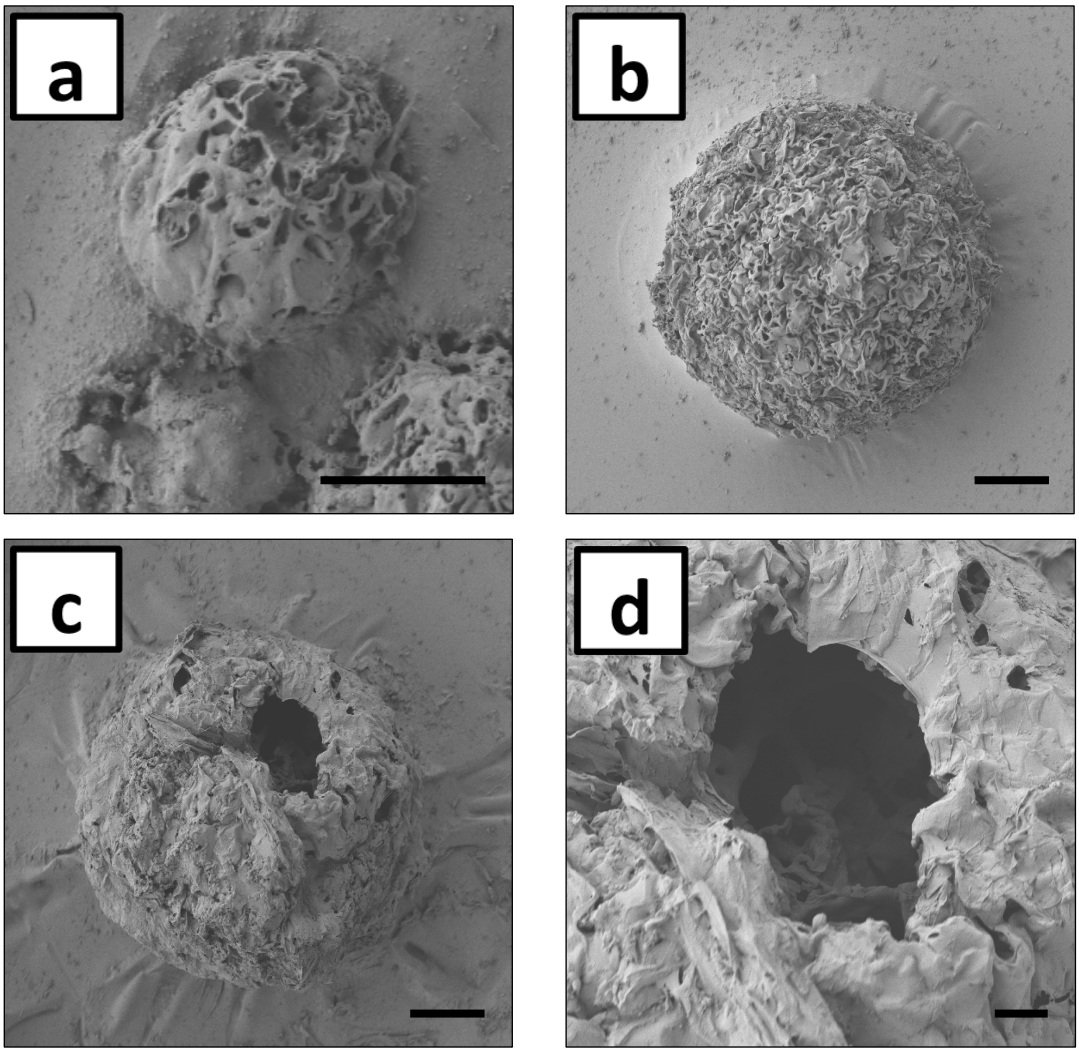

FIGURE 7.06. SEM images of particle degradation in release medium at 37°C over 7 days for (a) small particles (scale bar: 10μm) (b) medium particles (scale bar: 20μm) and (c) large particles (scale bar: 30μm) (d) high magnification micrograph of surface pore degradation as seen for the large particle in (c) (scale bar: 5μm).

This *in vitro* study reveals a clear dependence of microsphere size on the residual release of the encapsulated dye from the TIPS microsphere carrier. Clearly, microsphere size will strongly affect the rate of dye release. As size decreases, the surface area-to-volume ratio of the particle increases. Thus, for a given rate of dye diffusion through the microsphere, the rate of flux of dye out of the microsphere, per mass of formulation, will increase with decreasing particle size. In addition, water penetration into smaller particles may be quicker due to the shorter distance from the surface to the center of the particle. Also, while the decrease in surface area with increases in particle size may lead to a decreased rate of erosion of poorly water-permeable polymers like polyanhydrides, release rates (per mass of polymer) will be faster for smaller polyanhydride microspheres.

This study also lays the platform to study the release of antibiotics from the particles and assess how this would perform within different insoluble microenvironments, e.g. Phosphate Buffered Saline (PBS), Simulated Body Fluid (SBF) and *in vivo* studies with animal subjects. The degree of hydrolytic degradation will vary across release medium, along with the ability of the medium to penetrate the particle surface, enter pores and solubilize the encapsulated agents. These variations will effectively depend on factors such as the concentration, surface tension and viscosity of the release medium.

8. CONCLUSIONS

SUMMARY & FUTURE

8.1 MAJOR CONCLUSIONS

In this chapter we review the main conclusions from this dissertation, and provide some insight and final comments about topics that were not approached for lack of time, but that are worthy of future investigations. The major conclusions have been divided into 'Part A' and 'Part B' to reflect the clear differentiation in techniques and protocols used to manufacture the micro/nano-structures for different application. Part A summarizes the conclusions made for the electrospun fabrication of polymer/Au composites and Part B summarizes the conclusions made for the electrospray synthesis of PLGA TIPS microspheres and their functionality. Section 8.2 covers the future research that would need to be conducted to support the work and findings from these studies. Furthermore, the suggestions for future work (for both 'Part A' and 'Part B') have been divided into their own section to address the challenges associated with the electrospun fabrication of polymer/nanoparticle composites and also the synthesis of polymeric microparticle carriers.

PART A – PEO/Au NP COMPOSITES

Principal conclusions follow:

• We have successfully reported a frugal-driven approach for the one-step fabrication of tunable PEO/Au NP composite nanowires at ambient temperatures. The novelty of the methodology lies in the simplicity of their synthesis without using costly materials and nanofabrication technologies. This procedure circumvents the space, regulation, control, standards and maintenance necessary for state-of-the-art cleanroom facilities. Whilst conventional nanofabrication methods rely on batch-type processes, the electrospinning technique is a rapid jetting process and offers less complex scaling challenges.

• The addition of metallic Au NPs produced a linear increase in solution conductivity and subsequently led to a reduction in fibre diameter. This was conclusively associated with the increasing presence of nanoparticles in the solution as the solvent formulation was not adjusted and the polymer concentration was kept consistent throughout the fabrication of the polymer/nanoparticle composites, at 5% (w/w).

• Bright-field and dark-field STEM images revealed for the first time the presence and distribution of Au NPs within the fibres. Dark-field STEM proved most effective in analyzing single fibres containing Au NPs and dark-field imaging effectively revealed the nanoparticle distribution within the fibres, enhancing the contrast by discriminating against the local atomic number of the material. Attempts were made to further analyze the optical presence of the increasing nanoparticle loading in the fibres although this was difficult to measure due to the difficulty of performing UV/Vis measurements of the fibres.

• I-V measurements revealed resistive switching behaviour with samples containing 30% (wt.) Au NPs although understanding the switching mechanism is a challenging task. Although it is possible to track the mechanism responsible for resistive switching, this could be possible using Conductive Atomic Force Microscopy (C-AFM) or Scanning Tunneling Microscope (STM) techniques. In-situ TEM can potentially reveal the dynamics of the filament (or conduction mechanism) evolution and could form the basis of future investigation. Although electrical switching in polymer/nanoparticle structures is poorly understood using the MIM configuration, little is known about the electrical behaviour of PEO alone and the contribution of either nanoparticles, polymer or a composite of the two (i.e. polymer/nanoparticles) to the switching mechanism.

The assembly process has not yet been refined and further improvement may enable greater control over how the particles are distributed within the polymer fibres. These structures are of immediate interest in nanoelectronics; as nano-tracks to wire nanocomponents together and can also have potential functionality in information technology for memory storage nanodevices. Additionally, other studies alike (using other metallic compounds) have shown application in nanophotonics and plasmonic technologies where highly ordered linear nanoparticle structures are required.

PART B – PLGA TIPS MICROSPHERES

Principal conclusions follow:

• The ES technique is unique in ensuring tight control over droplet/particle size once the electrical conductivity and flow rate were identified for the ideal processing window in obtaining the stable cone-jet. Specifically, it can provide high monodispersity of micrometre-size particles, commonly where other alternative synthesis techniques fail.

• The main parameters affecting particle size can be inferred from a semi-empirical scaling law, factoring two key variables affecting the particle size, including solution electrical conductivity and the feeding flow rate. Among these, the solution electrical conductivity is the main property controlling particle size. Not only can it be varied by orders of magnitude by adding small amounts of dopants, but its variation will further affect allowable flow rates (for a stable operation of the ES in the cone-jet mode). This study demonstrated how solution conductivity could be amplified by alteration of the solvent formulation, adding very small volumes of formic acid and DI water. This enabled the ES to be operated within a broad range of flow rates.

• Particle shape analysis revealed that particles retained their spherical shape regardless of their size. The findings of High Sensitivity Circularity for particles of different sizes demonstrated that the ES synthesis route does not significantly alter the geometric properties of the PLGA TIPS microspheres.

• ES (along with freeze drying) does not alter the physicochemical properties of the polymer microparticles, an important factor when preparing spherical particles for drug delivery. Other chemical-based methods rely on the removal

of surfactants and coatings, which would otherwise alter the physicochemical properties of the particle.

• Internal porosity of the TIPS microspheres is highly dependent on particle size. Porosity decreased with increasing particle size and this trend was not dependent on the ES technique. Particles smaller in size had the encapsulated agent solubilized out of the particle centre quicker than larger-sized particles.

• Our approach, entailing particle deposition in a LN_2 bath, not only provides control over particle size, morphology and compactness but also allows for the stabilization of the particles without further changes in particle size or morphology, and with minimal loss of encapsulated agent due to the instantaneous freezing of the polymer droplet.

• While conventional synthesis techniques rely on batch or emulsion methods, our ES-TIPS technique offers several advantages: In a single-step flow process, particles can be made encapsulating the agent with high efficiency (>89% encapsulation efficiency) and stored for long periods (i.e. long shelf-life). The spray process is continuous and can be adapted to a roll-to-roll process for industrial scale manufacture. Multiplexing of the ES sources is critical since it increases the throughput by orders of magnitude, without compromising the uniformity of the synthesized particles.

Importantly, throughout this series of studies, efforts were made to move the synthesis approach from the all too common empiricism of a large fraction of the literature on materials synthesis, and to establish fundamental criteria that allow for the generation of particles of a prescribed size, morphology and consistency. As a result, the extension of the approach to different drug/polymer combinations should be facilitated.

8.2 FUTURE RESEARCH

PART A – PEO/Au NP COMPOSITES

Suggestions for future work follow:

• Although we have extensively studied the fabrication process as well as the performance of electrospun nanodevices, there are still multiple tasks left to further explore in this area. The polymer material we used in this study is mostly a model demo polymer, PEO. However, the cost of other synthetic or conductive polymers is high relative to PEO dissolved in DI water. It would be very promising if a substitute polymer could be found to replace PEO in this fabrication process with effective device performance yet still match the cost-effective benefits that PEO offers. Natural polymers would be the immediate choice for this substitution and will also widen the application of this work to other domains, e.g. life sciences.

• Further process optimization is required to ensure nanoparticle distribution within the polymer fibres is controllable. Suggestions for attempting to improve this would involve fabricating composites using a range of natural or synthetic polymers capable of being electrospun using a batch of concentrations that enable the onset of electrospinning. A more detailed study of the effect of the molecular weight of the polymer on the morphology of the obtained fibres containing metallic nanoparticles would aid the investigations performed here.

• Understanding the effects of solvent volatility and evaporation on the thinning of fibres during their flight would provide an insight into the optimal nanoparticle size that should be electrospun within the polymer. If the mean nanoparticle size is greater than the bulk polymer fibre, this can result in

nanoparticles being expelled from the fibre and effectively disrupt the formation of evenly distributed particles within the polymer matrix.

• Future studies could involve greater control over surface chemistry. By preparing polyethylene glycol-grafted (PEGylated) nanoparticles, one can carefully tailor nanoparticle placement within a polymer matrix and thereby form structures that are decorated with particles in a well-defined manner. It also can overcome aggregation, which negates any benefits associated with the nanoscopic dimension and therefore enable control over electrical performance. Not only would grafting impart hydrophilicty and biocompatibility to the particles but also produce a consistent, homogenous blend for electrospinning.

• Investigations into the careful fabrication of the nanodevices requires efforts to optimize the I-V performance of the devices. Assessing the optimum material for the electrode contacts could involve the use of other metallic contacts. Furthermore, altering the distance of the contacts in fabricated devices will allow precision control of the strength of the electric field and also the reproducible control of the electrical performance.

• Finally, seeking control over the randomly oriented fibres using a customized near-field electrospinning deposition approach can overcome the lack of control over the current non-linear bending instabilities in the electrospinning jet. It can offer control over nanowire deposition to print linear parallel tracks for ultra-small integrated circuit design. Additionally, and prior to this, a more detailed study is essential to understand the effects of nanoparticle concentration, aggregation effects of nanosuspensions in polymers and particle distribution within nanofibres.

PART B – PLGA TIPS MICROSPHERES

Suggestions for future work follow:

• Even though our ES synthesis process has been shown at the micrometric scale, the results are expected to apply also at the nanometric scale. The manufacturing of polymeric nanoparticles was not performed in this study, since our efforts were focused on other aspects of the research that could provide more insight into characterizing the particles and the effects of ES atomization. However, showing our ability to synthesize such small particles using a technique capable of competitive production rates is important for practical applications, and should be considered for future projects.

• Increasing the production of particle carriers has to be completed with the appropriate choice of electrode configuration and applied voltages to use, to create an electric field capable of avoiding droplet flyback, while ensuing complete evaporation. Ensuring the particle collection efficiency is consistently optimized to collect all the material emitted is vital to reveal the commercial capabilities of the electric field-driven atomization route to manufacture.

• The diminutive flow rates required for the synthesis of sufficiently small microparticles limit the ES production rate, and require scaling up in order to make this technique attractive for practical applications. The use of multiplexing (that is, the parallel operation of several ES sources) allows the increase of the throughput by orders of magnitude without modifying the properties of the obtained particles. Packing densities in the multiplexed devices depend on the number of nozzles, the current emitted per nozzle, the driving field and the residence time of the droplets in their flight towards the collector.

• Analyzing how particles degrade and predicting this behaviour is also necessary to support the research conducted here. The use of confocal microscopy to analyze the release of a drug from an individual, isolated particle is another interesting experiment to perform. A comparison with the release profiles obtained from different particle batches could provide information about the existence or lack of bulk effects in the release of a drug. Ultimately, these release experiments should also be performed *in vivo* to account for the biological effects (related with the clearance of particles by the immune system) in the drug release. *Ex vivo* studies of particle-macrophage behaviour would allow experimentalists and clinicians to understand the particle sizes tolerable within biological microenvironments.

• Focusing on the synthesis of particles, a more detailed study of the effect of the molecular weight of the polymer on the morphology of the obtained particles would be desirable. Additional improvements would include the consideration of the mass loss experienced by the droplet during Coulomb fission and the use of a simplified electric field configuration to avoid the onset of fibre spinning.

• Examining the release of encapsulated compounds from the ES PLGA TIPS microspheres would be the next suitable *in vitro* follow-up study to see how the release performance compares with the dye-loaded microspheres.

• Lastly, the effect of the drug on the final characteristics of particles synthesized by the ES route is a potentially important factor that should be taken into consideration in future studies. Even though the dye surrogate used in our studies are small molecules as compared with the size of the polymer chains, larger proteins or other pharmaceutical-grade compounds can make the contribution of these macromolecules significant in the final outcome.

REFERENCES

[1] J. A. Champion, Y. K. Yatare, S. Mitragotri, Making polymeric micro- and nanoparticles of complex shapes, *Proceedings of the National Academy of Sciences of the United States of America*, 104 (29), pp. 11901-11904, 2007.

[2] Z. L. Wang, Characterizing the Structure and Properties of Individual Wire-Like Nanoentities, *Advanced Materials,* 12 (17), pp. 1295-1993, 2000.

[3] F. Cerrina, C. Marrian, *MRS Bulletin,* 56, December 1996.

[4] J. M. Gibson, *Physics Today,* 56, October 1997.

[5] S. H. Hong, J. Zhu, C. A. Mirkin, *Science*, 286, pp. 523-525, 1999.

[6] M. D. Levenson, *Solid State Technology, 81,* September 1995.

[7] Z. Y. Tang, N. A. Kotov, One-dimensional assemblies of nanoparticles: preparation, properties, and promise, *Advanced Materials,* 17 (8), pp. 951-962, 2005.

[8] Z. Nie, A. Petukhova, E. Kumacheva, Properties and emerging applications of self-assembled structures made from inorganic nanoparticles, *Nature Nanotechnology,* 5, pp. 15-25, 2010.

[9] A. N. Shipway, E. Katz, I. Willner, Nanoparticle Arrays on Surfaces for Electronic, Optical, and Sensor Applications, *ChemPhysChem,* 1, pp. 18-52, 2000.

[10] S. A. Maier, P. G. Kik, H. A. Atwater, S. Meltzer, E. Harel, B. E. Koel, A. A. G. Requicha, Local detection of electromagnetic energy transport below the diffraction limit in metal nanoparticle plasmon waveguides, *Nature Materials*, 2 (4), pp. 229-232, 2003.

[11] A. C. Balazs, T. Emrick, T. P. Russell, Nanoparticle polymer composites: where two small worlds meet, *Science,* 314 (5802), pp. 1107-1110, 2006.

[12] K. Park, Controlled drug delivery systems: Past forward and future back, *Journal of Controlled Release* 190, pp. 3-8, 2014.

[13] A. K. Sheela, Microspheres Market - Global Industry Analysis, Size, Share, Growth, Trends and Forecast (2013 – 2019), www.researchmoz.us, accessed: 08/2015.

[14] E. Campos, J. Branquinho, A. S. Carreira, A. Carvalho, P. Coimbra, P. Ferreira, M. H. Gill, Designing polymeric microparticles for biomedical and industrial applications, *European Polymer Journal*, 49, pp. 2005-2021, 2013.

[15] A. Jaworek, Micro- and nanoparticle production by electrospraying, *Powder Technology,* 176, pp. 18-35, 2007.

[16] S. Mitragotri, P. A. Burke, R. Langer, Overcoming the challenges in administering biopharmaceuticals: formulation and delivery strategies, *Nature Reviews Drug Discovery,* 13, pp. 655-672, 2014.

[17] J. A. Champion, S. Mitragotri, Shape Induced Inhibition of Phagocytosis of Polymer Particles, *Proceedings of the National Academy of Sciences of the United States of America*, 26 (1), pp. 244-249, 2009.

[18] S. M. Moghimi, A. C. Hunter, J. C. Murray, Long-circulating and target-specific nanoparticles: theory to practice, *Pharmacological Reviews,* 53 (2), pp. 283-318, 2001.

[19] M. Okubo, Y. Konishi, H. Minami, Production of hollow polymer particles by suspension polymerization, *Colloid and Polymer Science,* 276 (7), pp. 638-642, 1998.

[20] R. Arshady, Microspheres and Microcapsules: A Survey of Manufacturing Techniques, *Polymer Engineering and Science,* 29 (24), pp. 1746-1758, 1989.

[21] Y. Zhang, Y. Guan, S. Yang, J. Xu, C.C. Han, Fabrication of Hollow Capsules Based on Hydrogen Bonding, *Advanced Materials,* 15 (10), pp. 832-835, 2003.

[22] M. Fujiwara, K. Shiokawa, T. Kubota, Direct encapsulation of proteins into calcium silicate microparticles by water/oil/water interfacial reaction method and their responsive release behaviors, *Materials Science and Engineering C.*, 32, pp. 2484-2490, 2012.

[23] C. A. E. Hamlett, S. N. Jayasinghe, J. A. Preece, Electrospinning nanosuspensions loaded with passivated Au nanoparticles, *Tetrahedron*, 64, pp. 8476-8483, 2008.

[24] G. M. Kim, A. Wutzler, H. J. Radusch, G. H. Michler, P. Simon, R. A. Sperling, W. J. Parak, One-Dimensional Arrangement of Gold Nanoparticles by Electrospinning, *Chemistry of Materials,* 17 (20), pp. 4949-4957, 2005.

[25] J. Bai, Y. Li, S. Yang, J. Du, S. Wang, J. Zheng, Y. Wang, Q. Yang, X. Chen, X. Jing, A simple and effective route for the preparation of poly(vinylalcohol) (PVA) nanofibers containing gold nanoparticles by electrospinning method, *Solid State Communications,* 141, pp. 292-295, 2007.

[26] J. Bai, C. Li, S. Wang, Y. Zhang, A Novel Approach to Prepare Gold Nanoparticles/Polyacrylamide Composite Nanofibers, *Rare Metal Materials and Engineering*, 42 (3), pp. 474-477, 2013.

[27] K. Gries, H. Vieker, A. Gölzhäuser, S. Agarwal, A. Greiner, Preparation of Continuous Gold Nanowires by Electrospinning of High-Concentration Aqueous Dispersions of Gold Nanoparticles, *Small,* 8 (9), pp. 1436-1441, 2012.

[28] J. K. Kim, H. Ahn, Fabrication and Characterization of Polystyrene/Gold Nanoparticle Composite Nanofibers, *Macromolecular Research*, 16 (2), pp. 163-168, 2008.

[29] V. G. Pol, E. Koren, A. Zaban, Fabrication of Continuous Conducting Gold Wires by Electrospinning, *Chemistry of Materials,* 20, pp. 3055-3062, 2008.

[30] S. Ramakrishna, K. Fujihara, W. E. Teo, T. C. Lim, Z. Ma, An Introduction to Electrospinning and Nanofibres*, World Scientific Publishing Co. Pte. Ltd*, Singapore, 2005.

[31] A. S. Nain, J. C. Wong, C. Amon, M. Sitti, Drawing suspended polymer micro-/nanofibers using glass micropipettes, *Appl. Phys. Lett.*, 89, pp. (183105) 1-3, 2006.

[32] X. Xing, Y. Wang, B. Li, Nanofiber drawing and nanodevice assembly in poly(trimethylene terephthalate), *Optics Express*, 16 (14), pp. 10815-10822, 2008.

[33] T. Tatte, M. Hussainov, M. Paalo, M. Part, R. Talviste, V. Kiisk, H. Mändar, K. Pohako, T. Pehk, K. Reivelt, M. Natali, J. Gurauskis, A. Lohmus, U. Mäeorg, Alkoxide-based precursors for direct drawing of metal oxide micro- and nanofibres, *Sci. Technol. Adv. Mater.*, 12, pp. 1-12, 2011.

[34] A. Huczko, Template-based synthesis of nanomaterials, *Appl. Phys. A Mater. Sci. Process.*, 70 (4), pp. 365-376, 2000.

[35] L. Feng, S. Li, Y. Li, H. Li, L. Zhang, J. Zhai, Y. Song, B. Liu, L. Jiang, D. Zhu, Super-Hydrophobic Surfaces: From Natural to Artificial, *Adv. Mater.*, 14 (24), pp. 1857-1860, 2002.

[36] C. Ozgit-Akgun, F. Kayaci, I. Donmez, T. Uyar, N. Biyiki, Template-Based Synthesis of Aluminum Nitride Hollow Nanofibers Via Plasma-Enhanced Atomic Layer Deposition, *J. Am. Ceram. Soc.*, 96 (3), pp. 916-922, 2012.

[37] Y. Wang, M. Zheng, H. Lu, S. Feng, G. Ji, J. Cao, Template Synthesis of Carbon Nanofibers Containing Linear Mesocage Arrays, *Nanoscale Res. Lett.*, 5 (6), pp. 913-916, 2010.

[38] H. Liang, Q. Guan, L. Chen, Z. Zhu, W. Zhang, S. Yu, Macroscopic-Scale Template Synthesis of Robust Carbonaceous Nanofiber Hydrogels and Aerogels and Their Applications, *Angew. Chem. Int. Ed.*, 51 (21), pp. 5101-5105, 2012.

[39] M. Ikegame, K. Tajima, T. Aida, Template Synthesis of Polypyrrole Nanofibers Insulated within One-Dimensional Silicate Channels: Hexagonal versus Lamellar for Recombination of Polarons into Bipolarons, *Angew. Chem. Int. Ed.*, 42 (19), pp. 2154-2157, 2003.

[40] C. M. Zelenski, P. K. Dorhout, Template Synthesis of Near-Monodisperse[1] Microscale Nanofibers and Nanotubules of MoS_2, *J. Am. Ceram. Soc.*, 120 (4), pp. 734-742, 1998.

[41] Y. Chen, Nanofabrication by electron beam lithography and its applications: A review, *Microelectron. Eng.*, 135, pp. 57-72, 2015.

[42] W. Yue, Z. Wang, Y. Yang, L. Chen, A. Syed, K. Wong, X. Wang, Electron-beam lithography of gold nanostructures for surface-enhanced Raman scattering, *Journal Of Micromechanics And Microengineering*, 22, pp. 1-9, 2012.

[43] A. Perez-Junquera, J. I. Martin, J. M. Alameda, One-step fabrication of large area arrays of dots by electron beam lithography, *Microelectron. Eng.*, 84, pp. 845-847, 2007.

[44] S. A. Maier, M. L. Brongersma, P. G. Kik, H. A. Atwater, Observation of near-field coupling in metal nanoparticle chains using far-field polarization spectroscopy, *Phys. Rev. B*, 65, pp. (193408)1-4, 2002.

[45] E. M. Hicks, S. Zou, G. C. Schatz, K. G. Spears, R. P. Van Duyne, L. Gunnarsson, T. Rindzevicius, B. Kasemo, M. Kall, Controlling Plasmon Line Shapes through Diffractive Coupling in Linear Arrays of Cylindrical Nanoparticles Fabricated by Electron Beam Lithography, *Nano Lett.*, 5 (6), pp. 1065-1070, 2005.

[46] L. Clarke, M. N. Wybourne, M. Yan, S. X. Cai, J. F. W. Keana, Transport in gold cluster structures defined by electron-beam lithography, *Appl. Phys. Lett.*, 71 (5), pp. 617-619, 1997.

[47] M. Grzelczak, J. Vermant, E. M. Furst, L. M. Liz- Marzan, Directed Self-Assembly of Nanoparticles, *ACS Nano*, 4 (7), pp. 3591-3605, 2010.

[48] P. Suvannasara, N. Praphairaksit, N. Muangsin, Self-assembly of mucoadhesive nanofibers, *RSC Adv.*, 4, pp. 58664-58673, 2014.

[49] K. Zhang, M. Jiang, D. Chen, DNA/Polymeric Micelle Self-Assembly Mimicking Chromatin Compaction, *Angew. Chem. Int. Ed.*, 51 (35), pp. 8744-8747, 2012.

[50] M. Li, H. Schnablegger, S. Mann, Coupled synthesis and self-assembly of nanoparticles to give structures with controlled organization, *Nature*, 402, pp. 393-395, 1999.

[51] A. K. Boal, F. Ilhan, J. E. DeRouchey, T. Thurn- Albrecht, T. P. Russell, V. M. Rotello, Self-assembly of nanoparticles into structured spherical and network aggregates, *Nature*, 404, pp. 746-748, 2000.

[52] N. Tucker, J. J. Stanger, M. P. Staiger, H. Razzaq, J. Hofman, The History of the Science and Technology of Electrospinning from 1600 to 1995, *Journal of Engineered Fibres and Fabrics*, 7, pp. 63-73, 2012.

[53] W. E. Teo, S. Ramakrishna, A review on electrospinning design and nanofibre assemblies, *Institute of Physics (IOP)*, 17, pp. 89-106, 2006.

[54] A. Formhals, Process and apparatus for preparing artificial threads, 1,975,504 (Patent), 1934.

[55] T. Subbiah, G.S. Bhat, R.W. Tock, S. Parameswaran, S. S. Ramkumar, Electrospinning of Nanofibres, *J. Appl. Polym. Sci.*, 96, pp. 557-569, 2005.

[56] G. Taylor FRS, Disintegration of Water Drops in an Electric Field, *Proc. R. Soc. London, Ser. A*, 280 (1382), pp. 383-397, 1964.

[57] D. H. Reneker, I. Chun, Nanometer diameter fibres of polymer, produced by electrospinning. *Institute of Physics (IOP)*, 7, pp. 216-223, 1996.

[58] J. Doshi, D. H. Reneker, Electrospinning Process and Applications of Electrospun Fibres, *J. Electrostat*, 35 (2-3), pp. 151-160, 1995.

[59] M. M. Hohman, M. Shin, G. Rutledge, M. P. Brenner, Electrospinning and electrically forced jets. II. Applications, *Phys. Fluids*, 13 (8), pp. 2221-2236, 2001.

[60] D. Li, Y. Xia, Electrospinning of Nanofibers: Reinventing the Wheel?, *Adv. Mater.*, 16 (14), pp. 1151-1170, 2004.

[61] W. Teo, R. Inai, S. Ramakrishna, Technological advances in electrospinning of nanofibers, *Sci. Tech. Adv. Mater.*, 12, pp. 1-19, 2011.

[62] N. Bhardwaj, S. C. Kundu, Electrospinning: A fascinating fiber fabrication technique, *Biotechnol. Adv.*, 28, pp. 325-347, 2010.

[63] M. Bogntizki, T. Frese, M. Steinhart, A. Greiner, J. H. Wendorff, Preparation of Fibers with Nanoscaled Morphologies: Electrospinning of Polymer Blends, *Polym. Eng. Sci.*, 41 (6), pp. 982-989, 2001.

[64] P. Gupta, C. Elkins, T. E. Long, G. L. Wilkes, Electrospinning of linear homopolymers of poly(methyl methacrylate): exploring relationships between fiber formation, viscosity, molecular weight and concentration in a good solvent, *Polymer*, 46, pp. 4799-4810, 2005.

[65] X. Zong, K. Kim, D. Fang, S. Ran, B. S. Hsiao, B. Chu, Structure and process relationship of electrospun bioabsorbable nanofiber membranes, *Polymer*, 43, pp. 4403-4412, 2002.

[66] H. S. Kim, K. Kim, H. J. Jin, I. Chin, Morphological Characterization of Electrospun Nanofibrous Membranes of Biodegradable Poly(L-lactide) and Poly(lactide-*co*-glycolide), *Macromol. Symp.* 224, pp. 145-154, 2005.

[67] J. M. Deitzel, J. Kleinmeyer, D. Harris, N. C. B. Tan, The effect of processing variables on the morphology of electrospun nanofibers and textiles, *Polymer*, 42, pp. 261-272, 2001.

[68] H. Fong, I. Chun, D. H. Reneker, Beaded nanofibers formed during electrospinning, *Polymer*, 40, pp. 4585-4592, 1999.

[69] W. K. Son, J. H. Youk, T. S. Lee, W. H. Park, The effects of solution properties and polyelectrolyte on electrospinning of ultrafine poly(ethylene oxide) fibers, *Polymer*, 45, pp. 2959-2966, 2004.

[70] A. Koski, K. Yim, S. Shivkumar, Effect of molecular weight on fibrous PVA produced by electrospinning, *Mater. Lett.*, 58, pp. 493-497, 2004.

[71] J. He, Y. Wan, J. Yu, Effect of concentration on electrospun polyacrylonitrile (PAN) nanofibers, *Fiber Polym.*, 9 (2), pp. 140-142, 2008.

[72] V. Jacobs, R. D. Anandjiwala, M. Maaza, The Influence of Electrospinning Parameters on the Structural Morphology and Diameter of Electrospun Nanofibers, *J. Appl. Polym. Sci.*, 115, pp. 3130-3136, 2010.

[73] J. S. Choi, S. W. Lee, L. Jeong, S. Bae, B. C. Min, J. H. Youk, W. H. Park, Effect of organosoluble salts on the nanofibrous structure of electrospun poly(3-hydroxybutyrate-*co*-3-hydroxyvalerate), *Int. J. Biol. Macromolec.*, 34 (4), pp. 249-256, 2004.

[74] T. Lin, H. Wang, H. Wang, X. Wang, The charge effect of cationic surfactants on the elimination of fibre beads in the electrospinning of polystyrene, *IOP Publishing Nanotechnology*, 15, pp. 1375-1381, 2004.

[75] R. Jalili, S. A. Hosseini, M. Morshed, The Effects of Operating Parameters on the Morphology of Electrospun Polyacrilonitrile Nanofibres, *Iran Polym. J.*, 14 (12), pp. 1074-1081, 2005.

[76] K. J. Pawlowski, H. L. Belvin, D. L. Raney, J. Su, J. S. Harrison, E. J. Siochi, Electrospinning of a micro-air vehicle wing skin, *Polymer*, 44 (4), pp. 1309-1314, 2003.

[77] S. Zhao, X. Wu, L. Wang, Y. Huang, Electrospinning of Ethyl–Cyanoethyl Cellulose/Tetrahydrofuran Solutions, *J. Appl. Polym. Sci.*, 91, pp. 242-246, 2004.

[78] X. Yuan, Y. Zhang, C. Dong, J. Sheng, Morphology of ultrafine polysulfone fibers prepared by electrospinning, *Polym. Int.*, 53, pp. 1704-1710, 2004.

[79] S. Megelski, J. S. Stephens, D. B. Chase, J. F. Rabolt, Micro- and Nanostructured Surface Morphology on Electrospun Polymer Fibers, *Macromolecules*, 35, pp. 8456-8466, 2002.

[80] C. J. Buchko, L. C. Chen, Y. Shen, D. C. Martin, Processing and microstructural characterization of porous biocompatible protein polymer thin films, *Polymer*, 40 (26), pp. 7397-7407, 1999.

[81] H. Kitching, M. J. Shiers, A. J. Kenyon, I. P. Parkin, Self-assembly of metallic nanoparticles into one dimensional arrays, *J. Mater. Chem. A,* 1, pp. 6985-6999, 2013.

[82] M. J. Shiers, R. Leech, C. J. Carmalt, I. P. Parkin, A. J. Kenyon, Self-Assembled Ultra-High Aspect Ratio Silver Nanochains, *Adv. Mater.*, 24, pp. 5227-5235, 2012.

[83] A. Haryono, W. H. Binder, Controlled Arrangement of Nanoparticle Arrays in Block-Copolymer Domains, *Small*, 2 (5), pp. 600-611, 2006.

[84] S. V. N. T. Kuchibhatla, A.S. Karakoti, D. Bera, S. Seal, One dimensional nanostructured materials, *Prog. Mater. Sci.*, 52, pp. 699-913, 2007.

[85] Y. Xia, P. Yang, Y. Sun, Y. Wu, B. Mayers, B. Gates, Y. Yin, F. Kim, H. Yan, One Dimensional Nanostructures: Synthesis, Characterization, and Applications, *Adv. Mater.*, 15 (5), pp. 353-389, 2003.

[86] R. Sardar, J. S. Shumaker-Parry, Asymmetrically Functionalized Gold Nanoparticles Organized in One-Dimensional Chains, *Nano Lett.*, 8 (2), pp. 731-736, 2008.

[87] R. R. Bhattacharjee, T. K. Mandal, Polymer-mediated chain-like self-assembly of functionalized gold nanoparticles, *J. Colloid Interface Sci.*, 307, pp. 288-295, 2007.

[88] J. J. Chiu, B. J. Kim, E. J. Kramer, D. J. Pine, Control of Nanoparticle Location in Block Copolymers, *J. Am. Chem. Soc.*, 127 (14), pp. 5036-5037, 2005.

[89] J. C. Zhou, X. Wang, M. Xue, Z. Xu, T. Hamasaki, Y. Yang, K. Wang, B. Dunn, Characterization of gold nanoparticle binding to microtubule filaments, *Mater. Sci. Eng. C*, 30, pp. 20-26, 2010.

[90] X. Lu, C. Wang, Y. Wei, One-Dimensional Composite Nanomaterials: Synthesis by Electrospinning and Their Applications*, Small*, 5 (21), pp. 2349-2370, 2009.

[91] C. Zhang, S. Yu, Nanoparticles meet electrospinning: recent advances and future prospects, *Chem. Soc. Rev.*, 43, pp. 4423-4448, 2014.

[92] D. Crespy, K. Friedemann, A. M. Popa, Colloid-Electrospinning: Fabrication of Multicompartment Nanofibers by the Electrospinning of Organic or/and Inorganic Dispersions and Emulsions, *Macromol. Rapid Commun.*, 33 (23), pp. 1978-1995, 2012.

[93] J. Wu, N. Wang, Y. Zhao, L. Jiang, Electrospinning of multilevel structured functional micro-/nanofibers and their applications, *J. Mater. Chem. A,* 1, pp. 7290-7305, 2013.

[94] C. Zhang, K. Lv, H. Cong, S. Yu, Controlled Assemblies of Gold Nanorods in PVA Nanofiber Matrix as Flexible Free-Standing SERS Substrates by Electrospinning, *Small*, 8 (5), pp. 648-653, 2012.

[95] D. He, B. Hu, Q. Yao, K. Wang, S. Yu, Large-Scale Synthesis of Flexible Free- Standing SERS Substrates with High Sensitivity: Electrospun PVA Nanofibers Embedded with Controlled Alignment of Silver Nanoparticles, *ACS Nano*, 3 (12), pp. 3993-4002, 2009.

[96] J. Lim, J. H. Moon, G. Yi, C. Heo, S. Yang, Fabrication of One-Dimensional Colloidal Assemblies from Electrospun Nanofibers, *Langmuir*, 22 (8), pp. 3445-3449, 2006.

[97] C. D. Saquing, J. L. Manasco, S. A. Khan, Electrospun Nanoparticle–Nanofiber Composites via a One-Step Synthesis, *Small*, 5 (8), pp. 944-951, 2009.

[98] N. J. Pinto, A. T. Johnson Jr., A. G. MacDiarmid, C. H. Mueller, N. Theofylaktos, D. C. Robinson, F. A. Miranda, Electrospun polyaniline/polyethylene oxide nanofiber field-effect transistor, *Appl. Phys. Lett.*, pp. 4244-4246, 2003.

[99] T. Shang, F. Yang, W. Zheng, C. Wang, Fabrication of Electrically Bistable Nanofibers, *Small*, 2 (8-9), pp. 1007-1009, 2006.

[100] J. Miao, M. Miyauchi, T. J. Simmons, J. S. Dordick, R. J. Linhardt, Electrospinning of Nanomaterials and Applications in Electronic Components and Devices, *J. Nanosci. Nanotechnol.*, 10 (9), pp. 5507-5519, 2010.

[101] J. Kane, J. Ong, R. F. Saraf, Chemistry, physics, and engineering of electrically percolating arrays of nanoparticles: a mini review, *J. Mater. Chem.*, 21, pp. 16846-16858, 2011.

[102] H. Chang, C. Liu, W. Chen, Flexible Nonvolatile Transistor Memory Devices Based on One-Dimensional Electrospun P3HT:Au Hybrid Nanofibers, *Adv. Funct. Mater.*, 23, pp. 4960-4968, 2013.

[103] Y. Lin, C. Lin, Y. Chou, C. Liu, H. Chang, W. Chen, Nonvolatile organic field effect transistor memory devices using one-dimensional aligned electrospun nanofiber channels of semiconducting polymers, *J. Mater. Chem. C*, 1, pp. 5336-5343, 2013.

[104] R. J. Tseng, J. Huang, J. Ouyang, R. B. Kaner, Y. Yang, Polyaniline Nanofiber/Gold Nanoparticle Nonvolatile Memory, *Nano Lett.*, 5 (6), pp. 1077-1080, 2005.

[105] C. O. Baker, B. Shedd, R. J. Tseng, A. A. Martinez-Morales, C. S. Ozkan, M. Ozkan, Y. Yang, R. B. Kaner, Size Control of Gold Nanoparticles Grown on Polyaniline Nanofibers for Bistable Memory Devices, *ACS Nano*, 5 (5), pp. 3469-3474, 2011.

[106] L. YingTao, L. ShiBing, L. Qi, L. HangBing, L. Su, L. Ming, An overview of resistive random access memory devices, *Chinese Sci. Bull.*, 56 (28-29), pp. 3072-3078, 2011.

[107] R. Waser, M. Aono, Nanoionics-based resistive switching memories, *Nat. Mater.*, 6, pp. 833-840, 2007.

[108] S. Fukushimaa, S. Kishimoto, Y. Takeuchi, M. Fukushima, Preparation and evaluation of o/w type emulsions containing antitumor prostaglandin, *Adv. Drug Deliv. Rev.*, 45 (1), pp. 65-75, 2000.

[109] R. A. Jain, The manufacturing techniques of various drug loaded biodegradable poly(lactide-*co*-glycolide) (PLGA) devices, *Biomaterials*, 21 (23), pp. 2475-2490, 2000.

[110] R. Arshady, Microsphres and Microcapsules: A Survey of Manufacturing Techniques. Part 1: Suspension Cross-Linking, *Polym. Eng. Sci.*, 29 (24), pp. 1746-1758, 1989.

[111] R. Arshady, Microsphres and Microcapsules: A Survey of Manufacturing Techniques. Part III: Solvent Evaporation, *Polym. Eng. Sci.*, 30 (15), pp. 915-924, 1990.

[112] G. Crotts, T. G. Park, Protein delivery from poly(lactic-co-glycolic acid) biodegradable microspheres: release kinetics and stability issues, *J. Microencapsul.*, 15 (6), pp. 699-713, 1998.

[113] J. J. Blaker, J. C. Knowles, R. M. Day, Novel fabrication techniques to produce microspheres by thermally induced phase separation for tissue engineering and drug delivery, *Acta Biomater.*, 4 (2), pp. 264-272, 2008.

[114] R. M. Day, J. J. Blaker, Microspheres, Patent No.: US 8,765,182 B2, 2008.

[115] H. Keshaw, N. Thapar, A. J. Burns, N. Mordan, J. C. Knowles, A. Forbes, R. M. Day, Microporous collagen spheres produced via thermally induced phase separation for tissue regeneration, *Acta Biomater.*, 6 (3), pp. 1158-1166, 2010.

[116] R. Ahmadi, N. Mordan, A. Forbes, R. M. Day, Enhanced attachment, growth and migration of smooth muscle cells on microcarriers produced using thermally induced phase separation, *Acta Biomater.*, 7 (4), pp. 1542-1549, 2011.

[117] H. Ghanbar, C. J. Luo, P. Bakhshi, R. M. Day, M. Edirisinghe, Preparation of porous microsphere-scaffolds by electrohydrodynamic forming and thermally induced phase separation, *Mater. Sci. Eng. C.*, 33, 2488-2498, 2013.

[118] D. P. Go, D. J. E. Harvie, N. Tirtaatmadja, S. L. Gras, A. J. O'Connor, A Simple, Scalable Process for the Production of Porous Polymer Microspheres by Ink-Jetting Combined with Thermally Induced Phase Separation, *Part. Part. Syst. Charact.*, 31 (6), pp. 685-698, 2014.

[119] P. A. Burke, L. A. Klumb, J. D. Herberger, X. C. Nguyen, R. A. Harrell, M. Zordich, Poly(lactide-co- glycolide) microsphere formulations of darbepoetin alfa: spray drying is an alternative to encapsulation by spray-freeze drying, *Pharm. Res.*, 21 (3), pp. 500-506, 2004.

[120] M. Murillo, C. Gamazo, M. M. Goni, J. M. Irache, M. J. Blanco-Prieto, Development of microparticles prepared by spray-drying as a vaccine delivery system against brucellosis, *Int. J. Pharm.*, 242 (1-2), pp. 341-344, 2002.

[121] P. He, S. S. Davis, L. Illum, Chitosan microspheres prepared by spray drying, *Int. J. Pharm.*, 187 (1), pp. 53-65, 1999.

[122] A. Sosnik, K. P. Seremeta, Advantages and challenges of the spray-drying technology for the production of pure drug particles and drug-loaded polymeric carriers, *Adv. Colloid Interface Sci.*, 223, pp. 40-54, 2015.

[123] J. Yao, L. K. Lim, J. Xie, J. Hua, C. Wang, Characterization of electrospraying process for polymeric particle fabrication, *J. Aerosol Sci.*, 39, pp. 987-1002, 2008.

[124] A. Jaworek, Micro- and nanoparticle production by electrospraying, *Powder Technol.*, 176, pp. 18-35, 2007.

[125] N. Bock, T. R. Dargaville, M. A. Woodruff, Electrospraying of polymers with therapeutic molecules: State of the art, *Prog. Polym. Sci.*, 37, pp. 1510-1551, 2012.

[126] Y.Wu, R. L. Clark, Controllable porous polymer particles generated by electrospraying, *J. Colloid Interface Sci.*, 310, pp. 529-535, 2007.

[127] S. Chakraborty, I. Liao, A. Adler, K. W. Leong, Electrohydrodynamics: A facile technique to fabricate drug delivery systems, *Adv. Drug Deliv. Rev.*, 61, pp. 1043-1054, 2009.

[128] J. Xie, J. Jiang, P. Davoodi, M. P. Srinivasan, C. Wang, Electrohydrodynamic atomization: A two-decade effort to produce and process micro-/nanoparticulate materials, *Chem. Eng. Sci.*, 125, pp. 32-57, 2015.

[129] A. Jaworek, A. T. Sobczyk, Electrospraying route to nanotechnology: An overview, *J. Electrostat.*, 66, pp. 197-219, 2008.

[130] M. Zamani, M. P. Prabhakaran, S. Ramakrishna, Advances in drug delivery via electrospun and electrosprayed nanomaterials, *Int. J. Nanomedicine*, 8, pp. 2997-3017, 2013.

[131] N. J. Felici, Recent Developments and Future Trends in Electrostatic Generation, *Direct Current*, 4 (7), pp. 3-12, 1959.

[132] A. G. Bailey, Electrostatic Spraying of Liquids, J. Wiley & Sons, NY, USA, 1988.

[133] L. Rayleigh FRS, On the equilibrium of liquid conducting masses charged with electricity, *Philos. Mag.*, 14 (87), pp. 184-186, 1882.

[134] O. V. Salata, Tools of Nanotechnology: Electrospray, *Curr. Nanosci.*, 1, pp. 25-33, 2005.

[135] G. Taylor FRS, Disintegration of Water Drops in an Electric Field, *Proc. R. Soc. London, Ser. A*, 280 (1382), pp. 383-397, 1964.

[136] M. Cloupeau, B. Prunet-Foch, Electrostatic spraying of liquids in cone-jet mode, *J. Electrost.*, 22, pp. 135-159, 1989.

[137] M. Cloupeau, B. Prunet-Foch, Electrostatic spraying of liquids: Main functioning modes. *J. Electrost.*, 25, pp. 165-184, 1990.

[138] A. Gomez, K. Tang, Charge and fission of droplets in electrostatic sprays, *Phys. Fluids*, 6, pp. 404-414, 1994.

[139] A. Jaworek, Electrospray Technology for Thin-Film Deposition, *Nova Science Publishers*, Inc., NY, USA, 2010.

[140] D. Chen, D. Y. H. Pui, S. L. Kaufmar, Electrospraying of conducting liquids for monodisperse aerosol generation in the 4 nm to 1.8 μm diameter range, *J. Aerosol Sci.*, 26 (6), pp. 963-977, 1995.

[141] J. F. de la Mora, I. G. Loscertales, The Current Emitted by Highly Conducting Taylor Cones, *J. Fluid Mech.*, 260, pp. 155-184, 1994.

[142] J. F. de la Mora, The Fluid Dynamics of Taylor Cones, *Annu. Rev. Fluid Mech.*, 39, pp. 217-243, 2007.

[143] K. Tang, A. Gomez, Monodisperse Electrosprays of Low Electric Conductivity Liquids in the Cone-Jet Mode, *J. Colloid Interface Sci.*, 184 (2), pp. 500-511, 1996.

[144] C. N. Ryan, K. L. Smith, J. P. W. Stark, The flow rate sensitivity to voltage across four electrospray modes, *Appl. Phys. Lett.*, 104, pp. 1-4, 2014.

[145] M. Cloupeau, B. Prunet-Foch, Electrohydrodynamic Spraying Functioning Modes: A Critical Review, *J. Aerosol Sci.*, 25 (6), pp. 1021-1036, 1994.

[146] F. Danhier, E. Ansorena, J. M. Silva, R. Coco, A. Le Breton, V. Préat, PLGA-based nanoparticles: An overview of biomedical applications, *J. Controlled Release*, 161 (2), pp. 505-522, 2012.

[147] B. Almería, W. Deng, T. M. Fahmy, A. Gomez, Controlling the morphology of electrospray-generated PLGA microparticles for drug delivery, *J. Colloid Interface Sci.*, 343 (1), pp. 125-133, 2010.

[148] A. Bohr, J. Kristensen, E. Stride, M. Dyas, M. Edirisinghe, Preparation of microspheres containing low solubility drug compound by electrohydrodynamic spraying, *Int. J. Pharm.*, 412 (1-2), pp. 59-67, 2011.

[149] A. Bohr, M. Yang, S. Baldursdóttir, J. Kristensen, M. Dyas, E. Stride, M. Edirisinghe, Particle formation and characteristics of Celecoxib-loaded poly(lactic-co-glycolic acid) microparticles prepared in different solvents using electrospraying, *Polymer*, 53 (15), pp. 3220-3229, 2012.

[150] S. D. Nath, S. Son, A. Sadiasa, Y. K. Min, B. T. Lee, Preparation and characterization of PLGA microspheres by the electrospraying method for delivering simvastatin for bone regeneration, *Int. J. Pharm.*, 443 (1-2), pp. 87-94, 2013.

[151] G. Zhang, R. Hou, D. Zhan, Y. Cong, Y. Cheng, J. Fu, Fabrication of hollow porous PLGA microspheres for controlled protein release and promotion of cell compatibility, *Chin. Chem. Lett.*, 24 (8), pp. 710-714, 2013.

[152] L. Nie, G. Zhang, R. Hou, H. Xu, Y. Li, J. Fu, Controllable promotion of chondrocyte adhesion and growth on PVA hydrogels by controlled release of TGF-β1 from porous PLGA microspheres, *Colloids Surf., B*, 125 (1), pp. 51-57, 2015.

[153] D. L. Wise, Handbook of pharmaceutical controlled release technology, *Marcel Dekker Inc.*, New York, 2002.

[154] M. Vert, J. Feijen, A. Albertsson, G. Scott, E. Chiellini, Biodegradable Polymers and Plastics, *Royal Society of Chemistry*; First Edition, 1992.

[155] J. A. Tamada, R. Langer, Erosion kinetics of hydrolytically degradable polymers, *Proceedings of the National Academy of Sciences of the United States of America*, 90 (2), pp. 552-556, 1993.

[156] J.S. Lee, G. S. Chae, M. S. Kim, S. H. Cho, H. B. Lee, G. Khang, Degradation behaviour in vitro for poly(D,L-lactide-co-glycolide) as drug carrier, *Biomed. Mater. Eng.*, 14 (2), pp. 185-192, 2004.

[157] R. Arshady, Preparation of biodegradable microspheres and microcapsules: 2. Polyactides and related polyesters, *J. Control. Release*, 17, pp. 1-22, 1991

[158] A. Rohiman, I. Anshori, A. Surawijaya, I. Idris, Study of Colloidal Gold Synthesis Using Turkevich Method, *American Institute of Physics*, 1415 (39), pp. 39-42, 2011.

[159] S.K. Ghosh, S. Nath, S. Kundu, K. Esumi, T. Pal, Solvent and Ligand Effects on the Localized Surface Plasmon Resonance (LSPR) of Gold Colloids, *Journal of Physical Chemistry B,* 108 (37), pp. 13963-13971, 2004.

[160] E.W. Washburn, Note on a Method of Determining the Distribution of Pore Sizes in a Porous Material, *Proceedings of the National Academy of Sciences of the United States of America*, 7 (4), pp. 115-116, 1921.

[161] S. Gangwal, O. J. Cayre, M. Z. Bazant, O. D. Velev, Induced-charge electrophoresis of metallo-dielectric particles, *Phys. Rev. Lett.*, 100 (5), 058302, 2008.

[162] S. Gupta, R. G. Alargova, P. K. Kilpatrick, O. D. Velev, On-chip electric field driven assembly of biocomposites from live cells and functionalized particles, *Soft Matter*, 4 (4), pp. 726-730, 2008.

[163] T. Sakai, P. Alexandridis, Mechanism of Gold Metal Ion Reduction, Nanoparticle Growth and Size Control in Aqueous Amphiphilic Block Copolymer Solutions at Ambient Conditions, *J. Phys. Chem. B*, 109 (16), pp. 7766-7777, 2005.

[164] B. L. V. Prasad, S. I. Stoeva, C. M. Sorensen, K. J. Klabunde, Digestive Ripening of Thiolated Gold Nanoparticles: The Effect of Alkyl Chain Length, *Langmuir*, 18, pp. 7515-7520, 2002.

[165] P. Sahu, B.L.V. Prasad, Effect of digestive ripening agent on nanoparticle size in the digestive ripening process, *Chem. Phys. Lett.*, 525-526, pp. 101-104, 2012.

[166] Y. Yang, P. Gao, S. Gaba, T. Chang, X. Pan, W. Lu, Observation of conducting filament growth in nanoscale resistive memories, *Nat. Commun.*, 3 (732), pp. 1-8, 2012.

[167] D. Kwon, K. M. Kim, J. H. Jang, J. M. Jeon, M. H. Lee, G. H. Kim, X. Li, G. Park, B. Lee, S. Han, M. Kim, C. S. Hwang, Atomic structure of conducting nanofilaments in TiO_2 resistive switching memory, *Nat. Nanotechnol.*, 5, pp. 148-153, 2010.

[168] J. Lee, Progress in non-volatile memory devices based on nanostructured materials and nanofabrication, *J. Mater. Chem.*, 21, pp. 14097-14112, 2011.

[169] Y. Yang, W. Lu, Nanoscale resistive switching devices: mechanisms and modeling, *Nanoscale*, 5, pp. 10076-10092, 2013.

[170] F. Chiu, A Review on Conduction Mechanisms in Dielectric Films, *Advances in Materials Science and Engineering*, pp. 1-18, 2014.

[171] H. Da, W. Jie, T. Hua, Analysis and modeling of resistive switching mechanisms oriented to resistive random-access memory, *Chin. Phys. B*, 22 (3), pp. 1-6, 2013.

[172] L. Ma, S. Pyo, J. Ouyang, Q. Xu, Y. Yang, Nonvolatile electrical bistability of organic/metal nanocluster/organic system, *Appl. Phys. Lett.*, 82 (9), pp. 1419-1421, 2003.

[173] J. He, L. Ma, J. Wu, Y. Yang, Three-terminal organic memory devices, *J. Appl. Phys.*, 97, pp. 1-6, 2005.

[174] A. Zabet-Khosousi, A. Dhirani, Charge Transport in Nanoparticle Assemblies, *Chem. Rev.*, 108 (10), pp. 4072-4124, 2008.

[175] T. Ludtke, P. Mirovsky, R. Huther, L. Govor, G. H. Bauer, J. Parisi, R. J. Haug, Charge transport through chains of nanoparticles, *Physica E*, 42, pp. 2830-2833, 2010.

[176] R. J. Tseng, C. O. Baker, B. Shedd, J. Huang, R. B. Kaner, J. Ouyang, Y. Yang, Charge transfer effect in the polyaniline-gold nanoparticle memory system, *Appl. Phys. Lett.*, 90, pp. 1-3, 2007.

[177] T. Ludtke, P. Mirovsky, R. Huther, L. Govor, G. H. Bauer, J. Parisi, R. J. Haug, Transport in nanoparticle chains influenced by reordering, *Physical Letters A*, 375, pp. 2079-2081, 2011.

[178] T. Mikolajick, M. Salinga, M. Kund, T. Kever, Nonvolatile Memory Concepts Based on Resistive Switching in Inorganic Materials, *Adv. Eng. Mater.*, 11 (4), pp. 235-240, 2009.

[179] J. Ouyang, Materials effects on the electrode-sensitive bipolar resistive switches of polymer:gold nanoparticle memory devices, *Organic Electronics*, 14, pp. 1458-1466, 2013.

[180] W. L. Kwan, B. Lei, Y. Shao, Y. Yang, Understanding the switching mechanism of polymer memory, *Current Applied Physics*, 10, pp. 50-53, 2010.

[181] J.A. Champion, S. Mitragotri, Role of target geometry in phagocytosis, *Proc. Natl. Acad. Sci. U. S. A.*, 103 (13), pp. 4930-4934, 2006.

[182] K. S. Soppimath, T.M. Aminabhavi, A.R. Kulkarni, W.E. Rudzinski, Biodegradable polymeric nanoparticles as drug delivery devices, *J. Controlled Release*, 70 (1-2), pp. 1-20, 2001.

[183] G. Schliecker, C. Schmidt, S. Fuchs, R. Wombacher, T.Kissel, Hydrolytic degradation of poly(lactide-co- glycolide) films: effect of oligomers on degradation rate and crystallinity, *Int. J. Pharm.*, 266 (1-2), pp. 39-49, 2003.